

Endurance Test Strategies for Pitch Bearings of Wind Turbines

Von der Fakultät für Bauingenieurwesen und Geodäsie
der Gottfried Wilhelm Leibniz Universität Hannover
zur Erlangung des Grades

Doktor der Ingenieurwissenschaften
– Dr.-Ing. –

genehmigte Dissertation von

Matthias Stammler

geboren am 22.10.1982 in Henstedt-Ulzburg

2020

Referent: **Prof. Dr.-Ing. Andreas Reuter**
Gottfried Wilhelm Leibniz Universität Hannover,
Institut für Windenergiesysteme

Korreferent: **Prof. Dr.-Ing. Gerhard Poll**
Gottfried Wilhelm Leibniz Universität Hannover,
Institut für Maschinenkonstruktion und Tribologie

Kommissionsmitglied: **Prof. Dr.-Ing. Michael Beer**
Gottfried Wilhelm Leibniz Universität Hannover,
Institut für Risiko und Zuverlässigkeit

Vorsitz: **Prof. Dr.-Ing. Ludger Lohaus**
Gottfried Wilhelm Leibniz Universität Hannover,
Institut für Baustoffe

Tag der Promotion: 3. Juni 2020

Abstract

Modern wind turbines turn their blades along their primary axis to control the conversion of aerodynamic power. The pitch bearings connect the rotor hub of the turbine with the blades and allow this rotation. They are large slewing bearings with diameters in the range of 2 - 7 m. In comparison to bearings in other applications, pitch bearings suffer from three particularities: Oscillating movements instead of full rotations, dynamic and stochastic loads in five degrees of freedom instead of controlled loads, and interface parts with low and complex stiffness along the circumference instead of almost stiff connections.

The capital costs of the bearings and even more the costs connected to failures make it paramount to mitigate operational risks of new designs. As there are no established calculation methods for the most dominant damage modes of pitch bearings, bearing tests are of critical value to this risk mitigation.

This work covers the design of endurance test runs for pitch bearings. A true endurance test run of pitch bearings should result in a profound evaluation of the risk of failure during the lifetime of the wind turbine. This goal makes the design of an endurance run a substantial task. It gets even more challenging when such a test run needs to fit into the overall turbine design process, both in matters of timing and finance.

This work results in a test run profile that covers wear and fatigue damage modes of the bearing rollers and raceways, among others. It also covers the development and commissioning of the test environment for different bearing sizes. The IWT7.5-164 reference turbine serves as example for the design of the test environment and the test run.

Zusammenfassung

Moderne Windenergieanlagen drehen die Rotorblätter um die Längsachse und kontrollieren so die Umwandlung der im Wind enthaltenen Energie. Blattlager verbinden die Rotornabe mit den Rotorblättern und ermöglichen diese Drehung. Blattlager sind Großwälzlager mit einem Durchmesser von 2 bis 7 m. Im Vergleich zu Wälzlagern in anderen Anwendungen weisen sie folgende Besonderheiten auf: Die Drehungen erfolgen oszillierend und nicht dauerhaft rotierend. Die äußeren Belastungen sind dynamisch und stochastisch und nur teilweise kontrollierbar. Die Schnittstellenbauteile haben eine geringe und über dem Umfang variierende Steifigkeit.

Der Anschaffungspreis von Blattlagern und insbesondere die mit Ausfällen verbundenen Kosten erfordern eine Bewertung von Ausfallrisiken bei neuen Auslegungen. Da es keine hinreichenden Berechnungsmethoden für die dominanten Schadensmechanismen gibt, sind Blattlagertests von entscheidender Bedeutung im Auslegungsprozess.

Diese Arbeit leistet einen Beitrag zur Entwicklung von Dauertestprogrammen für Blattlager. Ein echter Dauertest resultiert in einer fundierten Bewertung des Ausfallrisikos für die Lebensdauer der Windenergieanlage. Dieses Ziel macht die Entwicklung eines Dauerlaufs zu einer Herausforderung, insbesondere, wenn Zeit- und Kostenrahmen von üblichen Entwicklungsprozessen berücksichtigt werden müssen.

Das Ergebnis dieser Arbeit ist ein Testprogramm, das Ermüdung und Verschleiß der Lagerlaufbahnen und Wälzkörper sowie weitere Schadensmechanismen abdeckt. Hierfür wurde eine Prüfumgebung konzipiert und in Betrieb genommen. Die IWT7.5-164 Referenzwindenergieanlage dient als Beispiel für die Auslegung der Prüfumgebung und des Prüflaufs.

Acknowledgments

One of my (daughter's) favorite books is *The Snail and the Whale* by Donaldson and Scheffler. It is about a little sea snail that befriends a humpback whale and travels the entire world on his tail. After seeing the Antarctica, Caribbean Islands, and many other wonders this planet has to offer, one page reads as follows:

'And she gazed at the sea, the sky, the stars
she gazed and gazed, amazed by it all
and said to the whale " I feel so small."

One of the greatest privileges an adult can have is to gaze – and, well, to feel small sometimes doesn't hurt either. I have worked in various fields of engineering, but never had so many opportunities to gaze at the shier dimensions, the elegance of the white steel and FRP, and the wonderful engineering than I have in the wind energy in general and with the Fraunhofer IWES in particular.

Acknowledgments of phd theses sometimes mention the hardships that came along with the project. I did not suffer hardships, so I gladly skip this part. However, the lack of hardships is thanks to the contributions of other persons, and I will try to give a shout out to each and every one of them.

To Andreas, for taking decisions swiftly and the help at a point I was severely stuck. To Professor Poll, who is a walking encyclopedia of tribology and the people connected to it. To Katharina, for being the person to find the very small and the very big errors in ideas and texts, and in particular for having hundreds helpful comments on an earlier version of this one. To Christian, my open-minded manager at the institute. To Arne, who was the first student working with me at the IWES and became a remarkable engineer. Fabian, designer of the hub, and the driving force between many a publication. Felix, one of the best designers and astoundingly positive persons I know. Gregor, who spent so many hours with me at the first test rig in Bremerhaven. Lale, my sister, and Thomas, for some rounds of proof reading. The Hamburg team of Karsten, Oliver, Florian, Matthis, Nils, and Filip - it is a pleasure to work with you. The relentless people of IDOM who spent considerable time of their lives in Hamburg for assembling and commissioning the test rig. A bunch of people from the Bremerhaven administration and IT, in particular Antje, for supporting fast and well. Sven, for pushing his former company into blade bearing tests and making my first large rig possible. Eike, who took over his role later and has a refreshingly critical mind. The students who spent their internships and theses stays with me, and in particular Christian, Sebastian, Khaldoun, and Bahram.

Acknowledgments

It feels somewhat odd not to mention my family and friends - the persons who did not directly help with this endeavor, but whom I love to bits for so many reasons. I salute you with a smile and good memories to the Chefschaumschnippler, 'Lachs,wer?' and Gerd das Pferd. Last I would like to mention, or rather dedicate this work, to the one person that was a role model in so many ways before I even understood what that was. Mehmet Atif Özren was an engineer who graduated from the same engineering school I did and was like a father to me. Thank you, wherever you are.

Contents

Abstract	iii
Zusammenfassung	v
Acknowledgments	vii
1 Introduction	1
2 State of the Art	3
2.1 Wind Turbines	3
2.1.1 Principles and History	3
2.1.2 Load Simulation and Post-Processing	6
2.1.3 Pitch Control	10
2.1.4 IWT7.5 Reference Wind Turbine	12
2.2 Rolling Bearings	14
2.2.1 Principles and History	14
2.2.2 Hertzian Calculation of Contact Parameters	15
2.2.3 Kinematics and Slip	19
2.2.4 Grease Lubrication	21
2.3 Pitch Bearings	22
2.3.1 Bearing Types	22
2.3.2 Operating Conditions	24
2.3.3 Interfaces	29
2.3.4 The IWT7.5 Pitch Bearing and its Interfaces	31
2.4 Damage Modes of Pitch Bearings	37
2.4.1 Overview	37
2.4.2 Fatigue of Rolling Contacts	38
2.4.3 Wear of Raceways, Rollers and Gears	40
2.4.4 Static Overload and Edge Wear	42
2.4.5 Other Damage Modes	43
2.5 Design of Pitch Bearings	44
2.5.1 FE Simulation of Pitch Bearings	44
2.5.2 Prevention of Damage Modes	50
2.6 Test Rigs for Pitch Bearings	51
2.7 Chapter Summary	53

3	Data Analysis	55
3.1	Range-pair Counting and Bin Counting	55
3.2	Movement Sequence Recognition	58
4	Scaled Sequence Tests	61
4.1	Reasons for Scaled Sequence Tests	61
4.2	Scaling Criteria and Bearing Choice	62
4.3	BEAT0.1 Test Rig and Test Program	66
4.4	Results of Scaled Sequence Tests and Reference Tests	72
5	Creation of the Test Environment	79
5.1	Test Rig Purpose	79
5.2	Design Requirements	81
5.3	BEAT6.1 Rig	84
5.4	Emulation Parts	85
5.4.1	Requirements	85
5.4.2	Hub Adapter	86
5.4.3	Force Transition Element	89
6	Endurance Run Program	93
6.1	Wear Profile Input	93
6.2	Wear Profile Composition	98
6.3	Rolling Contact Fatigue Profile	105
7	Conclusions and Outlook	109
	References	111
	Annex	121

Chapter 1

Introduction

This work investigates test programs for pitch bearings of wind turbines. Pitch bearings (also called blade bearings) are rotary joints and connect the rotor blades of a wind turbine with the rotor hub. They allow the turbine controller to rotate the rotor blades along their primary axis, which in turn controls the aerodynamic forces of the blade. This rotation is commonly called pitching. [1–3] To the knowledge of the author, all existing pitch bearings are rolling bearings, and the dominant type are four-point contact ball bearings. Three-row bearings with rollers or balls are alternative concepts. The root diameter of the rotor blades determines the pitch bearing diameter, which is in the range of 2-7 m for currently available commercial turbines with rated powers in a range of 2 to 12 MW.

Pitch bearings suffer from different challenges than bearings in most other industrial applications. In particular, they execute oscillating movements instead of full rotations [2], they experience stochastic loads in five degrees of freedom instead of controlled loads [4], and they connect with interface parts that have a relatively low and varying stiffness along their circumference [5,6]. Last, practical research for bearings of comparable sizes is sparse, mostly due to the involved costs.

Pitch bearings have various possible damage modes of which not all are completely understood at the current stage of science. Especially wear of the raceways and rolling bodies cannot be predicted with respect to its occurrence and progression [7,8]. Commercial design of these bearings rests upon experience with previous applications and static calculations. While rolling contact fatigue calculations are available [9–11], to the knowledge of the author rolling contact fatigue plays a minor role in real-world failures of pitch bearings. With growing turbine sizes and a fierce competition between manufacturers [12], requirements for pitch bearings get more challenging. Two major trends drive this change: Firstly, the approach to use lightweight turbine components for the sake of reduction of capital costs and weight-related loads on main structures like the tower, and secondly load mitigation controllers which reduce loads on most structures resulting in an unprecedented set of movements of pitch bearings [13], The consequences of these movements are unknown.

At this point, it is necessary to mention that the exchange of a pitch bearing of large offshore wind turbines comes at costs far above one million euro. A design flaw within the pitch system of a fleet of offshore wind turbines would be a serious financial threat even to the largest companies.

All the aforementioned summarizes to a combined risk of uncertainty in the design, major changes in the operation conditions and substantial financial consequences of pitch bearings failures. Endurance tests of pitch bearings that represent their operational life can minimize this risk. Given the uncertainty about damage modes, the complex interfaces and the dynamic loads, the question how to carry out such endurance runs is not trivial and has not been answered satisfyingly yet. Approaches for pitch and other wind turbine bearings limit to accelerated runs with a focus on rolling contact fatigue and robustness tests, which combine fatigue runs with a collection of time series [14, 15]. The increased oscillatory activity of pitch bearings with novel controllers [13] and the current state of research with small bearings [7] indicate that wear is a more important damage mode than rolling contact fatigue. This thesis follows a novel approach with focus on wear damage modes.

The present thesis is structured in the following way: Chapter 2 presents the state of the art in all fields related to this thesis. These are the wind turbines themselves (Section 2.1), rolling bearings in general (Section 2.2) and pitch bearings in particular (Section 2.3). Further sections dedicate to the damage modes of pitch bearings (Section 2.4), their design process (Section 2.5) and existing test rigs for pitch bearings and similar bearings (Section 2.6).

Chapter 3 covers the matter of data analysis. In the context of this work, data analysis refers to the transfer of time series (like the output of a wind turbine load simulation) into a set of data that lays the foundation for the later endurance run program. Range-pair and bin counting (Section 3.1) provide the amplitudes and frequencies of all oscillatory movements as well as the absolute values of any signal, sorted into bins. Later sequence recognition (Section 3.2) gives insight into the clusters of similar oscillations. The author applies all these methods to the time series of the IWT7.5-164 reference turbine.

Over the course of this work, the need for scaled functional tests became more and more evident. Chapter 4 sheds light onto the reasons for this need (Section 4.1) and describes criteria for scaled tests (Section 4.2). The author used the BEAT0.1 test rig (Section 4.3) to run the tests the results of which are part of Section 4.4.

Chapter 5 contains a description on the test environment the author uses for the endurance runs. The name of this environment is BEAT6.1 (Bearing Endurance and Acceptance Test rig for 6 meter bearings, the first of its kind). As an introduction to the design path of this test rig, Section 5.1 describes possible purposes of test rigs. Section 5.2 on page covers the design requirements, and Section 5.3 presents the test rig. The parts that emulate the interfaces, rotor blade and rotor hub, conclude this chapter (Section 5.4).

Chapter 6 presents the methods to create endurance run programs and the endurance run program for the pitch bearings of the IWT7.5-164 reference turbine. It splits into sections on the input for wear profiles (Section 6.1), the later output (Section 6.2), and one section on fatigue profiles (Section 6.3, containing both input and output).

The final Chapter 7 of this thesis provides the key conclusions of this work as well as an outlook.

Chapter 2

State of the Art

2.1 Wind Turbines

2.1.1 Principles and History

Humankind has changed ecosystems on regional scale for thousands of years. Since the beginning of the industrialization, this influence is on a global scale. [16] The use of the planet's resources exceeds its ability to regrow them by far. In 2019, all resources earth provides within a year were consumed by July 29th [17]. The consequences of this become more and more evident with every new heat record and an increasing number of natural disasters [18].

With almost certainty, humankind will not undertake all necessary efforts to limit the global warming it caused by burning fossile fuels. Decades of ignorance, convenience, and avoidance minimized realistic possiblities to keep the temperature level at 1.5 degrees over pre-industrialization averages. [19]

The Intergovernmental Panel on Climate Change (IPCC) estimates severe mid-term effects, of which the most challenging for all societies is the migration of hundreds of millions of persons from then uninhabitable areas of the planet. [16] As even the migration of some hundred thousands of refugees during the wars in Syria intensified the rise of right-wing populist parties all over Europe [20], the author thinks it is only fair to assume that democratic structures will suffer with larger-scale migration movements – not because of the migration, but because of humans' inability to handle such situations.

This short and drab excursion leads us to one of the more successful attempts to reduce man-made pollutions. The actions needed to keep climate change within boundaries might be too enormous to realize, yet it is our responsibility to our children to give it a solid try. One means to this end is wind energy. Mankind has harvested power from wind since 1750 BC [21]. Until the late 19th century, the main purpose was of mechanical nature: Grind crops and pump water [22]. Cheap and continuously available energy from coal made this application obsolete by the end of the 19th century. Converting wind energy into electrical energy was always a possibility, yet could it not

compete with cheap fossil fuels. Only in niche applications, like remote farms in Denmark, wind turbines provided electrical power [22].

The key trigger for the development of modern wind turbines were the same fossil fuels that superseded it earlier: The oil crisis in the 1970s demonstrated the dependence of all western societies on cheap Arabic oil. Wind energy promised independence, and many western countries started to investigate it. [1, 22] From the very beginning, this approach was undermined by parties and companies who made good money with fossil fuel trade - one prominent example being the German research turbine Growian. The electrical power company RWE participated in the design and erection of this turbine - not to make it a success, but to prove the invalidity of the overall concept. [21] As the Growian, most large, multi-megawatt research turbines of the late 70s and early 80s had severe design flaws and ran only for a few hundred hours [1]. It became evident that wind turbines did not provide an immediate solution to the voracious demand for electrical power. But, in a remarkable twist, some of the research results helped to develop small scale turbines in the countries of Denmark, Germany and the USA. Former agricultural engineering companies started with 25 kW (which could supply a single farm with electricity when running at rated power) sizes and used the knowledge and routine gained with each new turbine to grow them steadily. This development was further supported by the Chernobyl disaster in 1986, which impressively demonstrated the catastrophic consequences of failures in nuclear power plants. At the beginning of the new millennium, commercial wind turbines reached the size of former research monsters - but with more reliable operation and at a fraction of the costs. Wind turbines became utility scale, went offshore and got more and more reliable and cost-efficient. In 2019, wind energy production is one of the cheapest sources of electrical energy [23, 24] and offshore parks are to be built without any subsidies on power prices [25]. In 2016, wind energy contributed 13 percent to Germany's primary energy production [26]. After over 30 years of commercial development, there is no technical obstacle to prevent it from providing much larger shares, and the commercial competitiveness is given, in particular in the light of subsidies for fossil energy production [27]. If and when the full potential of wind energy is unleashed is merely yet dodgily a political question.

The dominant shape of wind turbines is the upwind, three-bladed, horizontal-axis type, see Figure 2.1 for a visualization. In contrast to very early windmills, the blades of this concept rely on aerodynamic lift. Almost all commercially available, multi-megawatt turbines follow this concept. The reasons for the dominance are twofold (as in most technical applications): First and simple, there is a lot of experience with it that allows to understand its commercial and technical characteristics, and second, there are some technical reasons for particular sub-solutions. An upwind turbine has the simple benefit of the wind acting on the blades before it reaches the tower. A yaw mechanism turns the entire tower head, including the rotor, into the incoming wind. The tower slows down the wind speed more drastically behind than in front of itself, and a downwind rotor consequently suffers from higher load fluctuations than an upwind one. Three blades are the lowest number of blades that give a reasonably harmonic load introduction to the drivetrain and structure. Single-bladed turbines always need a counterweight, whose size and cost are unreasonable for above-megawatt capacities. Even-numbered rotors suffer from higher load fluctuations: at the time one blade points downward and is in front of the tower, another blade points straight upward and has the highest aerodynamic load. Five or more blades would have

heavier rotors, which increases costs. Vertical axis turbines have never reached the efficiency of horizontal-axis turbines in real-life applications. [28]

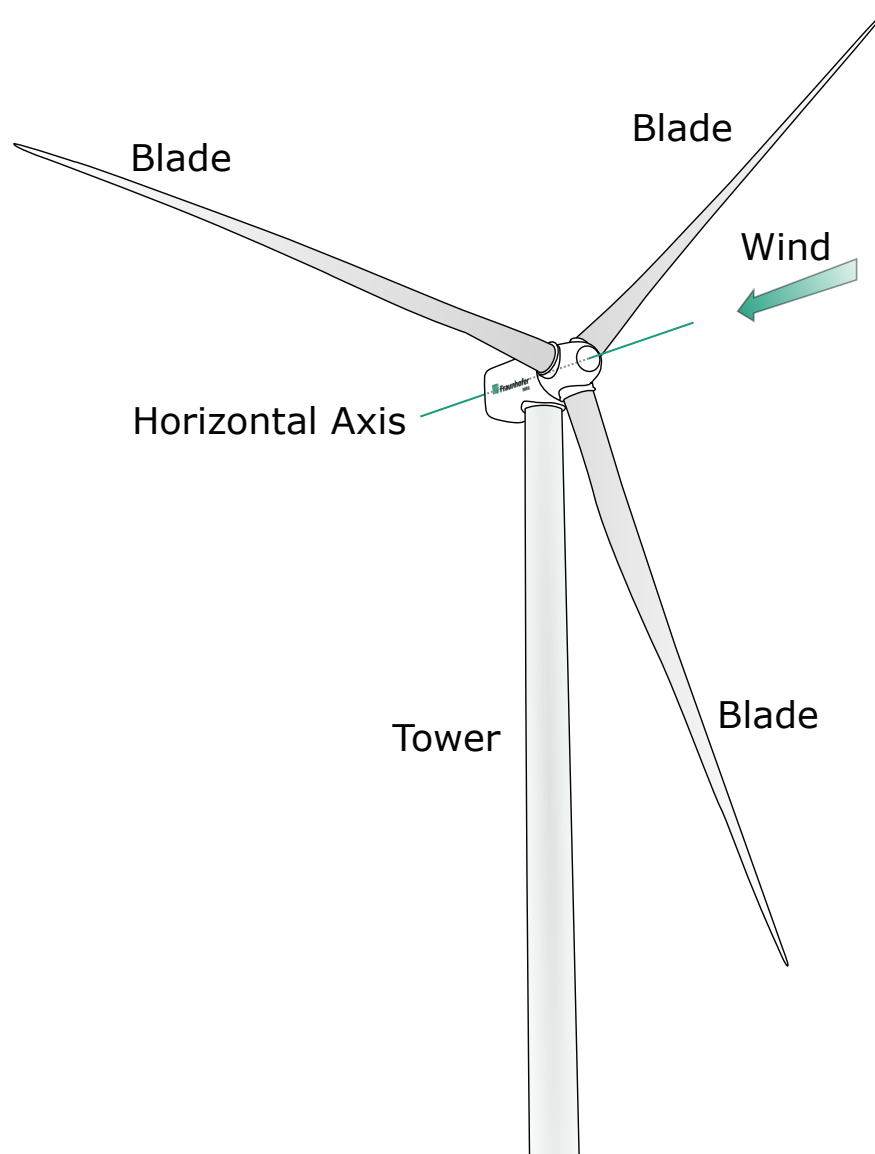


Figure 2.1: Dominant concept of a wind turbine with an upwind rotor, three blades and a horizontal axis.

Wind turbines have grown in size over the last decades and seem to continue this growth [29]. In 2019, the world's largest turbine is the GE Haliade X 12 MW offshore turbine. The rotor blades of this turbine have a length of 107 m [30]. While past and current growth leads to reduction in energy production costs, at a certain point further growth should increase them again: Practical experience has shown that the blade mass increases with the power of approximately 2.9 to the blade length, while theoretically one would expect the power of 3. The difference accounts to technical improvements [31]. Similar relationships can be found for any structural element of the

turbine, while the power output only increases with the power of 2 to the blade length. Mass is money, and this argues the case for a natural limit in turbine sizes. On the other hand, foundation and maintenance costs – particularly in offshore conditions – call for a reduced number of turbines with higher capacity.

Technical improvements can reduce the mass growth caused by larger rotors. One key technology to reduce masses are load reduction techniques. One of these is the individual control of pitch angles of rotor blades (Individual Pitch Control, IPC). This technique is the major driver behind this work and will be introduced in a later section.

2.1.2 Load Simulation and Post-Processing

The loads of wind turbines vary because the wind itself varies in speed, direction and turbulence. To the dismay of many wedding planners, weather itself is only predictable on very short terms, and such predictions always come with uncertainties. Any design for a wind turbine that has a lifespan of 20 years or longer comes with the same uncertainties. As it is impossible to know every wind condition for the entire lifetime, wind turbine designers work with security margins and reasonable assumptions of probabilities. Based on known wind speed and turbulence distributions, a probable wind speed and turbulence distribution is derived. This is further split into probable operation modes and results in a list of Design Load Cases (DLC). With these DLC, the loads for the turbine are calculated, and the results are multiplied with security factors to account for uncertainty. An example DLC is the power production without any fault (calculated for different wind vectors). [2, 32]

With the early research turbines like the Growian, designers did not take account of turbulences. The results were unrealistically low fatigue loads, which were used to design a welded steel hub. It resisted the real fatigue loads for a few hundred hours, but was thought to last several years. [1] This disappointing result was a very valuable lesson, as only a few years later wind turbulence was an established part of the load calculations. [33].

Wind causes the loads that act upon the structures of the turbine, but getting from an assumed wind speed distribution to the loads of individual components takes some work. The blades convert the wind into lift and drag. But these are not the only loads the blades transfer to the blade roots: Blades have a substantial weight and produce gravitational as well as centrifugal forces. All of these result in a combination of bending moments and forces at the blade root. The loads of the three blades add up to a combined load in the hub and the subsequent structures like the drivetrain and the tower. Unfortunately, none of the components are infinitely stiff. In fact most wind turbine design are as flexible as possible (to save money on material). As the structures deform under load, the blades also change their aerodynamic properties. Consequently, load calculation of the entire turbine has to be an iterative process. As it covers both aerodynamic and elastic behavior of the turbine, it is known as aero-elastic simulation.

For every instant of the lifetime of the wind turbine, the behavior of the entire turbine has to be calculated. This behavior is not only determined by the conditions at this instance, it is also

influenced by the time instants before which determine the initial deformation and position of the turbine. The level of detail of such a calculation is a question of available computational power and time. A simulation of the surrounding wind and the entire turbine on molecular level is not possible with the computational resources available on this planet, so any model needs to be a simplification. Due to the high number of time instances that need calculation, both the wind-blade interaction and the flexibility of the turbine are simplified. [1]

Figure 2.2 visualizes the blade sections and tower sections of an aero-elastic model. The two dots represent the hub and the drivetrain, both of which have only one rotational degree of freedom. The use of a discrete number of sections is a common simplification in these simulations.

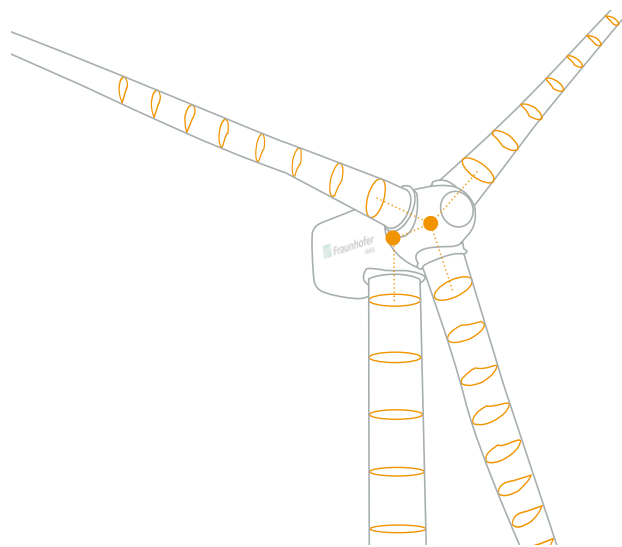


Figure 2.2: Sections of blades and tower for aero-elastic simulations

The common simplification for wind-blade-interaction goes by the name blade-element-momentum (BEM) method. A discrete number of sections with aerodynamic properties represents the blade. Empirical models cover more complicated aerodynamic effects like tip losses and wake effects. The flexibility is simplified in a similar way: For a limited number of blade sections, the mechanical properties are calculated. Hub, main frame and drive train are assumed as stiff, with the rotation of the drive train being the only degree of freedom. The tower, like the blades, consists of a discrete number of sections with different mechanical properties.

Even with these simplifications, a calculation of 20 or more years would use too many resources for a turbine design process. Thus, the average wind speeds are stacked into bins, simulated for ten minutes, and the resulting time series are repeated according to their wind speed to fill the turbine lifetime. Uncertainty is covered by different start conditions for each bin (called seed). Figure 2.3 shows an example of time series. This figure contains three signals: M_{yB} and M_{xB} are bending moments at a blade root, and the pitch angle is the angle the blade turns about its primary axis. A load simulation according to IEC [32] contains more than hundred of such time series outputs, each of which contains some hundred signals.

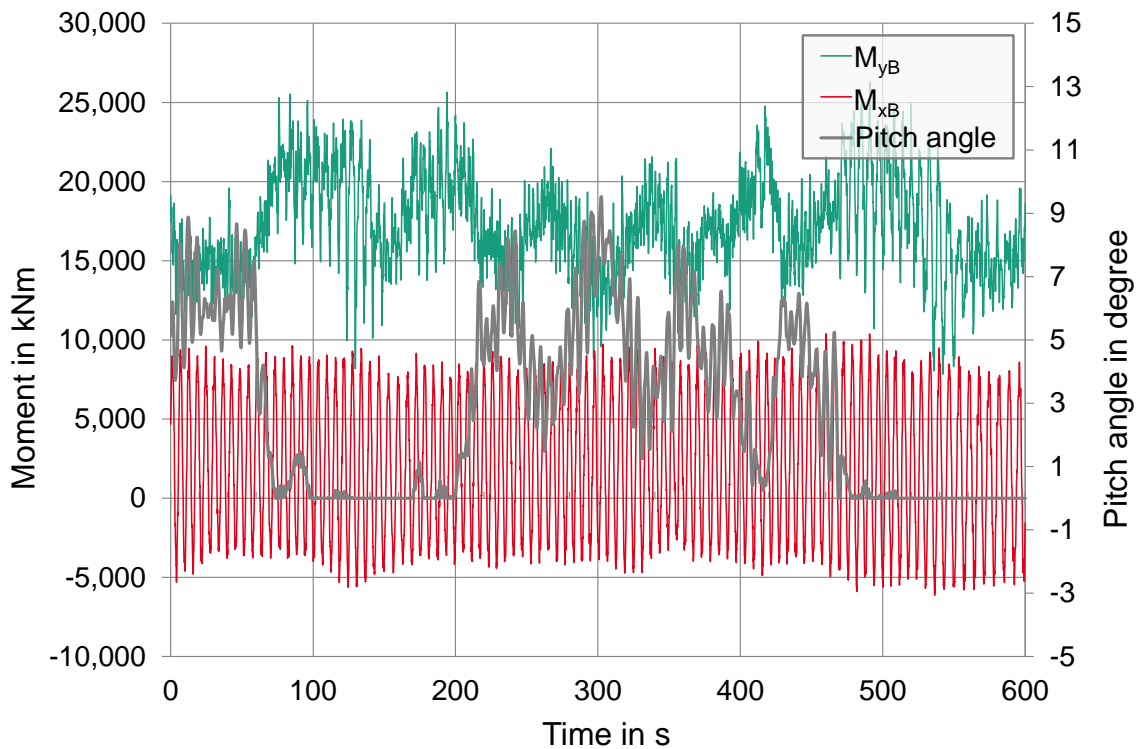


Figure 2.3: Example time series with blade root bending moments and pitch angle

The extreme values of the time series (with safety factors) are the input for ultimate strength calculations. For the fatigue calculations, the time series are post-processed. The author summarized typical post-processing techniques in [4], the following explanations stem from this reference. Common post-processing of time series includes rainflow counting [34], bin counting of signals and damage equivalent load (DEL) calculation [35].

Rainflow counting is widely used to create data input for fatigue calculations (see Figure 2.4). The algorithm treats the distance between the minimum and the maximum value as a single flank or half cycle (see number 1 in Figure 2.4). The name rainflow count is derived from this characteristic, as the gray path behaves like a water drop flowing down a roof if the figure is turned by 90° . To avoid double counting of value changes, other flanks that would interfere with the way of the gray path are intersected by it. This thus creates cycles 2/3, 4/5 and 6/7. Half cycle 1 is not a continuous movement, yet it is counted as one cycle, as the overall movement from the lowest to the highest load level is a relevant input for fatigue calculations. While rainflow counting simplifies the time series into something that can be handled in fatigue calculations, it comes with a drawback: If loads in several degrees of freedom act upon a component (like the hub of a wind turbine), the phase information about the individual loads is lost in the process.

Figure 2.5 shows the process of DEL creation. The results of the rainflow counting are a number of combinations of amplitudes and cycles (indicated as 1,2,3 in the figure). Given a certain relation

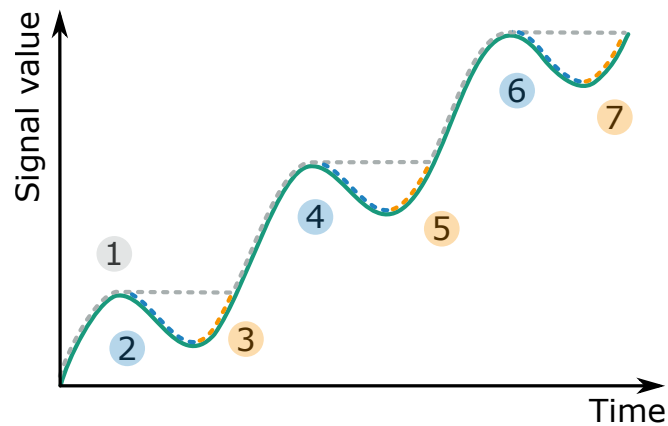


Figure 2.4: Visualization of rainflow counting

between stress cycles and cycles-to-failure (S-N slope), these values are transferred to an arbitrarily chosen amplitude level that is the same for all values (dotted arrows in Figure 2.5). The cycle values can then be summed (Σ -symbol in Figure 2.5). The S-N slope is again used to transfer this summed value to a chosen number of cycles and the corresponding amplitude level. None of these operations changes the summed fatigue damage to the part. DEL allow a simple fatigue calculation of structural parts.

Aero-elastic load simulations calculate the loads of turbine components with reasonable simplifications. Loads have the format of time series which then are post-processed to use them for ultimate and fatigue load calculations.

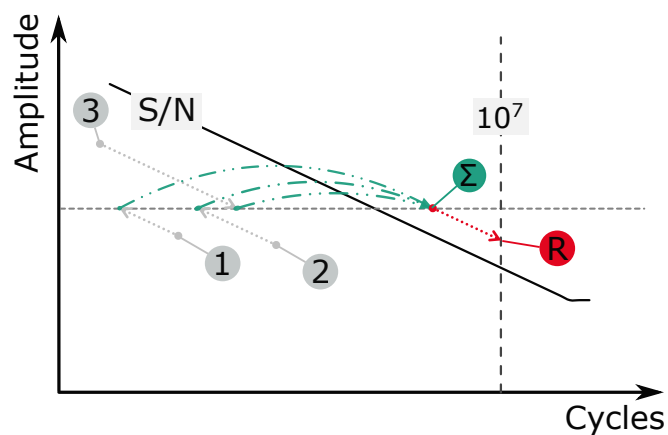


Figure 2.5: Visualization of DEL calculation

2.1.3 Pitch Control

If wind turbines could choose wind conditions, they preferred a steady wind inflow without turbulences, at rated speed, and with the uniform direction in the whole rotor area. Sadly, wind does not care about wind turbine preferences and changes frequently, in speed, direction, and turbulence. Modern wind turbines (in contrast to the wind mills of past millenia) have rotor blades that convert the inflowing wind into lift and an unavoidable fraction of drag. Depending on the wind speed and inflow angle, the lift and drag at each section of the rotor blade changes. Too little lift makes power production impossible, too much of it results in overload of the drive train and the structures. [2] Wind turbines have a rated wind speed, at which they reach their rated power. Above this wind speed, the power output has to be reduced. It does not make sense to design a wind turbine for the highest wind speed possible, since the structures would be unreasonably heavy and expensive, and very high wind speeds occur only seldomly [28]. (In wind turbine design, the 50-year-gust is a typical size for extreme load calculation. [32])

There are two primary means to reduce power output of wind turbines: Stall and pitch-to-feather. Stall type turbines have blades that cannot rotate about their primary axis, whereas the blades of pitch type turbines can do this. They rotate (pitch) into the so-called feather position. It is possible to pitch blades actively into a stall position, but this does not provide any advantages over stall turbines with fixed blade angles.

Figure 2.6 shows the stall principle. The center part of the figure shows a blade section in normal operation, with incoming wind (green dashed lines) attaching to the profile. u is the rotational speed of the blade section, v_w the speed of the wind, and v_{eff} the effective speed at the blade. α is the inflow angle. A stall blade does not turn, but when v_w increases, so does α , and this change leads to a turbulent flow separation which reduces the power intake, see the right part of Figure 2.6.

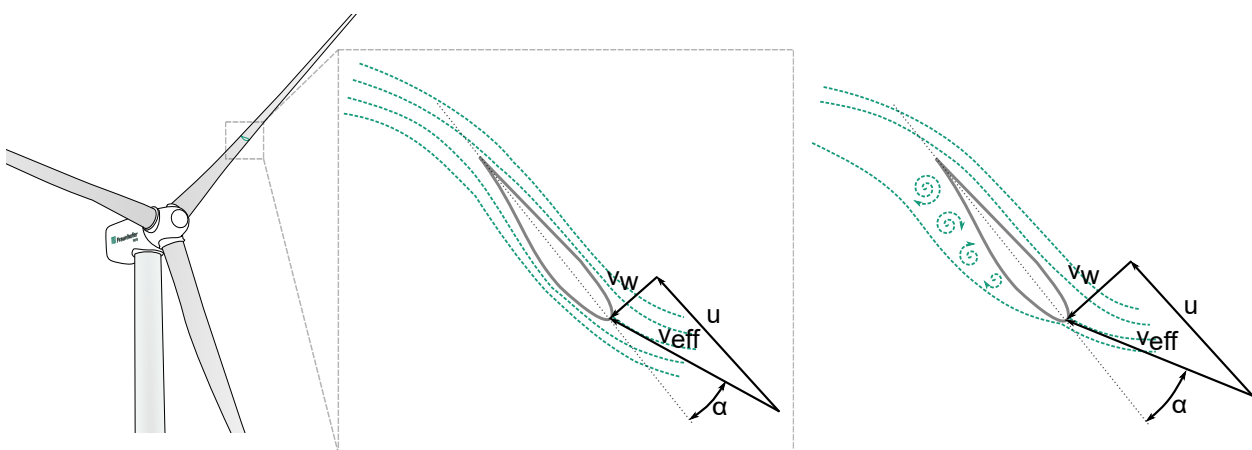


Figure 2.6: Stall principle: Attached flow in normal operation (center), separated flow in stall conditions (right)

With a pitch-controlled blade, the section itself rotates with its tip into the inflowing wind (see Figure 2.7). This reduces the inflow angle α . The flow is not separated, but lift is reduced. In Figure 2.3 of Section 2.1.2, the pitch angle is above 0° between 200 and 450 seconds. This behavior is due to the wind turbine controller pitching the blade(s) in the direction of the feather position to control the power output of the turbine.

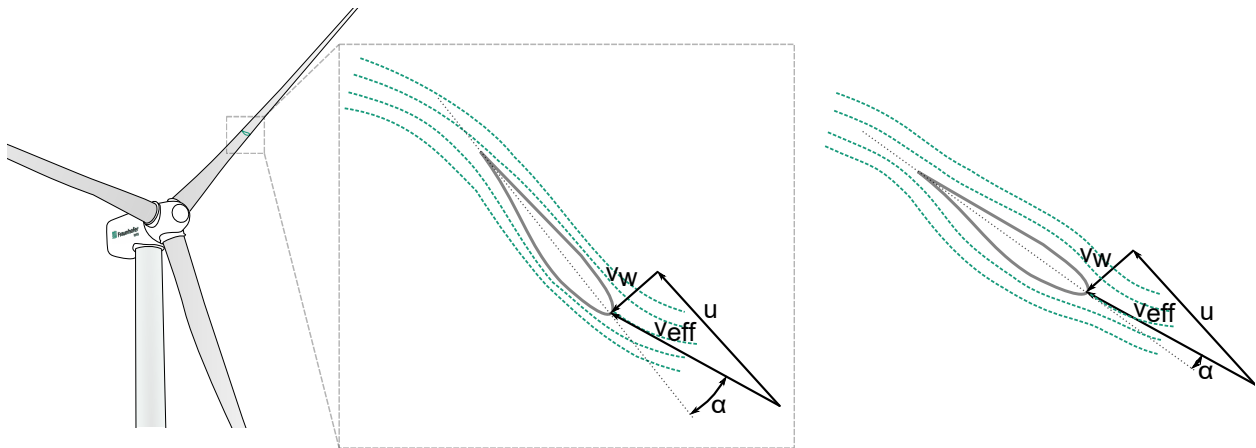


Figure 2.7: Pitch-to-feather principle: Attached flow in normal operation (center) and with a pitched blade (right)

Pitch-to-feather provides a smooth control over aerodynamically induced forces, whereas the flow of a stall blade does not separate at the exact same wind speed every time. This means a stall turbine needs to be designed in a way that it causes stall at the permissible load peak point (rated wind speed) under all circumstances. In consequence, the design stall point is set below this point, which results in causing stall below the rated speed in many cases. As the blades do not turn, stall turbines also have an increase in thrust forces at higher wind speeds, which pitch-to-feather turbines have not. The smooth control and the reduced thrust forces outweigh the more complicated mechanical system by far. These advantages make pitch-to-feather control the standard control of all newer turbines. [2]

Pitch control needs blades to turn around their primary axis. Pitch bearings and pitch drives (hydraulic or electric) provide this ability. Pitch bearings are the main subject of this thesis, and much more about them will follow in the next sections. To reduce the power output above rated wind speed, all three blades rotate to the same angle, thereby reducing the inflow angle at the blade sections and the lift. If they rotate about 90° , they reach feather position and produce virtually no lift. A collective pitch-to-feather is the primary braking mechanism of a wind turbine, and vital for the structural safety [1, 2]. This control goes by the name Collective Pitch Control (CPC).

The first pitch-to-feather turbines had mechanical links between the three blades that harmonized the pitch angle [1]. The major disadvantage of such a design is limited fail-safety. If the drive fails, there is no possibility to stop the turbine, and it is very certain it will destroy itself at wind speeds above rated. Current designs overcome this disadvantage with individual drives for each

blade. A failure of one drive does not endanger the structural safety of the entire turbine anymore. Each drive has a backup accumulator to allow pitching the blade to feather in case of power outages. [11, 32]

Given the individual pitch drives and the nature of the wind, which varies in speed and turbulence over the rotor area, it is elegant to think about Individual Pitch Control (IPC). Controlling the blades individually allows to reduce overall out-of-plane moments of the rotor and with it the loads on subsequent structures, at only small reductions in energy production. In Figure 2.3 of Section 2.1.2, the pitch angle is above 0° between 200 and 450 seconds and oscillates around varying mean values with a double amplitude of roughly 2° . The slower change of the mean value is the aforementioned power control, while the superimposed oscillations show the activity of the IPC. Bossanyi described how to implement this idea in commercial turbines in 2003 [13]. Later publications included inflow-measurement as a control input [36] and more details on extreme load reduction [37]. All IPC systems share the idea of small, individual adjustments of the blade angle to control loads.

It is not a little task to design the controllers for IPC, but since there are even published results on field tests [38], it is fair to assume that one adept engineering team can do it. When it comes to the pitch bearings, the situation is quite different. IPC changes the way pitch bearings move, the number of oscillations, their amplitudes and the loads. Knowledge on damage modes is limited, calculation methods are not available, and there is no substantial experience from field applications (more on this in later sections). IPC makes wind turbines more cost-effective, yet it is uncertain if pitch bearings withstand the new load spectrum.

2.1.4 IWT7.5 Reference Wind Turbine

Like in any other industry, intellectual property needs protection in the wind industry as well. Wind turbine manufacturers are not too keen on publishing detailed data about their turbines, in particular the aerodynamic properties of the blades, the controllers, and the aero-elastic models. Yet, many research projects (including those the present thesis bases upon) depend on such data. To overcome this issue, some research institutions established so-called reference turbine models. These are basic turbine designs whose details are publicly available so anybody can run aero-elastic simulations. The turbines do not exist in reality, and as resources for the development are limited, they do not reach the overall quality of commercial turbines. But they do incorporate the fundamental behavior and can include advanced controllers. The US National Renewable Energy Laboratory (NREL) [39], the Technical University of Denmark (DTU) [40] and the German Fraunhofer Institute for Wind Energy Systems (IWES) [41] published reference turbine models. This thesis bases upon the project HAPT (Highly Accelerated Pitch Bearing Tests). For various and obvious reasons, the model used within this project is the IWES one.

The IWES model goes by the name IWT7.5-164. IWT stands for IWES Wind Turbine, 7.5 refers to the nominal power P_r of 7.5 MW, and 164 to the rotor diameter D_{rotor} of 164 m. The turbine is a three-bladed, upwind rotor turbine and was designed as a nearshore-turbine for sites with relatively high wind speeds (IEC class A1). There are both CPC and IPC variants of the turbine.

Details of the turbine are part of the turbine documentation [42]. Together with Thomas and Schwack the author described the behavior of the CPC and IPC variants in [43]. Table 2.1 is taken from this reference and summarizes main characteristics of the turbine.

Table 2.1: Main characteristics of the IWT7.5.

Property	Symbol	Value	Unit
Hub height	h_{hub}	119.3	m
Specific power (per swept area)	ψ_{rotor}	355	W/m ²
Cut-in wind speed	V_{in}	3	m/s
Rated wind speed	V_r	11	m/s
Cut-out wind speed	V_{out}	25	m/s
Minimum rotational speed	Ω_{min}	5	rpm
Rated rotational speed	Ω_r	10	rpm
Rated tip speed	V_{tipr}	85.9	m/s
Design tip speed ratio	Λ_D	8.4	-
Tower mass	m_{tower}	1467.4	tons
Rotor-Nacelle-Assembly mass	m_{RNA}	536.6	tons

The revision of the turbine referenced in this work operates with a controller designed by the German wind turbine manufacturer Enercon. Enercon used the aero-elastic model of the IWT7.5, equipped with their own IPC-Controller, to run load simulations. This controller is a wideband IPC, designed to minimize loads as much as possible without limiting the movements of the pitch bearing. While the abovementioned IPC by IWES limits its activity to wind speed above rated wind speed, the Enercon IPC activates as well at wind speed slightly below rated speed. These speed regions contribute a large share to the overall fatigue loads of the turbine. The control variables are the loads in a non-rotating hub coordinate system, and the main objective is to minimize loads on the steel structures of the turbine as hub, machine frame, and tower. The controller respects fixed minimum and maximum values for the pitch angle. The minimum angle is -0.05° and the maximum angle is 90° .

2.2 Rolling Bearings

2.2.1 Principles and History

Bearings are machine elements that connect two parts of larger machines and allow movements in certain degrees of freedom while locking all others. Sliding bearings allow this by minimizing the friction between two surfaces, i.e. with a lubricant, while rolling bearings introduce rolling elements between them. The earliest known application of bearings were door hinges about 7000 BC [44]. Another assumed early application was the transport of heavy stone structures in ancient Egypt [45]. Most of the general designs of rolling bearings used today were introduced in the 18th century [44].

Pitch bearings of wind turbines allow the rotation of the blade about its primary axis and lock all other degrees of freedom. For this purpose, the bearings have two circular rings that share the same rotational axis. In case of a sliding bearing, the facing areas of the rings slide against each other. In case of a rolling bearing (see Figure 2.8), rolling bodies like balls or rollers roll on these faces, which are called raceways. The rolling bodies need to be equally distributed along the circumference of the raceway. This is achieved by individual elements between them, called spacers, or circumferential guides, called cages. In common bearings of both types, lubricants minimize the friction and protect the surfaces against corrosion. Usual lubricants are oils and greases, with water and solid lubricants being alternatives. In comparison to sliding bearings, rolling bearings have less frictional torque, but higher loads on the individual elements due to the smaller contact area. [46] The lower friction of rolling bearings motivated the present-day American Bearing Manufacturers Association (ABMA) to call themselves the Anti-Friction Bearing Manufacturers Association (AFBMA) in 1933 [47].

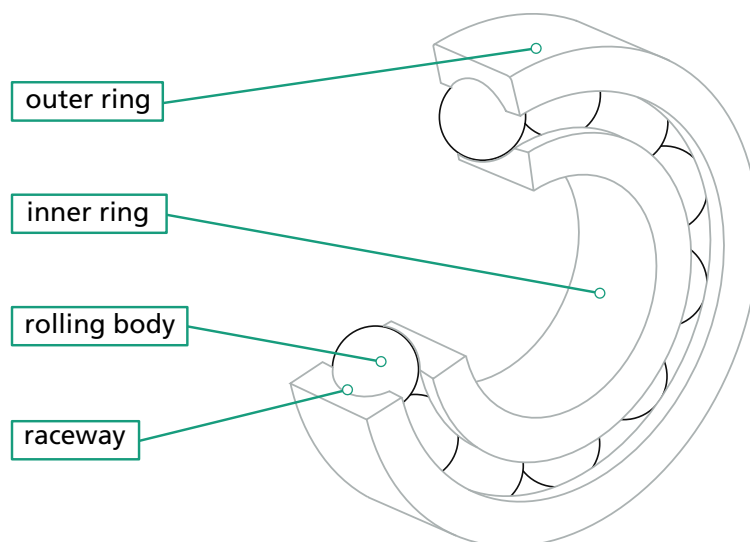


Figure 2.8: Rolling bearing with balls as rolling elements

2.2.2 Hertzian Calculation of Contact Parameters

When a force Q is applied to a contact of two bodies, it causes them to deform. A spherical contact – as we find it in a ball bearing – without load is a point contact, but when Q is applied, the deformation of the bodies creates a pressurized contact area (see center part of Figure 2.9). Under the load Q , the center of the smaller body moves towards the contact. This deformation has a nonlinear relation to Q , as the contact area becomes bigger with the applied force.

Hertz was the first to calculate spherical contacts and derive parameters like contact dimensions and contact pressure distribution [48, 49]. In a ball bearing, the pressurized contact area has the shape of an ellipse. The right part of Figure 2.9 shows such a contact ellipse with its height $2a$ and width $2b$. Hertz established that the pressure distribution has an ellipsoidal shape as well. The calculations are subject to some boundary conditions like frictionless contacts; homogeneous, isotropic materials; no plastic deformations; relatively small contact areas in comparison to the curvature of the bodies. Although these conditions do not apply in reality, the calculations deliver reasonably good results [50]. As a consequence of the ellipsoidal pressure distribution, the pressure calculations include solving ellipsoidal integrals. As there is no analytical solution to such integrals, common approaches use integral tables and interpolate between the values. Harris and Kotzalas present such an approach in their work *Rolling Bearing Analysis*, see [46]. Houpert [51] later used approximate functions to allow direct calculation of the characteristics and skip the interpolations. For individual contacts and whole bearings with low numbers of rolling bodies, finite element (FE) calculations are a common practice, especially since they can respect friction conditions in the contact, ball-cage interactions, and real raceway geometry. The later Section 2.5.1 covers FE calculations.

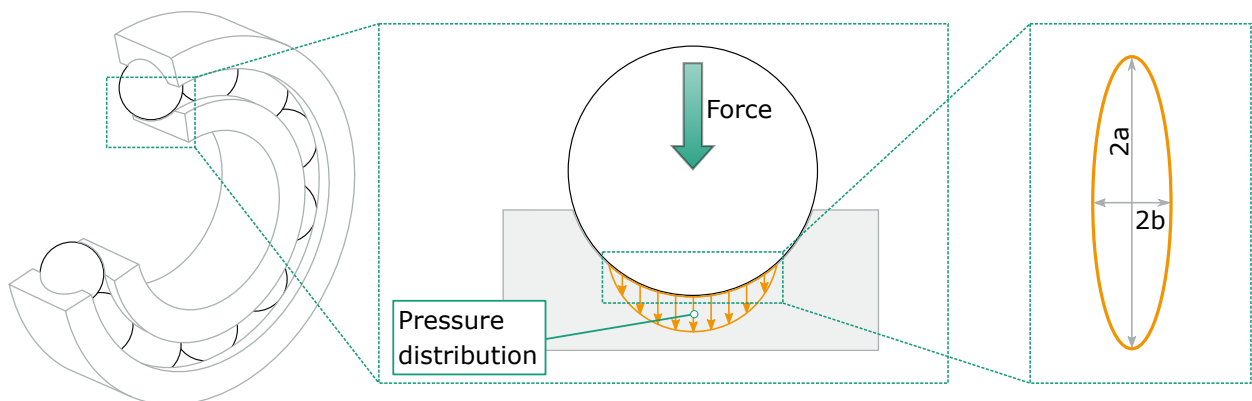


Figure 2.9: Hertzian contact area of a ball on a raceway

The later Section 2.3.4 describes the pitch bearing of the IWT7.5-164 reference turbine. The parameters of an individual ball/raceway contact of this bearing (see Table 2.2) are part of the exemplary contact calculation developed in this section. This calculation follows the procedure described by Houpert in the introductory part of [51], which refers to Harris and Kotzalas [46].

Table 2.2: Material and geometrical parameters of the IWT7.5-164 pitch bearing

Property	Sign	Value	Unit
Ball size	D	80	mm
Pitch diameter	d_m	4690	mm
Osculation (both rings)	ϕ	0.5319	-
Young's modulus (ball and raceway)	E_1, E_2	210 000	N/mm ²
Poisson ratio (ball and raceway)	ν_1, ν_2	0.3000	-
Contact angle	α_c	45	°

In Table 2.2, the term osculation (ϕ) describes the ratio between the radius of the ball and the radius of the raceway. More specifically, it is the ratio of the radius r of the raceway in a direction transverse to the direction of rolling to the diameter D of the rolling element. In ball bearings, the radius of the raceway is always slightly larger than the radius of the ball to reduce slip and prevent jamming of the bearing. In case of this bearing, the overall diameter is much larger than the ball diameter and the osculation is the same on inner and outer ring.

To facilitate the following calculations, we now transform the contact of two curved bodies into an equivalent contact of one curved body on a flat plane. Equation (2.1) gives the combined Young's modulus E . Equations (2.2) to (2.4) define radii of the two contact partners, both in rolling direction x and transverse to it (y). Since one of the contact partners is a perfect sphere, the definition of the contact radii in both directions is identical and given in Equation (2.2). Equation (2.3) defines the raceway radius at the center of the contact in x . The positive sign is used for the outer raceway. Equation (2.4) gives the radius of the raceway transverse to the rolling direction. Equation (2.5) defines the curvature sum. Last before the interpolation step, Equation (2.6) gives the curvature difference. Here, the negative sign applies for the outer raceway. Table 2.3 lists the results based on the contact parameters listed in Table 2.2.

$$\frac{1}{E} = \frac{1}{2} \cdot \left(\frac{1 - \nu_1^2}{E_1} + \frac{1 - \nu_2^2}{E_2} \right) \quad (2.1)$$

$$R_{x_1} = R_{y_1} = \frac{D}{2} \quad (2.2)$$

$$R_{x_2} = \frac{d_m}{2} \pm \cos(\alpha_c) \cdot \frac{D}{2} \quad (2.3)$$

$$R_{y_2} = R_{x_1} \cdot \phi \quad (2.4)$$

$$\Sigma\rho = \frac{2}{R_{x_1}} + \frac{1}{R_{x_2}} - \frac{1}{R_{y_2}} \quad (2.5)$$

$$F(\rho) = \frac{\frac{1}{R_{x_1}} - \frac{1}{R_{x_1}} \pm \frac{1}{R_{x_2}} + \frac{1}{R_{y_2}}}{\Sigma\rho} \quad (2.6)$$

Table 2.3: Transformed contact parameters of IWT7.5-164 pitch bearing

Property	Symbol	Value	Unit
Combined Young's modulus	E	230769	N/mm ²
Ball radius	R_{x_1}, R_{y_1}	40	mm
Outer raceway radius in x	$R_{x_{2O}}$	2373.2800	mm
Inner raceway radius in x	$R_{x_{2I}}$	2316.7200	mm
Raceway radii in y	$R_{y_{2O}}, R_{y_{2I}}$	42.5500	mm
Curvature sum outer raceway	$\Sigma\rho_O$	26.9207	1/m
Curvature sum inner raceway	$\Sigma\rho_I$	26.9309	1/m
Curvature difference outer raceway	$F(\rho)_O$	0.8573	-
Curvature difference inner raceway	$F(\rho)_I$	0.8886	-

The curvature difference is now used to get the dimensionless parameters a^* , b^* and δ^* from a table with solutions of complete elliptical integrals. Table 6.1 of Harris and Kotzalas [46] provides such solutions. Between the given values, we use linear interpolation. Table 2.4 gives the parameters for the outer and inner raceway.

Table 2.4: Dimensionless contact parameters of IWT7.5-164 pitch bearing

Sign	Value
a_O^*	2.6617
b_O^*	0.5006
δ_O^*	0.7363
a_I^*	2.9675
b_I^*	0.4719
δ_I^*	0.6959

With these parameters, it is possible to calculate the semimajor axis a and semiminor axis b of the contact, the maximum contact pressure P_{max} and the contact deformation δ for a given force Q acting on the ball, see Equations (2.7) to (2.10).

$$a = a^* \cdot \left[\frac{3Q}{2\Sigma\rho} \cdot \frac{2}{E} \right]^{(1/3)} \quad (2.7)$$

$$b = b^* \cdot \left[\frac{3Q}{2\Sigma\rho} \cdot \frac{2}{E} \right]^{(1/3)} \quad (2.8)$$

$$P_{max} \approx \frac{1.5Q}{\pi ab} \quad (2.9)$$

$$\delta = \delta^* \cdot \left[\frac{3Q}{2\Sigma\rho} \cdot \frac{2}{E} \right]^{(2/3)} \quad (2.10)$$

Table 2.5 lists these parameters for a load Q of 47025.16 N. This load results in a contact pressure of exactly 2000 MPa at the inner ring. The dimensions of the ellipse are given in full axes instead of semiaxes, as these values are more meaningful for the later sections of this thesis. The values deviate only very little for the inner and the outer ring. Any following results will therefore be given for the inner ring only.

Table 2.5: Hertzian contact parameters of IWT7.5-164 pitch bearing

Symbol	Value	Unit
$2a_O$	16.8065	mm
$2b_O$	2.6726	mm
P_{max_O}	1999.4906	MPa
δ_O	0.0751	mm
$2a_I$	16.8043	mm
$2b_I$	2.6723	mm
P_{max_I}	2000.0000	MPa
δ_I	0.0751	mm

Repeating the calculations for various values from 0 to the aforementioned 47025.16 N yields force-dependent curves for dimensions and pressure. Figure 2.10 shows the nonlinear deformation over the applied force. At a contact pressure of 2000 MPa, the center of the ball moves 0.075 mm towards the contact with the raceway. For the later concepts in this work, the width of the contact ellipse $2b$ and the deformation δ are of particular importance.

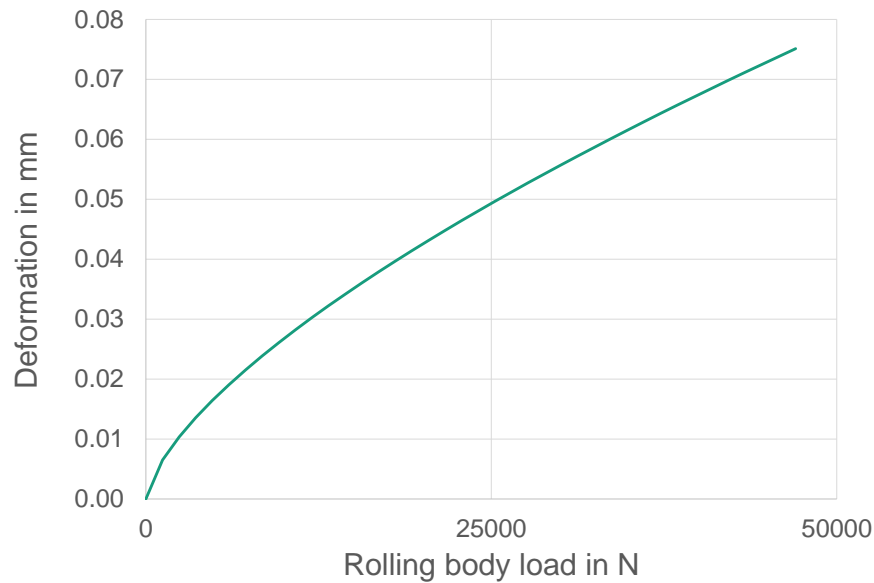


Figure 2.10: Deformation over contact force

2.2.3 Kinematics and Slip

In most rotatory bearing applications, one of the bearing rings is stationary, while the other rotates. This is the case for pitch bearings as well; the ring connected to the hub does not rotate about its primary axis, while the ring connected to the blade can rotate. In Figure 2.3 of Section 2.1.2, the pitch angle equals the position of the ring that connects to the blade. In case of the IWT7.5-164, this is the inner bearing ring.

Under the assumption of a perfect rolling motion, the distance x covered by the ball on the raceway relates to the pitch angle θ (in rad) as follows:

$$x \approx \frac{d_m \cdot \theta}{4} \quad (2.11)$$

The relation is approximate, as d_m is not the exact diameter of the contact between inner ring and ball. Due to the large diameters of pitch bearings, the error made with this approximation is very small, and for the purpose of this work, it is not necessary to execute exact calculations. Similar to the relation of the travels, the speed of the ball \dot{x} is half the speed of the ring. Figure 2.11 visualizes this concept.

A perfect rolling motion is without relative movement between the rolling partners. A relative movement is called slip. Balls in rolling bearings always move with slip, for various geometrical and tribological reasons. Slip further influences the relation in Equation (2.11). [46] Schwack

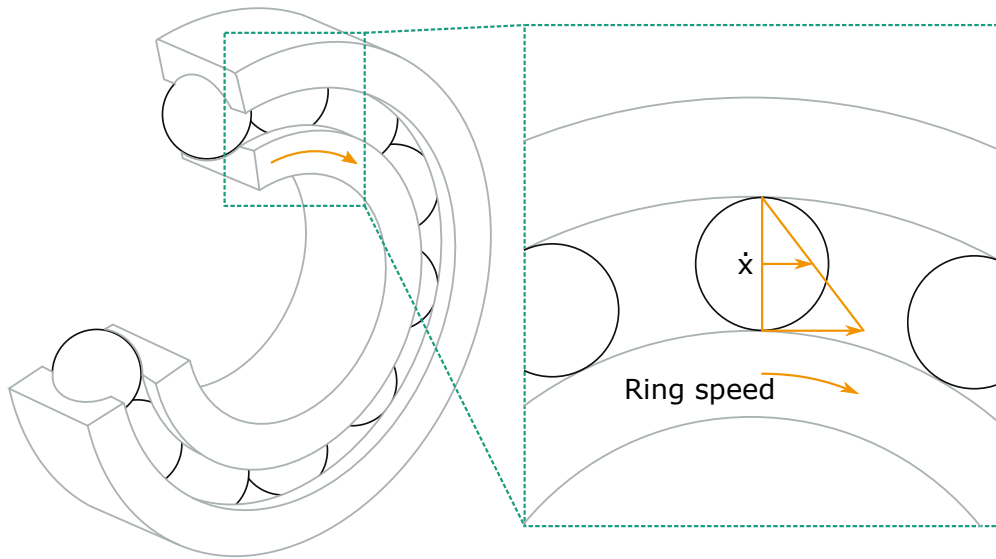


Figure 2.11: Relation of ring movement and ball movement

simulated slip in an angular-contact ball bearing in [52]. This work limits to simulations with homogeneous friction coefficients, but it indicates that slip does not influence the travel x during an oscillation in a way that needs to be represented in the calculation.

Section 2.2.2 introduced the width $2b$ of the contact ellipse. The ratio of the distance x to this width ($x/2b$) is a dimensionless parameter that describes the travel of a movement. $x/2b$ is independent of the bearing dimensions and allows to compare the oscillations of bearings with different diameters. Later sections of this work will make extensive use of this ratio, and Table 2.6 lists values of x and $x/2b$ for different pitch angles θ . Figure 2.12 shows different values of $x/2b$.

Table 2.6: Ball travels x for different pitch angles θ of IWT7.5-164 pitch bearing

Pitch angle in degree θ	Ball travel in mm x	Ratio travel/ellipse width $x/2b$
0.13	2.66	1.00
0.20	3.99	1.49
0.39	7.98	2.99
1.57	32.13	12.03
3	61.39	22.99
10	204.64	76.64
20	409.28	153.29

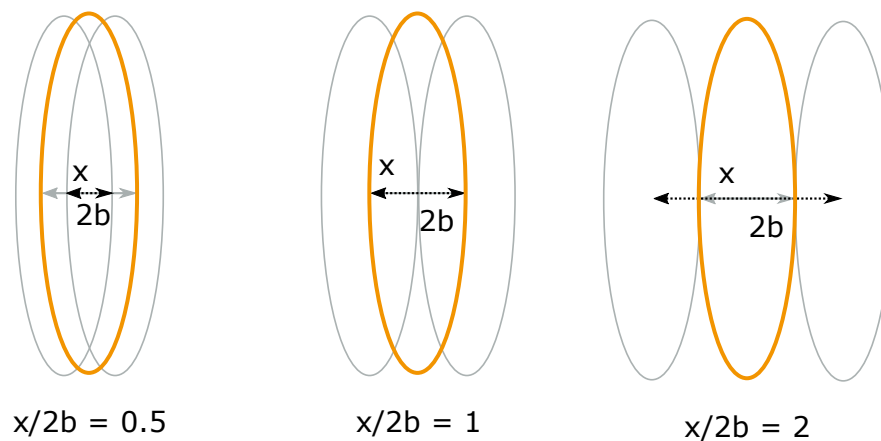


Figure 2.12: Different $x/2b$ ratios

2.2.4 Grease Lubrication

Lubricants serve various purposes in a bearing. They reduce friction, keep oxygen and dirt from the surfaces of rolling bodies and raceways, and can, as a lubricant film, separate the rolling bodies and the raceways from each other. The state of a complete separation is called full lubrication regime. This state is desirable, as it minimizes wear on the surfaces of the contact partners. [46]

The most important lubricants for rolling bearings are grease and oil. For obvious reasons, it is paramount for a lubricant to stay within the bearing. This is achieved with outer housings or sealings between the bearing rings. The most important advantage of grease over oil is its semi-fluid consistence, which allows to use less elaborate sealings. This (economical) advantage makes grease the most widely used lubricant for bearings. [46] Pitch bearings are particularly large and subject to substantial deformations, as such an effective oil sealing would come at prohibitive costs. As most other bearings, they use grease as well.

Grease is a solid to semi-fluid dispersion of a thickening agent and a liquid lubricant. While the way oil acts as a lubricant, i.e. how it gets into the contact between ball and raceway, is very well understood, it is not completely clear in which ways grease lubricates the contact. In particular, the interaction between thickener and oil and the question if and when thickener enters the rolling contact are still to be answered. [46,53] It is possible to calculate the lubricant film thickness for an oil-lubricated bearing with high accuracy [54,55], but as the role of the thickener is not well understood, this is not the case for grease lubrication [56].

Besides thickener and base oil, commercially available greases also contain additives. Additives can serve various purposes. Common purposes are corrosion inhibition and extreme-pressure / anti-wear (EP/AW) protection. EP/AW additives are generally based on sulfur and phosphorus. They react with the raceway and rolling body surfaces and form less reactive tribolayers. [46,57] The buildup and deterioration of these layers can currently not be calculated analytically, but have

to be determined in tests [46]. The additive-steel pairing determines the chemical process, while temperature, pressure, and time influence the process. [58,59]

2.3 Pitch Bearings

2.3.1 Bearing Types

Pitch bearings of wind turbines connect the rotor hub with the rotor blades. Figure 2.13 shows the location of one pitch bearing (orange) and its coordinate system. The coordinate system is fixed to the hub, i.e. it does not turn around the z-axis with pitch movements. A load in z-direction is called an axial load, loads in x and y are radial loads.

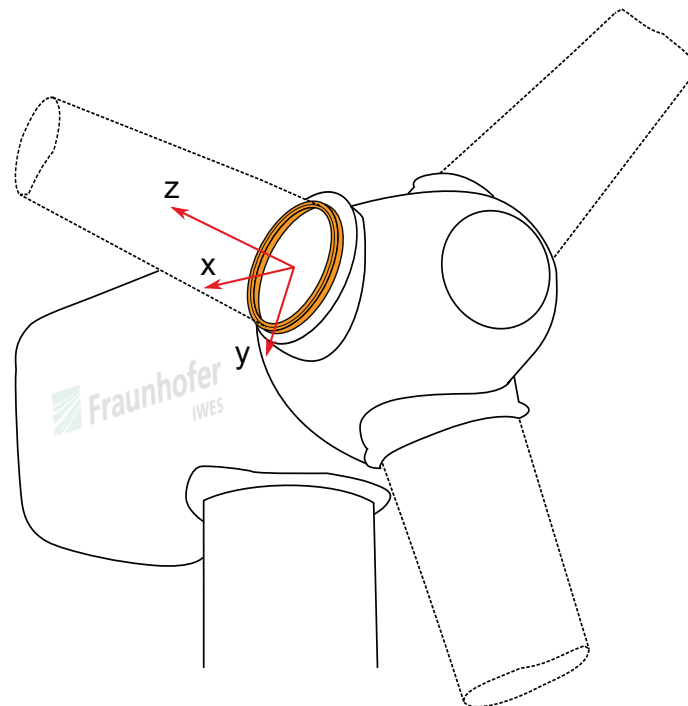


Figure 2.13: Pitch bearing in a wind turbine (orange) and coordinate system (red)

Pitch bearings are grease-lubricated rolling bearings. Rolling bearings of the size of pitch bearing are typically called slewing bearings. Besides pitch bearings, they are found in heavy machinery like cranes, excavators and similar. To the knowledge of the author, alternative concepts like sliding bearings did not get past the state of patents [60] or graduate theses [61]. Commercially available types include four-point contact ball bearings with one or two rows, three-row roller bearings and mixed types (with their commercial name T-Solid [62]) [63–65]. Figure 2.14 shows these three types. The orange arrows show possible force vectors between rolling bodies and

raceways. Three-row roller and T-Solid both have two axial rows (rows that carry axial loads) and one radial row. In a four-point contact, every row carries both axial and radial loads. All types have bolt holes in each ring (one of which is visualized in Figure 2.14). Bolts connect the pitch bearing to the blade hub and the blade. Three-row bearings have one split ring (in Figure 2.14, this is the outer ring), as this allows the assembly of the bearings. Four-point bearings do not have split rings. Instead, fill plugs on each row allow to put in the balls.

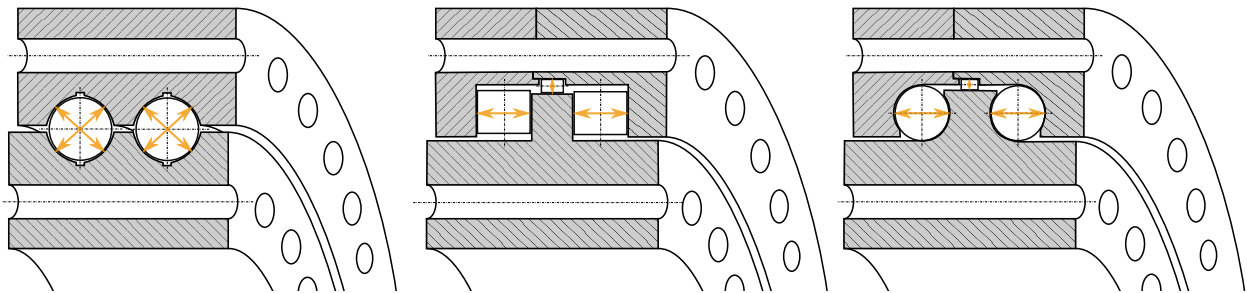


Figure 2.14: Pitch bearing types: Four-point contact (left), three-row roller (center), T-Solid (right)

Four-point bearings have been widely used as pitch bearings over the last decades [1]. Three-row roller and T-Solid bearings provide a higher overall stiffness and a longer rolling contact fatigue (RCF) lifetime at identical diameters [63–65]. Besides these advantages, they have a higher price, are heavier, and, due to the axial orientation of their rows, they have different slip conditions in the contact. The different slip conditions can be beneficial or harmful to the bearing raceways (more in the later section on raceway wear). The axial rows of the three-row bearings have a contact angle of 90° , four-point contact bearings have initial contact angles of $40 - 45^\circ$. The free contact angle β is the change of the initial contact angle under load (see Figure 2.15 for a definition of the contact angle).

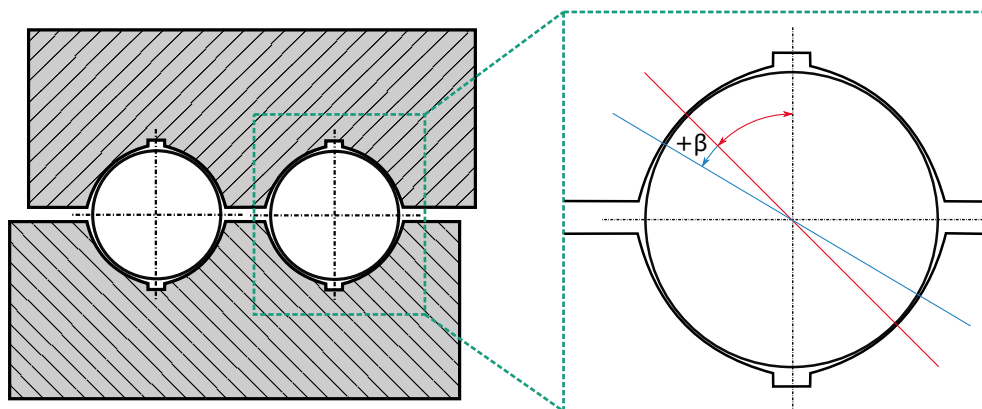


Figure 2.15: Contact angle definition in a four-point contact bearing

The name four-point bearing stems from the unloaded condition, in which the ball has contact to four raceways. Due to their contact angle they transform any pure axial or radial load into

a combination of the two. In loaded conditions, the ball usually is in contact with two of the four raceways. With inhomogeneous load distribution along the circumference and unequal load splitting between the rows, this leads to ovalization and tilting of the bearing rings. The initial contact angle changes. Schwack and Stammeler described the influence of outer loads on the contact angle in [5]. Figure 2.16 shows an exaggerated section view of deformed bearing rings.

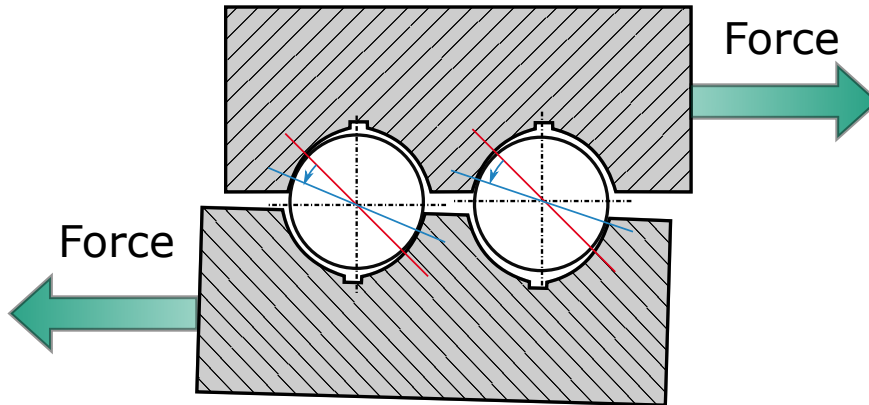


Figure 2.16: Four-point contact bearing deformation under axial load

Bearing rings of pitch bearings are usually made of 42CrMo4-type steels. The rolling bodies are from 100Cr6. The rings need additional hardening to withstand the contact pressures. Due to size, surface hardening by induction is the usual procedure. 42CrMo4-type steels display good characteristics for this process. The balls are through-hardened. The non-hardened fraction of the ring material is called core. After the hardening process, the rings are turned and sometimes additionally grinded to achieve the final geometry of the raceways.

Pitch bearings usually have a pre-tension in the contacts. One of the reasons for this is to avoid standstill marks (see the later section on damage modes). In four-point bearings, the pre-tension is achieved by putting in balls with a slightly larger radius than the space between the rings. In roller bearings, the pre-tension is achieved by bolting the rings to their interface parts – the pre-tension of the bolts is transferred to the rollers. The bolting of a four-point bearing slightly increases the pre-tension of the rolling contacts as well.

Commercial pitch bearings are available with cages or individual spacers between the rolling bodies [63–65].

2.3.2 Operating Conditions

Section 2.1 on wind turbines introduced the turbulent inflow of the wind and the resulting dynamics of the loads. The pitch bearings are at the root of the blade and are subject to the same load characteristics. Figure 2.17 shows the load components of a pitch bearing. M_y and M_x are the dominating components. M_y results mainly from the thrust force of the rotor blade and to minor parts from weight and inertia components. In normal operation, M_y has a slowly-changing mean

value with overlaid higher dynamic components (cf. 2.3). M_x results mainly from the weight of the rotor blade and the aerodynamic lift. In normal operation, the lift component has a positive mean value which offsets the larger sinusoidal weight component (cf. 2.3 as well). M_z is of far smaller magnitude than M_y and M_x , and the sources can be weight and aerodynamics, depending on the blade design. F_x and F_y are the radial bearing forces. F_x is connected to M_y , F_y to M_x . F_z is composed of the centrifugal forces (in rotation) and the weight. These two give it a similar shape to M_x (sinus with offset mean value). Figure 2.18 shows example time series with all load components.

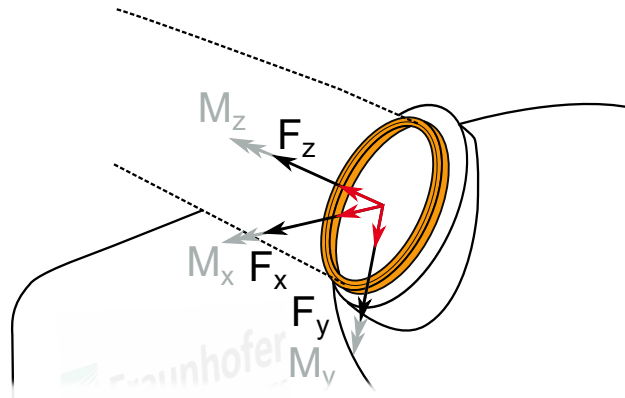


Figure 2.17: Load components of a pitch bearing

The bending moments M_x and M_y translate into axial forces at the blade root (see Figure 2.19). Together with F_z , they are the dominating load of a pitch bearing. The three-row bearing types in Figure 2.14 have larger rolling bodies in the axial rows than in the radial rows for this reason.

The loads act on the bearing while it executes the pitch movements. The pitch movements, i.e. the changes of the pitch angle θ are oscillatory in nature. As the wind changes, the amplitudes and frequencies of the movements change as well. For the purpose of this work, it is beneficial to categorize different patterns of movements. Figure 2.20 visualizes θ over time for different movement patterns. Please note that pitch drives are usually limited in rotatory speed, and most movements look more like ramps than like sinusoidal movements.

1. Similar amplitudes with similar mean values or similar amplitudes with identical lower values
2. Large amplitudes in a series of small amplitude oscillations
3. Varying amplitudes and mean values
4. Pauses

Type 1 is a pitch activity below rated speed of the wind turbine. The target pitch angle is close to 0° , and small oscillations control the loads of the turbine. Figure 2.21 shows this movement for all three blades. The phase offset between the three blades is typical for IPC. This movement is taken from the IWT7.5-164 reference turbine with the Enercon controller. The Enercon controller does not allow pitch angles smaller than -0.05° . The upper turning point of each movement

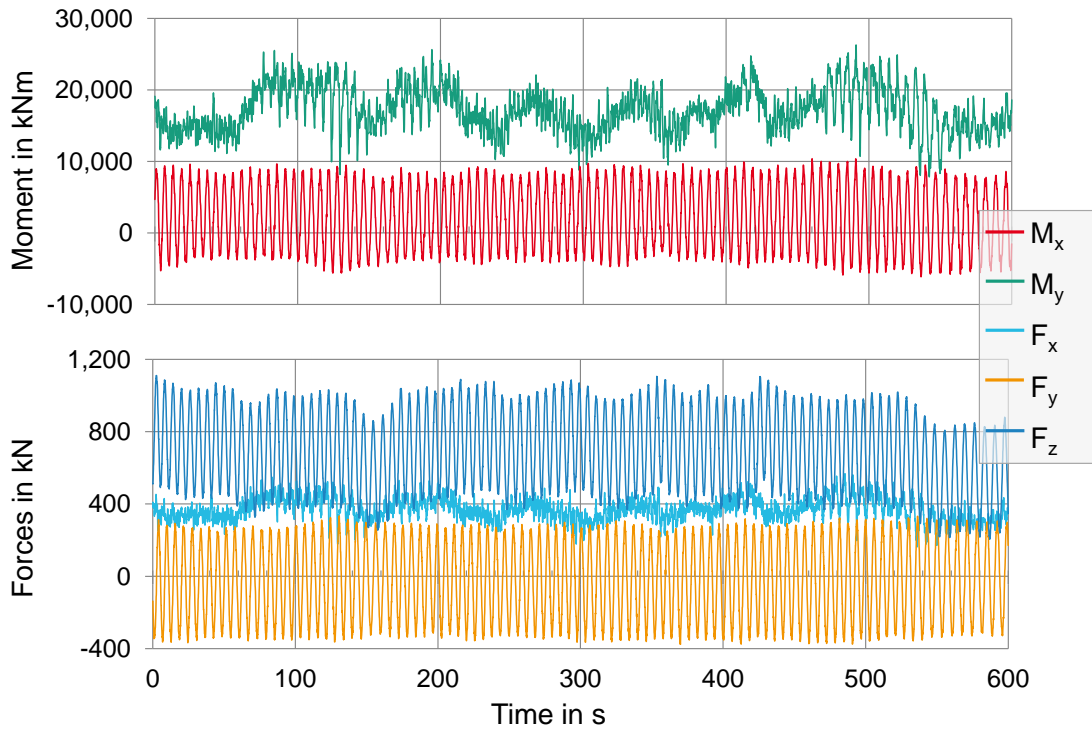


Figure 2.18: Time series with bending moments and forces

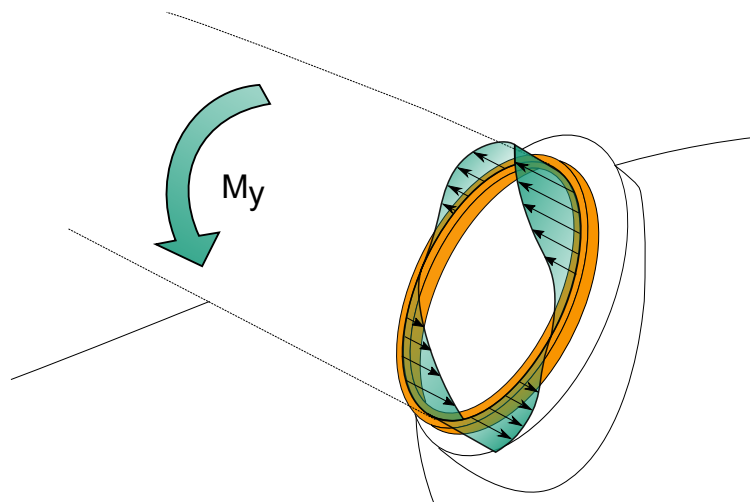


Figure 2.19: Translation of a bending moment to axial forces at the blade root



Figure 2.20: Movement patterns of pitch bearings

is determined by the IPC controller and varies. The constant lower turning point and the small amplitudes, however, lead to similar damage modes as oscillations with constant amplitudes and mean values (see the later sections on wear damage modes, Section 2.4.3, and scaled bearing tests, Section 4).

Type 2 is a reaction of a wind turbine to a significant increase in the mean wind speed. The CPC changes the pitch angle of all three blades to control the power output of the generator. Once the wind speed decreases again, the overall pitch angle approaches 0° again. This movement type is very rare in real wind turbines with IPC, because the IPC is active during gusts as well and adds small, overlaying oscillation to the longer movement. These small movements interrupt the long movement.

Type 3 is a combination of CPC and IPC at wind speeds above rated wind speed (see Figure 2.22). The CPC executes slower changes of the mean value, while the IPC overlays shorter oscillations. This movement is taken from the IWT7.5-164 reference turbine with the Enercon controller as well.

Type 4, the pauses, happen at very low wind speeds or in idling mode. The pitch bearing stands still.

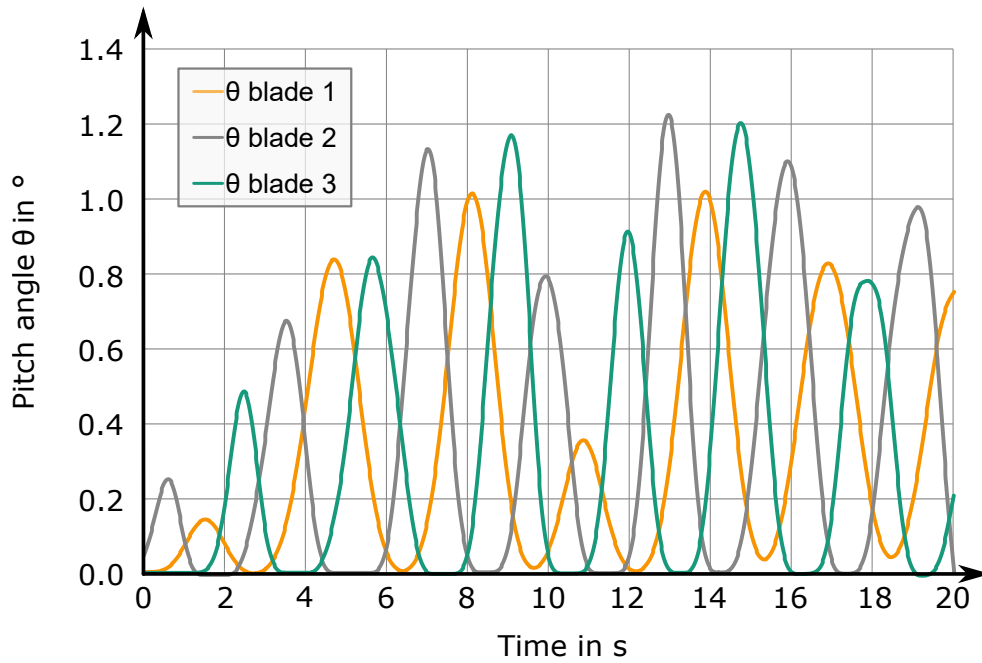


Figure 2.21: Pitch movement pattern of type 1

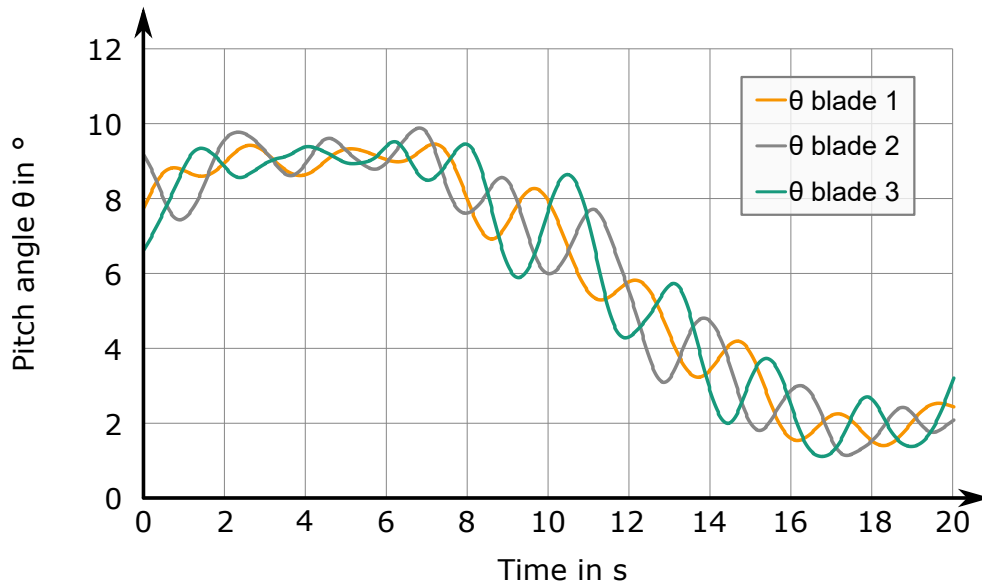


Figure 2.22: Pitch movement pattern of type 3

2.3.3 Interfaces

Pitch bearings interface with rotor blades and rotor hubs. In most designs, additional stiffener elements between blade and bearing or hub and bearing limit the bearing rings' deformation under load. The main purpose of the blades is to convert the energy of the wind into lift forces that make up the rotor torque. At the same time, they need to withstand the wind loads, the dynamics of the turbine and their own weight. Blade material is, apart from historical exceptions like the aforementioned Growian, a combination of fiber-reinforced plastics and foam or balsa wood. Fibers are glass fibers or carbon fibers, depending on the structural requirements. [1]

Figure 2.23 shows a cross section of a blade. The outer form is the aerodynamic profile that generates lift. Two spar caps from several layers of reinforced plastic provide the necessary stiffness to cope with the bending moments of the blade. The direction of fiber layers is mostly uniaxial in the direction of the z -axis. Two shear webs provide further stability. Spar caps and shear webs provide the structural integrity of the blade. Most blades are produced as two half shells which are bonded together in the later process. Bond positions are at the ends of the shear webs and at the leading and trailing edge of the blade. Except for the edges and the area of the spar caps, structural requirements are rather low, and sandwich material helps to make up a stable, yet lightweight outer form of the cross section. [1, 2]

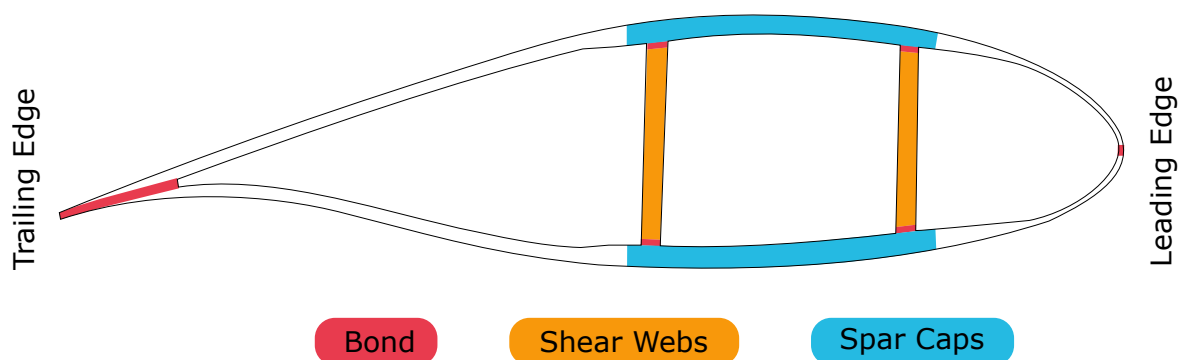


Figure 2.23: Cross section of a blade with functional elements

Towards the blade root, the aerodynamic profile converts into a circular shape that connects with the bearing. Bolts connect blade and bearing, and the blade needs to provide a thread for the bolts. The possible solutions for this are T-Bolts or inlays (see Figure 2.24). The blade root consists of several layers of fiber-reinforced plastic, giving it quasi-isotropic material properties. This makes it possible to cope with the high, complex loads in this area and provide the interface to the bolts. The first few meters of a blade usually make up a significant portion of its weight. [1, 2]

The spar caps transmit most of the load to the blade root. Figure 2.19 shows how this is transformed into axial loads. The characteristic of the load distribution is determined by the structural elements of the blade and differs from the load distribution of an ideally stiff tube

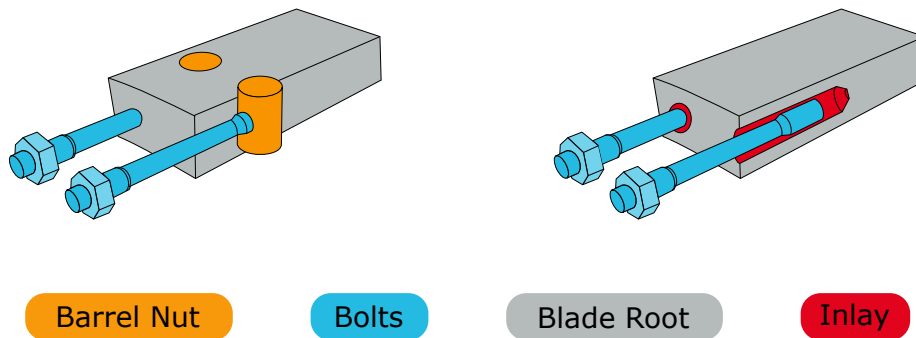


Figure 2.24: T-Bolt and inlay solution for blade root bolts

(see Figure 2.25). In case of an ideally stiff tube, the load distribution along the circumference (blue fill in Figure 2.25) would have a sinusoidal shape. In case of a blade, the highest load is aggravated by the structural elements, whereas the lower loads are alleviated (green fill in Figure 2.25). Recent works by Baust have shown that the detailed layout of the structural elements has little influence on the characteristic of this load distribution. All blades show a similar behavior, no matter the design details of the structure. No blade shows the behavior of a stiff tube. [66]

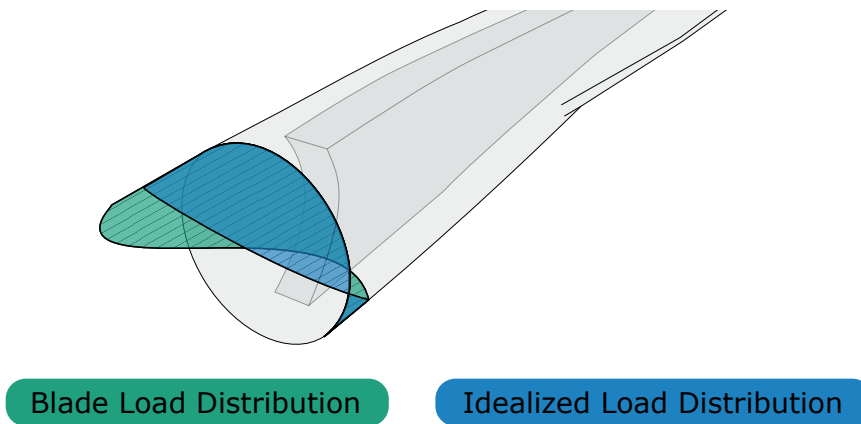


Figure 2.25: Load distribution caused by a bending moment: blade root vs. ideally stiff tube

In addition to the characteristic distribution of axial loads, blade roots tend to ovalize under bending moments. The ovalization is commonly counteracted by stiffener plates between blade and blade bearing. Without such plates, the ring deformation, especially of four-point bearings with an inner-ring blade mount, would reach impermissible magnitudes under operational loads. Blade ovalization, bolt interfaces and axial load distribution form the set of characteristics that determines the blade–pitch bearing interaction. The aerodynamic and structural design of the blades is a highly interesting and challenging domain, but as it is not of particular concern for this

work it will not be covered here. The books of Burton [2] and Hau [1], cited previously in this section, provide a good starting point to get acquainted with this field.

On the other side of the bearing, the rotor hub provides the mounting flanges for all three blades. Rotor hubs are commonly casted steel parts – as an exception one can again refer to the now well-acquainted Growian with its welded hub design. They come in two main design types: star and ball. [1] Figure 2.26 shows these two types. The difference is the shape of the material between the blade flanges, which looks like a ball for the right part of the picture. Commonly, the hub diameter is kept as small as possible, although this results in higher overall costs due to the slightly longer blades. The smaller hub is less prone to fatigue failure and has a reduced weight. [67] Hubs are made of isotropic material, but the stiffness at the bearing flanges is not homogeneous. A hub has the highest stiffness at the interface with the main shaft of the drive train, and the lowest at the opposite side. Between those extremes, geometric disturbances like pitch drive mounts and similar influence the stiffness distribution. [68]

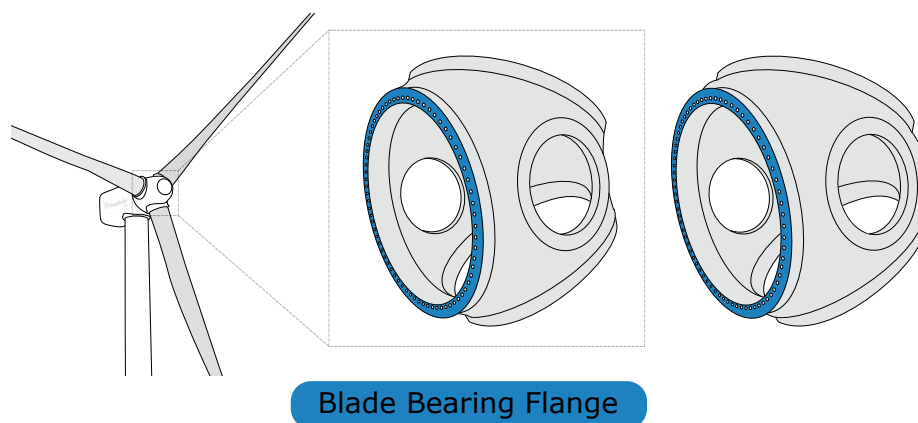


Figure 2.26: Star (left) and ball (right) type hub designs

To provide a stiffer surrounding for the pitch bearing, additional steel elements are part of some designs. Stiffener plates, i.e. flat discs mounted between blade and bearing and/or hub and bearing, limit ovalization of the rings, spacer rings spread the load more equally and limit tilting of the rings. Figure 2.27 shows a possible arrangement of such elements. They are commonly made of non-alloy steel. The application of stiffener elements depends on the design of the turbine.

2.3.4 The IWT7.5 Pitch Bearing and its Interfaces

In this thesis, the IWT7.5-164 reference turbine, introduced in Section 2.1.4, provides the environment for the design of a full acceptance run of a pitch bearing. An acceptance run results in a clear indication of the test item's suitability for the later application. The IWT7.5-164 is a virtual turbine, and as with most other reference turbines, there is no detailed design of all machine elements available. To execute a full acceptance run of a bearing, the following components need to be designed:

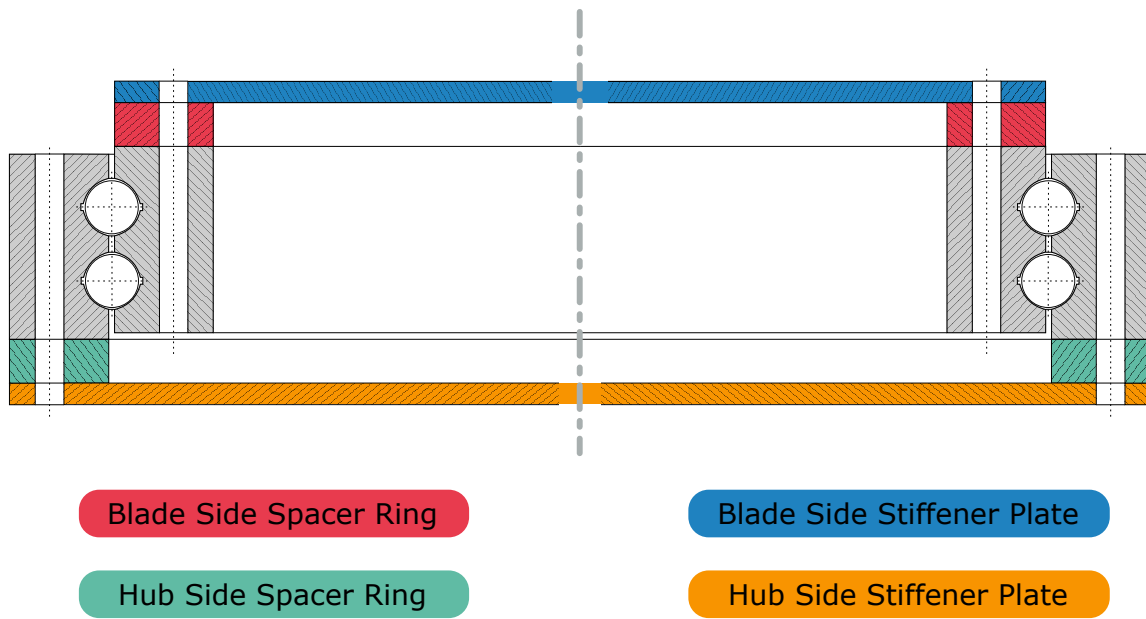


Figure 2.27: Pitch bearing with possible stiffener elements

- The pitch bearing itself
- The hub (limited to the stiffness properties)
- The blade (limited to the properties listed in the section before: bolt interface, ovalization, load distribution)
- Stiffener elements
- Pitch drive

The pitch bearing of the IWT7.5-164 is a four-point contact, double-row ball bearing. The German bearing manufacturer IMO designed the bearing specifically for this virtual reference turbine, its type designation is 12480. Figure 2.28 shows a section view of the bearing, and Table 2.2 of Section 2.2.2 and Table 2.7 list additional properties. Schwack and the author published the properties in other works as well [4, 5, 43]. The bearing has a segmented steel cage, the osculation at the inner and outer ring are the same. The inner ring connects to the blade. The pitch drive is an electrical motor with a gearbox, and the inner ring consequentially has gears to interface with this drive. The bolts of both rings are M42 bolts.

The hub is a ball-shaped basic design by Schwack. [67] Figure 2.29 shows a sketch of the hub, and Table 2.8 lists the main properties. The hub radius refers to the distance of the rotational axis to the center of the bearing flanges.

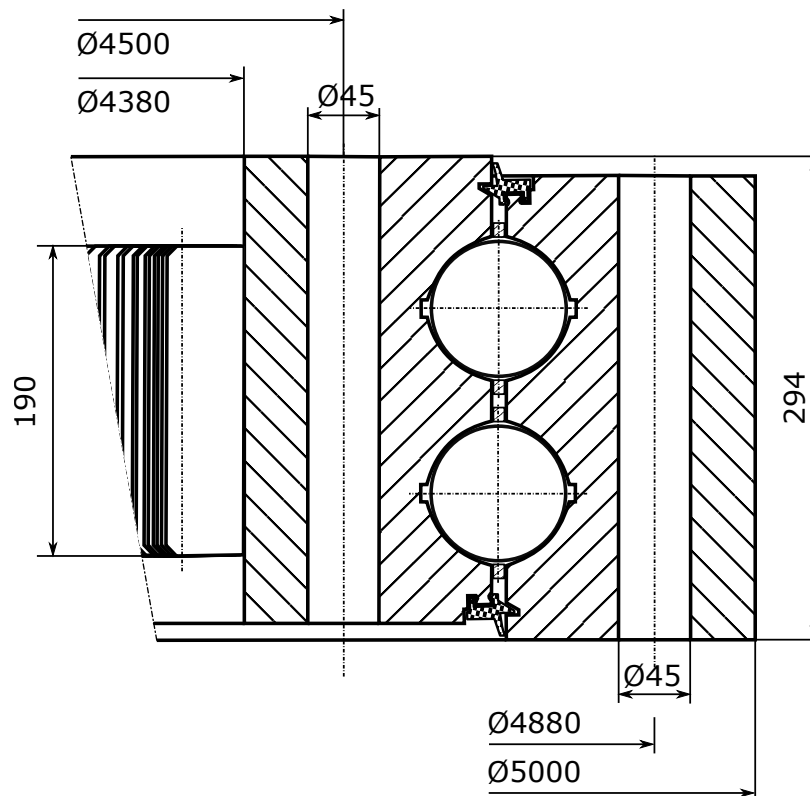


Figure 2.28: Type 12480 IMO pitch bearing section view

Table 2.7: Additional characteristics of the 12480 pitch bearing

Property	Value	Unit
Weight	9.3	tons
Fill plug diameter	90	mm
Ball count per row	147	-
Gear module	20	-

The hub design is rudimentary as only the stiffness properties are of interest for this work. In particular, it does not contain any interfaces for pitch drives or other technical systems, and the bearing arrangement (two main bearings on a kingpin) might provide several design challenges at later stages. The hub was designed against extreme loads.

For the purpose of this work, it was not possible to use the outer shape of the blade of the IWT7.5-164 turbine. The original blade has a blade root diameter of 4 m, and during the design phase of the bearing it was determined that this diameter does not suffice to transfer the maximum

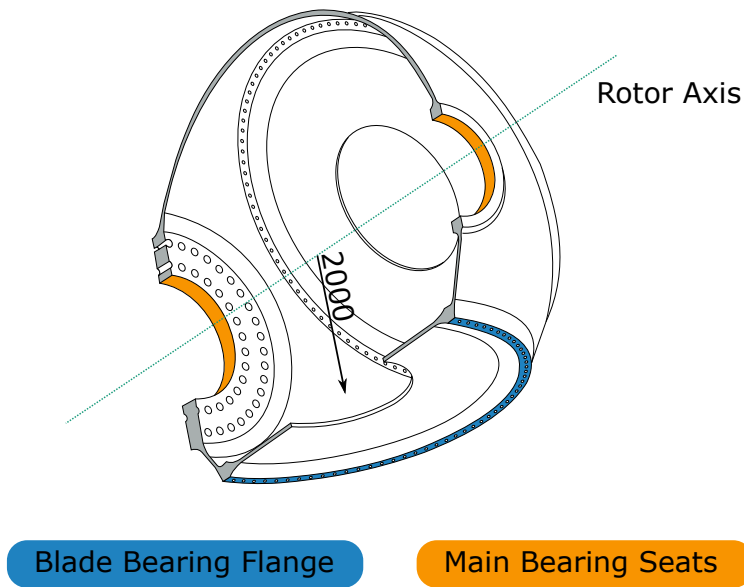


Figure 2.29: Sketch of the IWT7.5-164 hub

Table 2.8: Properties of the hub of the IWT7.5-164 reference turbine

Property	Value	Unit
Weight	40.70	tons
Hub radius	2	m

loads of the blade – the bolts would fail. As a compromise, the structural properties of the Sandia 100m blade (see [69]) were linearly scaled to a blade with 77m. Table 2.9 lists the main properties of this blade. The main material is glass-fiber reinforced plastic (GFRP), the bolt interface are T-Bolts with a diameter of 75 mm.

Table 2.9: Main blade characteristics

Property	Value	Unit
Weight	52	tons
Length	77	m
Root bolt circle diameter	4.50	m
Spar cap maximum width	1.57	m
Spar cap minimum width	0.50	m

The stiffener plate (see Figure 2.30) is located between blade and inner ring. FE simulations without a stiffener plate showed a radial ring deformation of 5.5 mm for the extreme bending moment of 50 MNm. These values are not acceptable and the stiffener plate reduces them to acceptable 0.6 mm. The stiffener plate is made from 1.0570 (S355J2G3) steel, has a thickness of 40 mm and a mass of 4.054 tons. The additional bolt circles are part of the design for the endurance run and connect to an optional hydraulic pitch cylinder.

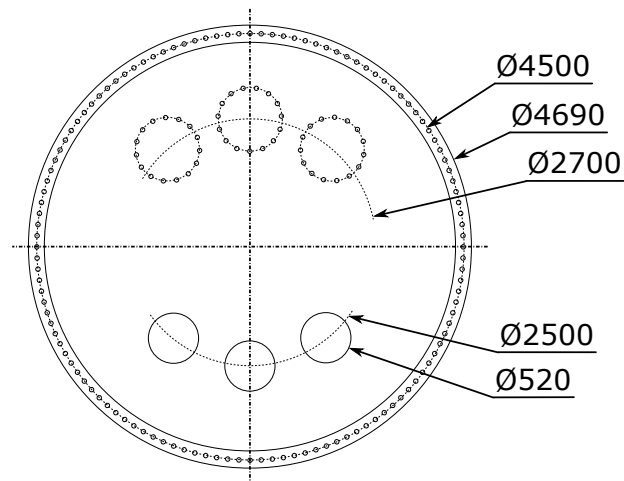


Figure 2.30: Stiffener plate of the IWT7.5-164

The pitch drive is a Bonfiglioli 712T3R gearbox with a Bonfiglioli BN160 motor. Due to space requirements, the first gear pair between motor and gearbox are bevel gears. The ratio of the gearbox is 1:104, the maximum output torque are 26.950 kNm and the dry weight of gearbox and motor are 760 kg. The gear backlash (play) between pitch drive and internal gears of the pitch bearing, which is necessary to limit friction and prevent jamming, is 0.02°. Figure 2.31 shows a sketch of the pitch drive.

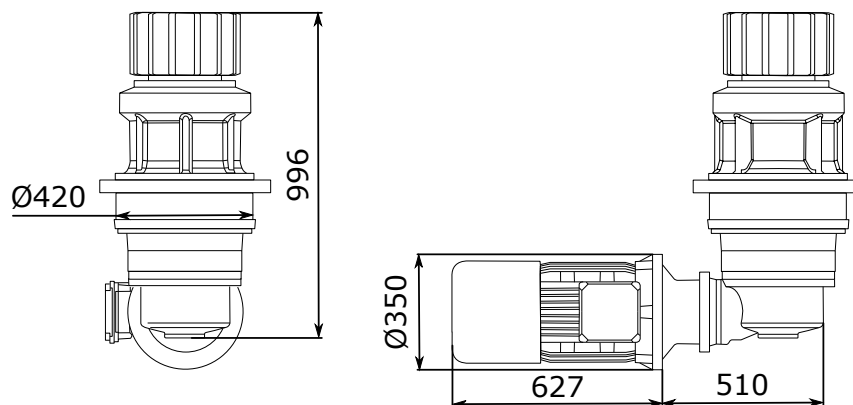


Figure 2.31: Pitch drive of the IWT7.5-164

The grease of the bearing is a fully formulated commercial grease. It was chosen for its widespread application in pitch bearings. The grease has a lithium thickener, solid lubricants and additives. The viscosity of the base oil is $50 \text{ mm}^2/\text{s}$ at 40°C and the NLGI (National Lubricating Grease Institute) consistency number is 2.

2.4 Damage Modes of Pitch Bearings

2.4.1 Overview

Pitch bearings have – as a result of their size, complex interfaces, and challenging operating conditions – abundant possibilities of failing. A set of damage origin, progression and final inoperability of the bearing is called damage mode in this work. Figure 2.32 shows locations of possible damage modes in a bearing cross section, Table 2.10 lists these. For the sake of visual clarity, the damage visualizations in Figure 2.32 are limited to example locations, yet the damages can occur at all similar locations. The term raceway here refers to the surface of the raceway and the hardened ring material below it, and ring refers to the non-hardened ring material at farther distance from the raceway surface. Cage can refer to both cages and individual spacers between rolling elements. Some of the damage modes might trigger others. As an example: A grease degradation can lead to raceway wear. In order to avoid them, it is however necessary to understand the reasons up to a point that allows the development of effective countermeasures. In case of grease degradation, a different grease formulation or a constant grease exchange also solves the subsequent wear problem. The later sections on fatigue and wear apply for raceways, rolling bodies and gears (though some calculation models differ), but for the sake of readability the detailed explanations are limited to raceways.

Table 2.10: Possible damage modes and locations in pitch bearings

Location	Raceway	Ring	Cage Seals	Bolts	Gears	Grease
Index in Figure 2.32	1	2	3.1 3.2	4	5	
Damage modes	Rolling Contact Fatigue Wear Static Overload Edge Wear	Core Crushing Structural Fatigue Corrosional Cracks	Wear	Fatigue Wear	Contact Fatigue Wear	Degradation

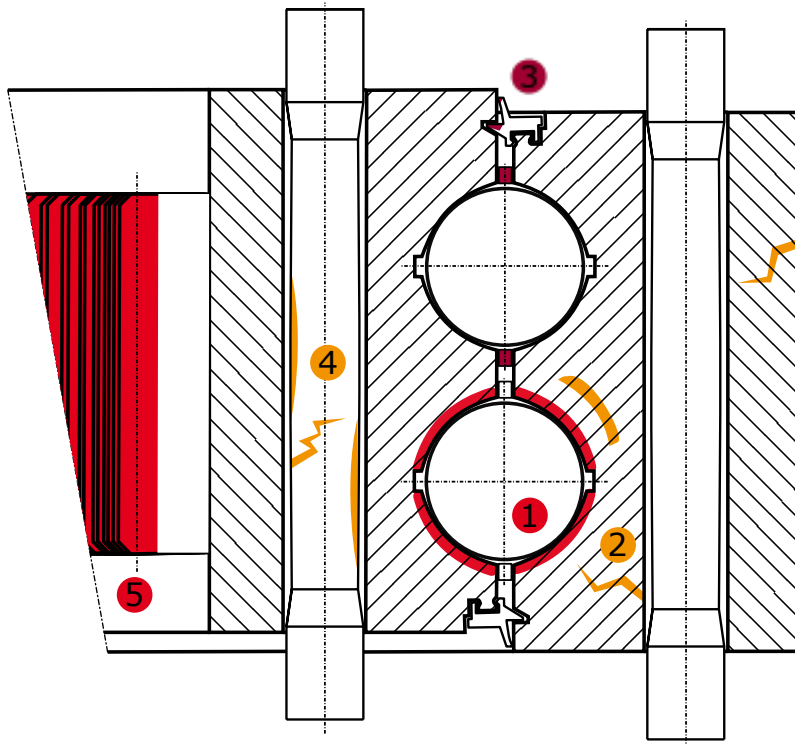


Figure 2.32: Location of damage modes

The exchange of pitch bearings comes at a significant price, since the blade has to be disconnected and lowered from hub height to the ground as well. Such exchanges are limited to situations in which the friction torque is too high for the pitch drive to turn the bearing or there is an imminent risk of the blade falling down. In both situations, damage has reached a severe state in the bearing, and it is challenging to determine its root cause. A crack going through the ring might have its origin on the raceway, the bolt holes or any other location. A completely destroyed raceway may have, in theory, reached this state with initial rolling contact fatigue, wear, or grease degradation. To the knowledge of the author, there are no meaningful data on pitch bearing failures and root causes available to the public. In one of the major studies on wind turbine reliability [70], the authors distinguished between *pitch bearings* and *blade bearings*, with one being seen as part of the drive train and the other as part of the rotor. This makes it hard to derive failure rates.

2.4.2 Fatigue of Rolling Contacts

In [43], Stammler and Schwack summarized rolling contact fatigue in pitch bearings. The following explanation stems from this work, except for the historical references. A properly mounted, lubricated and operated bearing can run for a very long time. In an ideal case, load and speed are constant and below limits for immediate failure, the bearing is oil-lubricated and the lubricant

forms a film that separates rolling body and raceway. Under such conditions, bearings fail (after the aforementioned very long time) due to rolling contact fatigue. Impurities in the bearing ring steel, for example inclusions of other materials, cause tension peaks on local levels and form the origin of micro cracks. Typically, these cracks start slightly below the surface of the bearing rings, as the shear stress is the highest at this point. The cracks grow up to the surface of the raceways and form little craters (pittings). When rolling bodies roll over these craters, the contact suffers from higher stress levels and the deterioration accelerates. Rolling contact fatigue (RCF) is usually discovered by a raise of the friction torque of the bearing at the appearance of the first pittings on the surface. [46]

RCF was a very prominent damage mode at the beginning of the 20th century, when steel impurities were much more common than nowadays. As impurities are statistically distributed along a population of bearings, so is rolling contact fatigue – every calculation results in a probability of failure, or, in the standardized way, in the time L_x that it takes for a certain percentage x of bearings to fail. [71]

The methods for RCF calculation were developed in the late 19th / early 20th century. Woehler showed how loads below static limits can damage material over time and coined the expression fatigue for this phenomenon [72]. The most common way to express this are the S/N slopes introduced in the section about load simulation. Hertz calculated pressure and stress distributions of spherical contacts [48, 49] (see Section 2.2.2 on Hertzian calculation for an example). Thomas and Hoersch used Hertz' results and determined the stress distribution under the surface [73]. Stribeck devised the friction curve that goes by his name today [74] and with it the idea of a full separation between contact partners. Miner introduced the concept of cumulative damage [75]. Weibull formulated statistical functions for multi-purpose applications [76]. These functions are used to express wind speed distribution as well. Lundberg and Palmgren ran fatigue tests on large populations of rolling bearings and defined the first model to calculate bearing fatigue life [77, 78].

As steel quality improved significantly over the 20th century, standard committees introduced correction factors to this model [79]. The introduction of models for elasto-hydrodynamic lubrication by Dowson and Higginson allowed to calculate lubrication film thickness [54, 80, 81]. Ioannides and Harris introduced a major update to the initial models in 1985 [82], in particular they defined a fatigue limit and stated that below this load no RCF occurs. These findings were incorporated in the standards and are part of the ISO 281 today [71].

Commonly, the RCF calculations are for rotating bearings. L_{10} (Equation (2.12)) is the time a population of bearings can operate until 10% of the bearings have failed. It is expressed in million revolutions. To derive L_{10_h} , these need to be divided by the speed of the bearing. C is the dynamic load rating, at which 90% of the bearings survive 1 million revolutions, P is the equivalent load, and p an exponent that depends on the geometry of the rollers. p was empirically determined by Lundberg and Palmgren. It is 3 for ball bearings [71].

$$L_{10} = \left(\frac{C}{P} \right)^p \quad (2.12)$$

Schwack and Stammer compared different approaches [9, 46, 71, 83] for oscillating applications in [10]. The comparison of the three methods showed significant deviations between their results. Additionally, most approaches are not applicable for short oscillations, which constitute a large portion of all pitch bearing movements (more on this in the later section on data analysis). Therefore it seems reasonable to develop the underlying methods, which have proven to be reliable for numerous applications, into a reliable model for pitch bearings.

Figure 2.33 shows a fatigue damage (pitting) on the raceway of a four-point contact bearing. This damage resulted from a test run that was specifically designed to provoke RCF. To the knowledge of the author, pure rolling contact fatigue has not occurred in any operating pitch bearing. However, the uncertainty about damage modes (see above) does not permit to classify this damage mode as generally irrelevant.

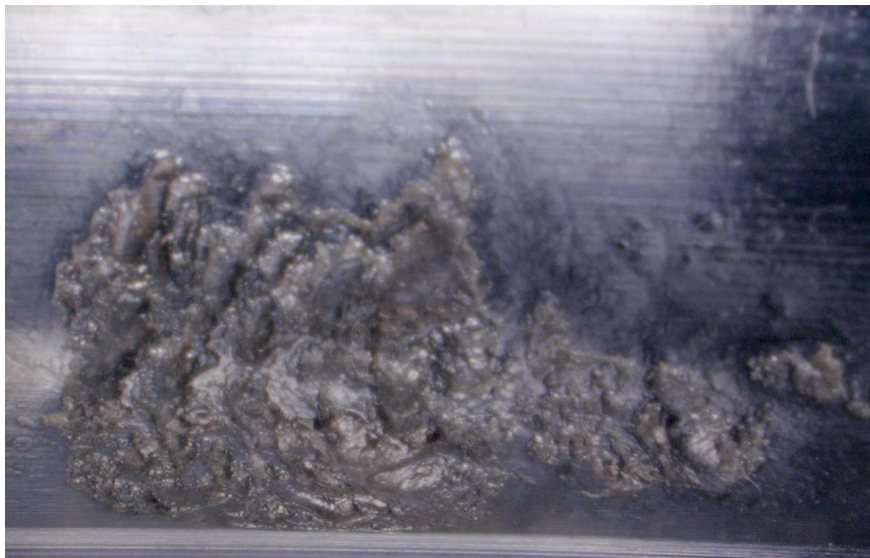


Figure 2.33: Pitting on the raceway of a four-point contact bearing after RCF test

2.4.3 Wear of Raceways, Rollers and Gears

If two perfectly smooth blocks of perfectly pure iron were placed against each other, they would become one block while their atoms form new links to each other. Bearing steels are less sociable metals than pure iron, yet they love to get acquainted with their rolling partners. Such acquaintance includes the exchange of atoms and molecules from one body to the other. This process is called adhesion. If one of the bodies is not perfectly smooth, if it even has sharp edges, and moves under pressure against the other, particles are removed from one or the two of them in a mechanical process, which is called abrasion. [84] Adhesion and abrasion are the two main wear processes in rolling bearings.

When a lubricant separates the rolling bodies (see above), wear is highly unlikely to occur. If no lubricant separates the contact partners, wear will occur at some point, unless additives in the lubricant form tribolayers that make the surfaces less reactive. Phosphor and sulfur are known to form layers on bearing ring surfaces which protect against wear. Foehl and Kußmaul described the formation of tribolayers with components of EP-additives in rolling bearings in [85]. They identified temperature and time as key parameters for a successful tribolayer formation. In a subsequent work (see [86]), they showed that it is necessary to apply pressure to the rolling contacts to create effective tribolayers. Attempts to create the layers by keeping the individual bearing rings in a heated oil bath failed. They also showed that high-alloy steels like X40Cr13H do not form tribolayers with organic additives, but need metal-organic additives. Thiede and Deters confirmed the necessity of pressure for tribolayer formation in [87]. Inacker, Beckmann, and Oster confirmed these findings in [58]. They also found that additives with longer molecular chains form thinner, but more stable tribolayers on the surfaces. At the surface of a raceway or roller with a tribolayer, the content of iron is very low. They defined the thickness of a tribolayer as the depth at which the iron content reaches 50%. In [59], the same authors focused on tribolayer formation on gears and came to similar conclusions as in rolling bearings.

In [43], Stammer and Schwack summarized wear damage modes in pitch bearings. The following explanation stems from this work. In some oscillating conditions, especially with small amplitudes, there is no separating lubricant film, and the lubricant cannot form tribolayers. Such conditions are type 1 of the pitch bearing movements shown in Figure 2.20. The most common wear phenomena related to such conditions are false brinelling and fretting corrosion.

Schwack stated that the first public report of false brinelling was given by Almen in 1937 [88]. Almen described damages on car hub bearings after ship transport. The bearings were ostensibly standing still during the transport, but the vibration of the ship engine and the ocean waves cause micro-movements ($x/2b < 1$) in the bearings. Such micro-movements can be very small rotations of the rolling bodies, but also changes in the contact ellipse size due to load changes on very low levels. These and the absence of a separating lubricant film lead to adhesive wear. Later operation of the bearings showed a strongly reduced lifetime. This problem was solved by using pre-tensioned bearings (the pre-tension reduced the micro-movements in standstill, this approach was later confirmed for large wind turbines bearings by Chen et al. in [89]) and adding EP additives to the lubricants. In the following decades, there were only few and disconnected publications on false brinelling [90, 91]. With the beginning of the 21st century, research activity increased [87, 92–98]. Most of the works focused on understanding influencing parameters like load, speed, frequency and lubricant. The author summarized the operating conditions of the tests in these works in [7] and compared them to wind turbine operating conditions. At the current state of knowledge, false brinelling will occur in grease-lubricated bearings that execute oscillating movements with ($x/2b < 1$) at or above a certain load level. If the oscillation parameters, amplitude and speed, are constant, there is no possibility to avoid false brinelling. Schwack [43] and Errichello [99] described the reaction product as magnetite.

In contrast, the reaction product of fretting corrosion is reddish hematite [43, 99]. Fretting corrosion is a more aggressive wear mechanism which develops from initial adhesive into abrasive wear. Hematite as a reaction product can indicate two things: Either there is no lubricant in

or around the contact and the relative movement between the contact partners happens under dry conditions, or water is in or around of the contact. False brinelling can develop into fretting corrosion, especially for amplitudes of ($x/2b > 1$). It was shown to occur up to ($x/2b = 12$) [43]. To the knowledge of the author, there are no reliable analytical models to calculate occurrence and progression of any wear damage mode.

Figure 2.34 is a microscopic picture of a pitch bearing raceway with multiple damages on the left side and a color map on the right side. The horizontally oriented grooves are a result from the hard turning, which was the final manufacturing step of this bearing. The green area is undamaged raceway, the orange area a false brinelling damage and the red area abrasive wear. In this case, the abrasive wear formed valleys in the raceway. The pitch drive was not able to supply enough torque to move the balls out of these valleys, and the bearing was exchanged. The false brinelling subsequently appeared on the abrasively damaged area because the bearing was in standstill between damage report and exchange.



Figure 2.34: Pitch bearing raceway with wear damage modes

The author assumes that raceway wear is a prominent damage mode of pitch bearings, but only in some cases to an extent that prevents pitch movements. There is no way to change the bearing design in a way that it is completely resistant to wear. The pitch controller, however, can counteract wear on raceways: Longer movements, which could either build up lubricant films and/or tribolayers, were described in patents [100,101] and guidelines [9,102]. In this work, the author could confirm the validity of the concept (more on this in the later Section about scaled tests).

2.4.4 Static Overload and Edge Wear

A static overload is a rolling element load Q that leads to an indentation of the raceway beyond permissible values. A consequence of static overload is edge wear: Section 2.3.1 about pitch bearing types explained the concept of free contact angles in four-point bearings. If the contact angle is very high, the pressure ellipse of the contact is truncated (see Figure 2.35), and the pressure can exceed permissible static values. In such cases, large debris brakes out of the raceway

edge. In both cases, static overload and edge wear, continued overrolling of the damaged areas lets them grow, and at a certain point the pitch drive cannot turn the pitch bearing anymore due to increased torque. Both damage modes can be prevented in the design stage. The standard ISO 76 [103] gives guidance on avoiding static overload, and finite element (FE)-simulations allow to understand the contact angles in given load situations (more on this in the later section on FE).

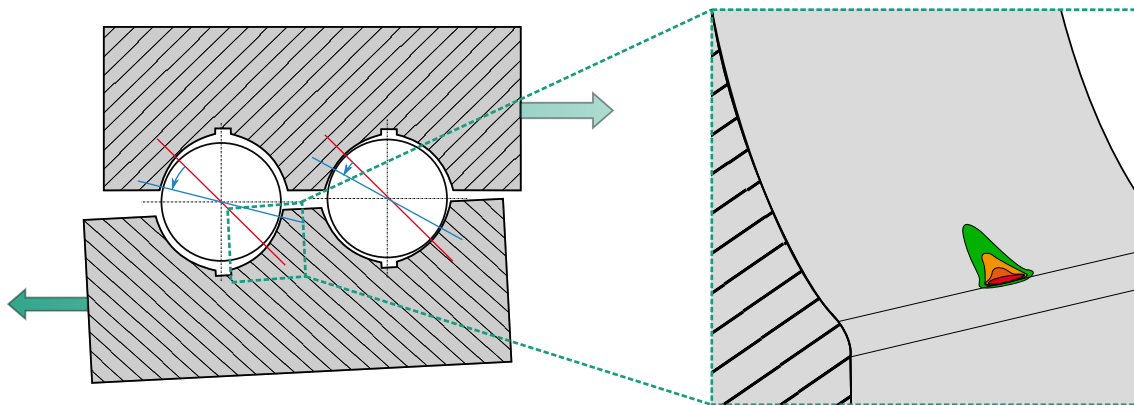


Figure 2.35: Truncation of a contact ellipse at high contact angles

2.4.5 Other Damage Modes

In comparison to wear and fatigue phenomena, little or no research about other damage modes is known to the author. The following description bases on practical experience and gray literature.

Of the possible damage modes, anything related to corrosion is probable and critical for a pitch bearing. As it operates outside, sometimes covered by a plastic part called spinner, sometimes without any extra cover, protection against corrosion is important. In particular it is important to prevent the inner surfaces of the bolt holes from corroding. Depending on other elements of the bearing like fill plugs and grease lines they can be in structurally weaker regions and consequentially suffer high deformations. If they corrode, the combination of deformations and corroded material can initiate cracks. These grow into the ring material and can lead to ring fractures. Surface coating can provide suitable protection against corrosion, but it is not trivial to apply it inside the bolt holes.

A form of RCF limited to slewing bearings is called core crushing [104]. The raceways are hardened in the manufacturing process, and the hard layer reaches into the ring material. The unhardened ring material can only cope with much smaller loads than the hardened material. Depending in the hardening depth and the loads, it can be possible to exceed permissible values in the unhardened material and initiate fatigue failures at a much higher depth than in common RCF cases.

Varying loads in various degrees of freedom act on bearing rings and bearing bolts. Both of them can suffer from structural fatigue failures. For bolts, the VDI guideline 2230 [105] serves as a calculation standard to calculate fatigue resistance.

In common pitch bearings, lubrication systems continually re-supply grease. Grease flow inside the bearings is somewhat unpredictable, and it is never certain that the rolling contacts are re-supplied. In the worst case, fresh grease finds its way to the outlets without getting into the contacts. Under such circumstances, the grease in the contact is subject to mechanical wear, degradation and aging, all of which will lead to an inability to fulfill its purpose. As a high number of pitch bearings survive turbine lifetimes, it is however reasonable to assume that most lubrication systems work well.

2.5 Design of Pitch Bearings

2.5.1 FE Simulation of Pitch Bearings

The individual rolling elements in a pitch bearing are not necessarily subject to identical loads. On the contrary, the load distribution between the elements is rather complex and defined by outer load distribution and interface stiffnesses (see Section 2.3 on pitch bearings). Any design process for a pitch bearing needs to take account of the load distribution.

Guidelines [9] provide approximate load estimation functions, but Menck and Stammer showed in a comparison with finite element simulations that these are inaccurate for pitch bearings [106]. Aguirrebeitia et al. took several steps towards an analytical solution that could replace such approximate functions. At the current stage, these solutions are still limited to single-row bearings and are not able to take into account inhomogeneous stiffness distributions. [107–110]. As no analytical solution is available, finite element (FE) simulations are the only means to calculate the load distribution of a pitch bearing.

Finite element simulations are a widespread analysis technique in engineering. A complex geometry is split into small, simple elements like pyramids or cubes (called a mesh). FE software packages supply a variety of elements in 1D, 2D and 3D. 1D elements are called beams, 2D shells and 3D solids. It is possible to calculate such elements with analytical equations. The elements are connected to each other at one or more nodes. An iterative solver algorithm calculates stresses and deformations in all elements. These values are influenced by the values of the other elements, as such the solution process has to be iterative. The element size is a compromise between accuracy and computational effort. [111]

Pitch bearings, particularly four-point contact bearings bring along a series of aspects that make a comprehensive simulation a wonderful challenge:

- A very high number of rolling contacts with pre-tension
- A very high number of bolted connections with high pre-tension

- Rotationally non-symmetrical load distribution at the rotor of the turbine
- Hub and blade with inhomogeneous stiffnesses
- Changes of ball contact angles under load

The size of the the contact area of a rolling contact (compare Section 2.2.2 on Hertzian calculation for some exemplary numbers) is relatively small in comparison to the dimensions of the roller and the raceway (or even a complete bearing ring). The type 12480 pitch bearing has 147 rolling bodies per row and 2 rows. Each rolling body has 4 possible contacts, which results in 1176 contacts with a size of some mm², in comparison to bearing rings with a diameter of 5 m and 30 cm of height. If all contacts were modeled with flexible 3D elements and a reasonable resolution, a global model of the bearing would take prohibitive high time to solve. If the contacts were modeled with a coarse resolution, they would not provide accurate results for contact pressure and size. A possible solution to this dilemma is to split the models: To split the model into a local model of an individual rolling contact to determine contact parameters and stiffness and a global model that uses the former to calculate global load distributions in the bearing. The fine model can, depending on the desired level of accuracy, be replaced by the Hertzian calculation of Section 2.2.2. In the global model, the contact stiffness curve (see Section 2.2.2) is taken as the non-linear stiffness of a spring that represents the contact properties. The springs are connected with stiff beam elements to stiff shell elements that connect to the flexible ring elements. Figure 2.36 shows such an arrangement, with the stiff elements in orange, and the nonlinear springs in blue. For the sake of visual clarity one of the spring-beam-connections has faded colors. The upper part visualizes the input of a force-deformation curve with a smaller version of Figure 2.10.

This approach is commonly called Daidié-approach, after the work of Daidié [112]. Gao et al. [113] used a similar model and confirmed the validity. Wang et al. and Baust and Stammeler applied it to three-row roller bearings [6, 114]. Four-point contact bearings can change the contact angles with outer loads (see Section 2.3.1). Truncation of the contact patch shall be limited under operational conditions (see Section 2.4.4). In the work of Daidié, the contact angle variation is determined by reading the deformed positions of the end points of the nonlinear springs. This approach is valid unless the bearing rings itself move in the simulation, e.g. because the hub flange it connects to deforms. Figures 2.37 and 2.38 attempt to visualize this problem.

Figure 2.37 shows a simulation with a fixed outer ring hub flange (fixed boundary condition marked in blue) and without tilting of the inner ring. The initial positions of the spring ends are 1 and 2, and the deformed positions are 1' and 2'. Their respective coordinates in x and y allow to calculate the contact angle:

$$\beta = \text{atan} \left(\frac{y_{2'} - y_{1'}}{x_{2'} - x_{1'}} \right) - 45^\circ \quad (2.13)$$

The coordinate system of Figure 2.37 has to be defined in the undeformed condition of the model. In a case without any tilting of the ring section, this does not pose a problem. However, Figure 2.38 shows a simulation where the bearing connects to a hub and the inner ring is allowed to tilt. Using the same equation as before, the result overestimates the contact angle in this case. The

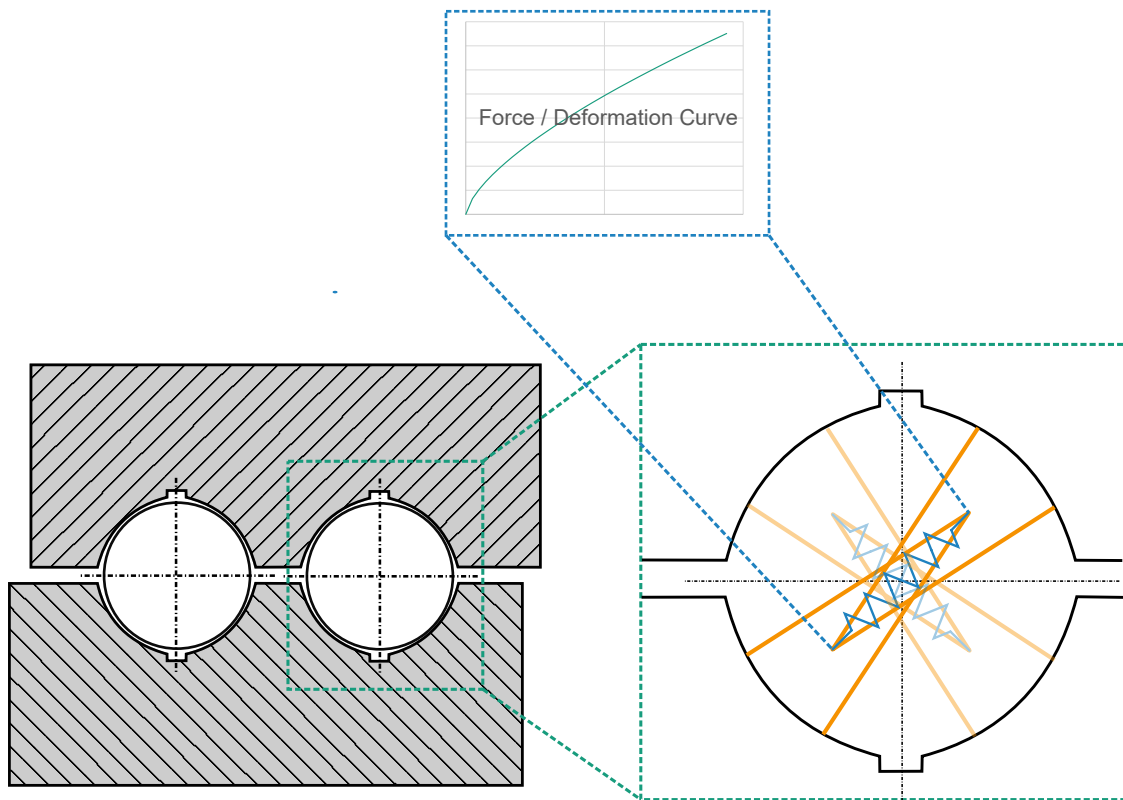


Figure 2.36: Springs representing a ball in a four-point contact FE model

errors are in the range of 2° for the type 12480 bearing in the IWT rotor. For load cases with high contact angles and a risk of truncation, these errors are not acceptable.

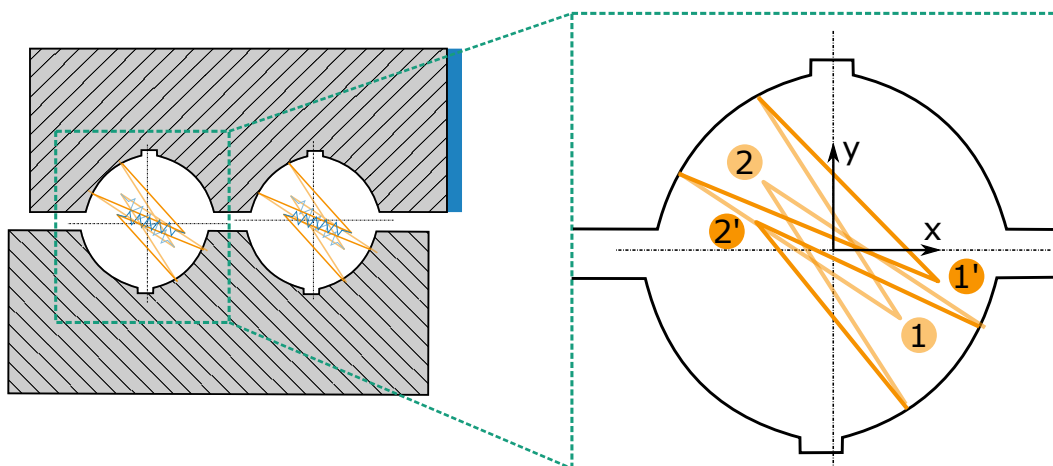


Figure 2.37: Contact angle calculation in a bearing with fixed hub flange

A possible solution to this problem is to evaluate the projection of the axis of the nonlinear spring onto the raceways and define the contact angle as a function of the contact point. The implementation of this into FE code would be very tedious and has, according to the knowledge of the author, not yet been done in published work.

Pitch bearings connect with bolts to the interface parts (hub and blade). The bolts are pre-tensioned and contribute to the pre-tension of the rolling contacts and to the stiffness of the rings. In [6], Baust and the author modeled the bolts as beam elements. Pre-tension can be modeled by various means. Some FE codes provide pre-tension for the elements, in other cases the initial temperature of the bolts is set to a value so that they reach target pre-tension at the simulation temperature (this can help with convergence issues).

The blade is usually modeled with shell elements except for the root section. Inlays or T-Bolts are usually modeled in 3D [66, 115, 116]. The hub is fully modelled with 3D elements. Common approaches to simulate a blade bearing with its interface are one-sixth, one-third and full rotor star models (see Figure 2.39).

One-sixth and one-third models have symmetrical boundary conditions at the cut surfaces (marked in pink in the figure) and reduce computational time significantly. However, they cannot be used to calculate realistic load cases of a rotor star. In case of a one-sixth model it is obvious that the blade behavior is neglected. In case of a one-third model, the forces at all blade roots have to be the same. Table 2.11 lists the extreme bending moments of the IWT7.5-164 turbine with the Enercon controller for one blade root (labeled blade 1) and the load the other blade roots have at the same time.

It is clear that the three blades do not have the same loads at the same time. In particular, it is physically impossible to have the same M_x , as this would mean the blades are in the same position (M_x is dominated by gravitational forces). As such, any symmetric calculation necessarily gives an unrealistic result and it is necessary to model full rotor stars.

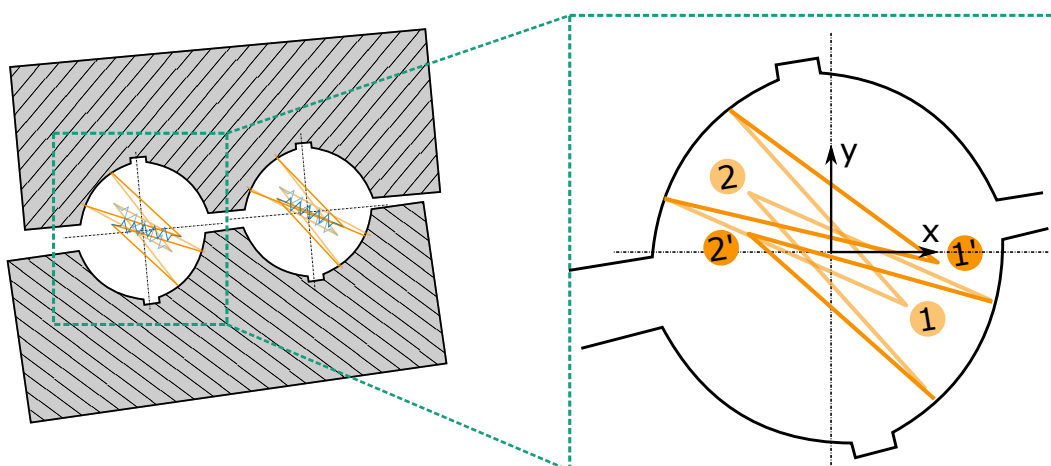


Figure 2.38: Contact angle calculation in a bearing with flexible hub flange

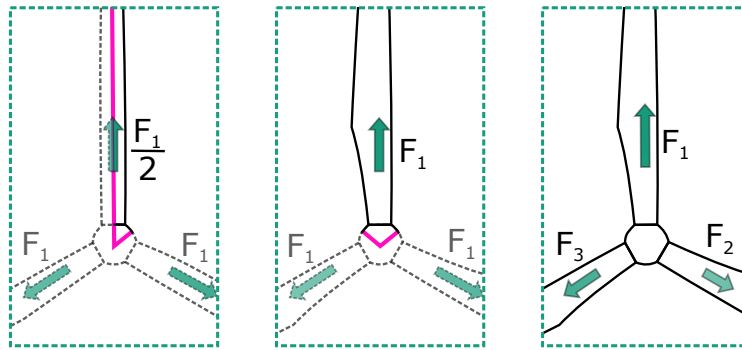


Figure 2.39: One-sixth (left), one-third (center), and full rotor star (right) models

Table 2.11: Extreme loads of blade root 1 and other root loads at the same time (in MNm)

Signal Load case	M_{x_1}	M_{y_1}	M_{x_2}	M_{y_2}	M_{x_3}	M_{y_3}
DLC6.2	26189	-5042	-12113	-1220	-13864	165
DLC2.2	8746	28628	-83	21762	-2641	25728
DLC6.2	-19155	1050	7568	-4089	11510	2
DLC2.2	2658	-13983	3847	-8650	-1008	1194

Figure 2.40 concludes this section with an example output a simulation of the IWT7.5-164 pitch bearing in the BEAT6.1 test rig. The different curves are the loads of the four raceways (two rows of balls, each of which has two raceways on each ring). The bearing is subject to a bending moment of 35 MNm. Due to the typical distribution of axial loads (see earlier Figure 2.19), the four-point contact turns into a two-point contact and each raceway carries loads over a span of approximately 180°. The expression ‘Traction Side’ refers to the 180° span of the bearing where the axial loads point in positive z-direction or away from the hub. In this section, the inner ring is pulled towards the outward direction.

The highest ball load is 188.4 kN which equals a contact pressure of 3.176 GPa. Figure 2.25 in Section 2.3.3 depicts the difference of a load distribution for an ideally stiff tube and a rotor blade, both subject to a bending moment. If a bending moment of 35 MNm is applied to the bearing by ideally stiff interfaces, the highest ball load would be 143.59 kN or 76.2 percent of the load at the test rig.

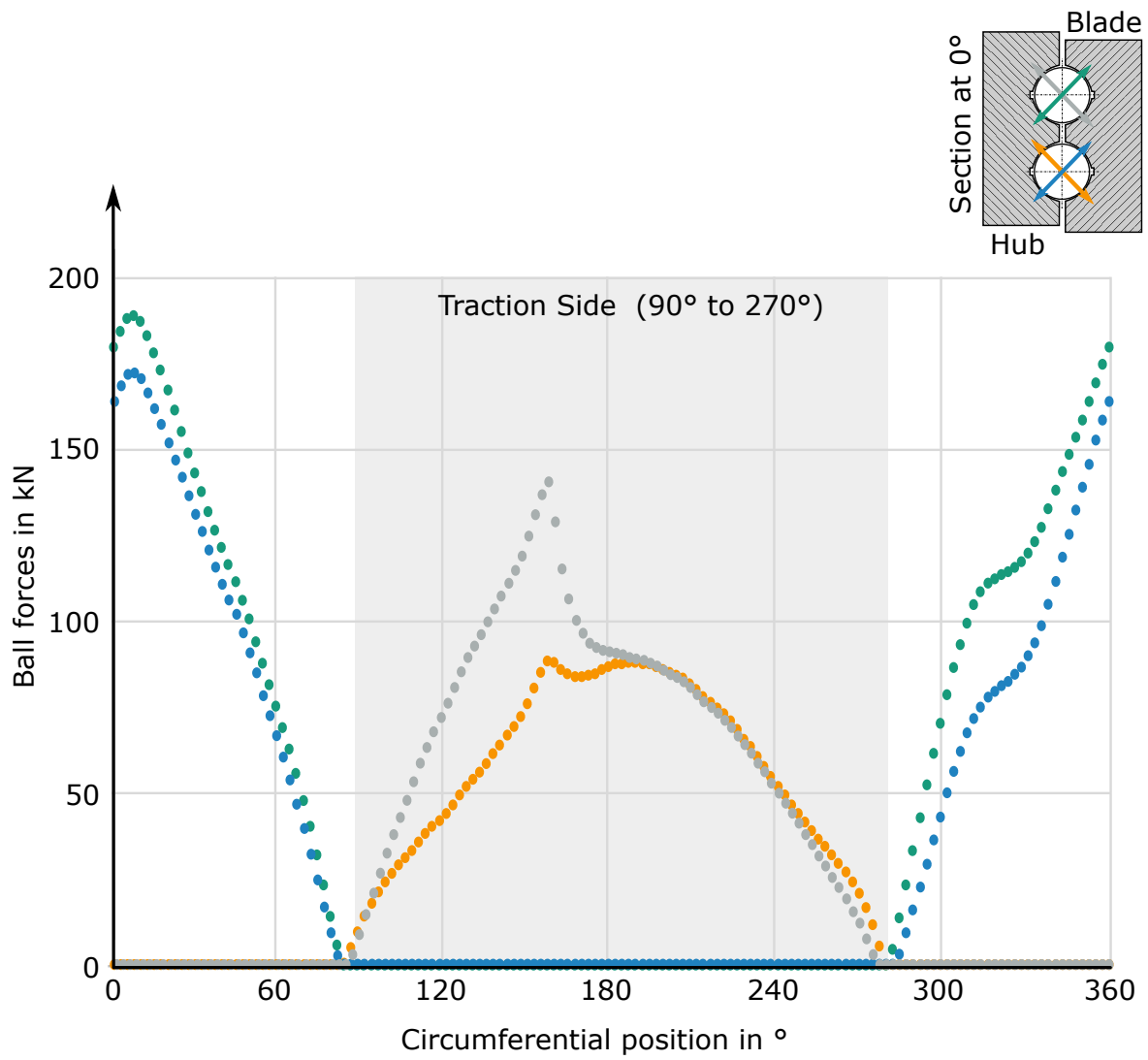


Figure 2.40: Example load distribution of the IWT pitch bearing

2.5.2 Prevention of Damage Modes

With the results of properly executed FE simulations and with rainflow counts and DELs derived from the aero-elastic simulation, it is possible to design pitch bearings against a number of failure modes before the first prototype is produced. Table 2.12 repeats the earlier Table 2.10 on damage modes, but all preventable damage modes are in green font. Wear damage of the bolts can be prevented, because it would be caused by a contact to the bolt holes (and relative movement), which can be avoided through careful design and FE analysis. The author deems rolling contact fatigue as one of the damage modes that can be solved prior prototype production. However, the methods require further development (see the earlier section on damage modes).

Table 2.12: Preventable damage modes

Location	Raceway	Ring	Cage Seals	Bolts	Gears	Grease
Damage modes	Rolling Contact Fatigue	Core Crushing	Wear	Fatigue	Contact Fatigue	Degradation
	Wear	Structural Fatigue		Wear	Wear	
	Static Overload	Corrosional Cracks				
	Edge Wear					

This leaves corrosional cracks, wear damage modes and grease degradation as the damage modes that cannot be excluded before the pitch bearing becomes reality. Protection of surfaces against corrosion is a challenge shared with many other applications, and standards for development, layer thickness and test methods are available. [117] It is not necessary to use a complete pitch bearing for such tests. Wear modes and the behavior of grease in the complex pitch bearing, however, call for tests with a complete pitch bearing. As wear modes are influenced by load (and load distribution) and slip (which in turn is influenced by the ring deformation, contact angle, and load distribution), a realistic test also needs realistic load conditions and interfaces.

2.6 Test Rigs for Pitch Bearings

In the sections on damage modes and pitch bearing design, we learned that it is not possible to exclude all damage modes before the first prototype of a pitch bearing is manufactured. The author concluded that a test should represent the outer loads of the pitch bearings and its interfaces. Test rigs for pitch bearings have been built by turbine manufacturers, bearing manufacturers and research institutions. Figure 2.41 shows the concepts of these rigs, of which there are three:

1. Upright bearing, steel interfaces, static/dynamic load application
2. Horizontal bearing, steel interfaces, dynamic load application
3. Upright bearing, hub and blade interface, static load application

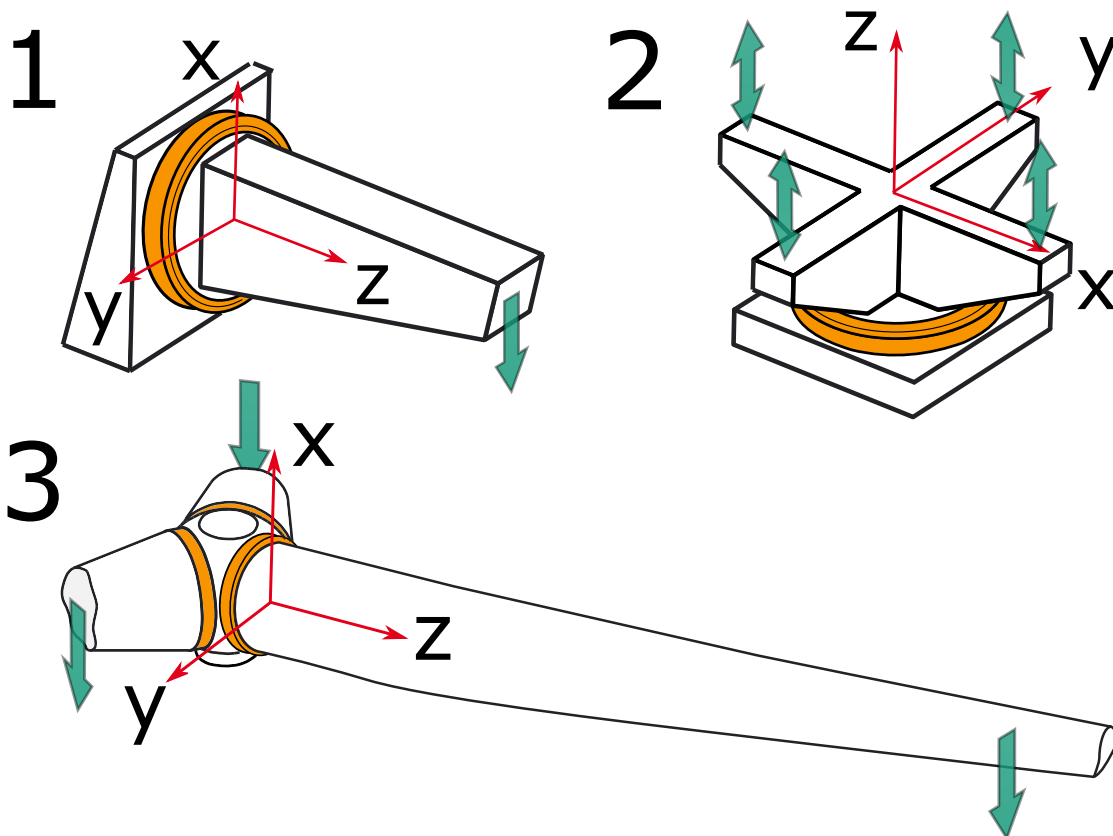


Figure 2.41: Concepts of blade bearing test rigs

Concept 1, with steel interfaces and an upright bearing, can be found with bearing manufacturers, among them Liebherr [118], Rothe Erde [119], Shanghai Oujikete [15] and Rollix [120]. A similar concept is followed by the WindBox consortium near Bilbao, Spain.



Figure 2.42: Fraunhofer IWES initial pitch bearing test rig for Senvion
©: Fraunhofer IWES / Martina Buchholz

Concept 2 can be found at the Korean Institute KIMM [121] and the Chinese manufacturer Fangyuan [122].

Wind turbine manufacturers, who have access to hubs and blades, typically use concept 3 with realistic interfaces. Publicly known test rigs are operated by Vestas [123], Siemens (most Siemens test rigs are outdoor and visible from nearby public roads) and Nordex (a picture of the test rig is part of one annual commercial report, see [124]). The author headed a project for the design and operation of an initial test rig for Senvion (see Figure 2.42 and [125]).

None of the above listed rigs is able to apply dynamic loads while having realistic interface structures. To the knowledge of the author, such a rig does not exist outside of the project covered by this thesis.

2.7 Chapter Summary

Wind turbine pitch bearings are rolling bearings that connect the rotor blade and the rotor hub. Their design incorporates aspects from wind energy and tribology. This chapter attempted to give an overview of these different fields.

The chapter began with a general look at wind turbines. The dominant concept is introduced, a three-bladed, upwind, horizontal-axis turbine. Almost every commercially available turbine follows it. Aero-elastic models are used to calculate the loads of turbine components from assumed wind fields. Pitch control in general and Individual Pitch Control in particular allow power and load control of the turbines. Individual Pitch Control is well established except for a lack of knowledge about its influence on pitch bearings. The IWT7.5-164 reference turbine is introduced. This turbine serves as an example for the later development of an endurance run for pitch bearings.

The section about rolling bearings began with general remarks on this mechanical component. Rolling bearings are two rings with rolling bodies in between. They allow rotation about one axis, while in general locking any other degree of freedom. In comparison to sliding bearings, they have a lower friction but higher contact stresses. The contact area between balls and raceways has an ellipsoidal shape, and the contact parameters can be calculated according to Hertz. The contact of the IWT7.5-165 reference turbine pitch bearing has a maximum pressure of 2 GPa, a width of 2.67 mm, and a height of 16.8 mm at 47025 N applied force. The rolling bodies move with approximately half the speed of the rotating ring. The ratio $x/2b$ is valuable to compare movements of bearings with different diameters. Grease is the lubricant used in pitch bearings, as it has the economic advantage over oil lubrication. The way grease acts to lubricate the contacts is not fully understood, and the additives play an important role in the formation of tribolayers on the surfaces.

The most common type of pitch bearings are four-point contact ball bearings. The dominant blade loads, M_y and M_x convert into a distribution of axial forces at the root. The load distribution differs from an ideally stiff tube due to the structural layout of rotor blades. Four-point bearings translate the axial forces into combinations of radial and axial forces and consequently have a tendency to ovalize under load. There are four important categories of pitch bearing movements. Category 1 is a oscillation with nearly constant amplitudes and mean values, category 2 is a similar oscillation, but interrupted by larger movements, category three is a sum of larger and smaller oscillations, and category 4 are periods without pitch angle changes.

The blade, made mostly of fiber-reinforced plastics, introduces the loads into the pitch bearing. Besides the aforementioned axial load distribution, the bolt interfaces and the ovalization of the blade influence the loads of the pitch bearing. The rotor hub, made of casted steel, has an inhomogeneous stiffness distribution along the circumference of the blade bearing flange due to its complex geometry and the interface with the main shaft of the drive train. Additional stiffener elements like plates or rings are part of some designs that limit pitch bearing deformations. The IWT7.5-164 pitch bearing, built by IMO, is a four-point contact ball bearing with two rows and an outer diameter of 5 m.

Pitch bearings can fail for various reasons, among them fatigue, wear, static overloads, corrosion and lubricant degradation. Fatigue damage modes are reasonably well understood, yet the complex load distribution and oscillatory movements of pitch bearings lead to different results with different approaches. Corrosion cannot be calculated (there is no model to predict when corrosion turns into a crack that endangers the ring), but there are standardized methods and tests for surface coatings. Wear, especially of the raceways, has received increased attention of the scientific community in the last two decades, but it is not yet possible to calculate occurrence or progression of this damage mode. Failure connected to grease degradation cannot be calculated either. These last two need tests of a whole pitch bearing, preferably with realistic interface conditions.

Finite element simulations are a crucial step in the design of pitch bearings. Currently, there are no analytical methods to calculate the load distribution in a blade bearing (with interfaces). FE simulations need to simplify some aspects of the bearing, in particular the rolling contacts, to limit computational time. A common approach is to use non-linear springs to represent the stiffness of a rolling contact. Calculating the real contact angle of a ball from a simulation of a full rotor star is a challenge not yet solved. The correct transfer of loads from aero-elastic simulations to FE is not yet state of the art, and the author proposed a method to overcome this shortcoming.

Wind turbine manufacturers, bearing manufacturers and research institutions in Europe and Asia have test rigs for pitch bearings. Turbine manufactures typically use real interfaces (hub and blade), while bearing manufacturers and research institutions rely on steel interfaces (supposedly due to the lack of access to real blades). The author was responsible for the construction and operation of a 3-MW class blade bearing test rig developed together with the manufacturer Senvion.

Wear damage modes of pitch bearings call for tests with realistic loads and interfaces. None of the so far described test rigs is able to run such a test. Either they have realistic interfaces and only static load application, or they have dynamic load application but steel interfaces with unrealistic stiffness properties.

Chapter 3

Data Analysis

3.1 Range-pair Counting and Bin Counting

The design of a pitch bearing test program starts with the analysis of the output of aero-elastic load simulations. The author published an article on data analysis of pitch bearing movements in *Renewable Energy Focus* in 2018 [4]. The present section largely stems from this publication. For the sake of readability, the IWT7.5-164 reference turbine with Enercon controller is called IWT in the following.

The section on load simulation defined the common load simulation output as time series files that need post processing to turn provide meaningful data for the design of components. Common post-processing techniques include bin counting, rainflow-counting and DEL calculation. The output of rainflow counting can be in form of so-called Markov matrices.

Rainflow counting produces valuable data for any structural fatigue calculations, but for an analysis of pitch bearing movements it is not suitable. For both rolling contact fatigue calculation and estimation of wear probabilities, it is necessary to consider each turning point of the oscillatory movements as the end of a half cycle. Rainflow counting summarizes cycles to reflect on spanning movements, which are of less importance for wear. With regard to blade-bearing movements, it is more important to focus on the single distances x covered by the roller/ball on the raceway. Every interruption of a movement leads to a breakdown of possible lubricant films and has to be taken into account. As such, the less common range-pair counting approach is more suitable in this case. Figure 3.1 compares the two approaches. Rainflow counting overestimates the number and amplitude of long cycles (see 1 in Figure 3.1) and the number of cycles with relatively small amplitudes (see 3,5 and 7 in Figure 3.1).

The author implemented the range-pair counting method in a MATLAB program, which uses the raw time series data as input. The time series of the IWT have a sample rate of 200 Hertz. The algorithm calculates the first derivation of the pitch angle signal $\dot{\theta}(t)$. A change of the sign of this signal (e.g. positive to negative) is a turning point of the movement. The movement between two turning points is one half cycle of an oscillation. All half cycles are stored into an array (designated *cycleTstore*). Depending on a set of filters, the half cycles are stacked into bins or ignored if their range is too small or large.

Figure 3.2 shows the results of cycle countings for different configurations of the IWT for a period of 20 years. Any oscillation with a range smaller than 0.05° is not taken into account. Such oscillations can appear in load simulation time series, however, it is questionable if the turbine executes them in reality as well. The reasons for this are the gear backlash, the inertia of the mechanical components and the bearing friction. Both of them are usually not part of the simulations. The CPC and IPC controllers are IWES controllers (these results were presented in [4] as well), the EN IPC refers to the Enercon IPC controller (these results appear first in this thesis).

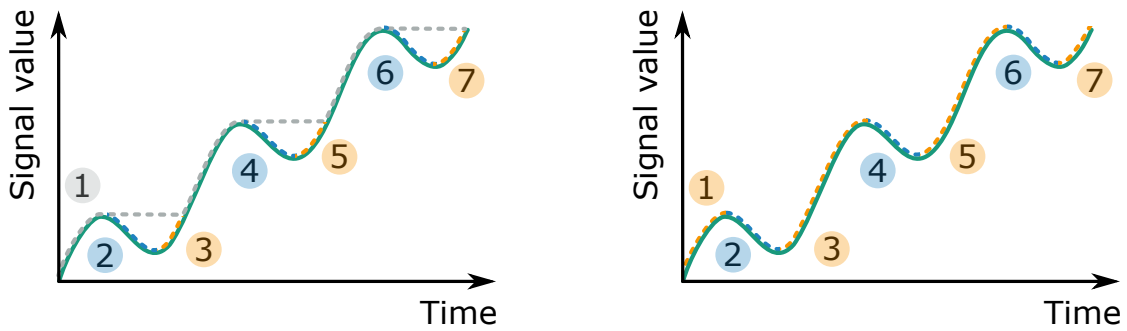


Figure 3.1: Rainflow counting (left) vs. range-pair counting (right)

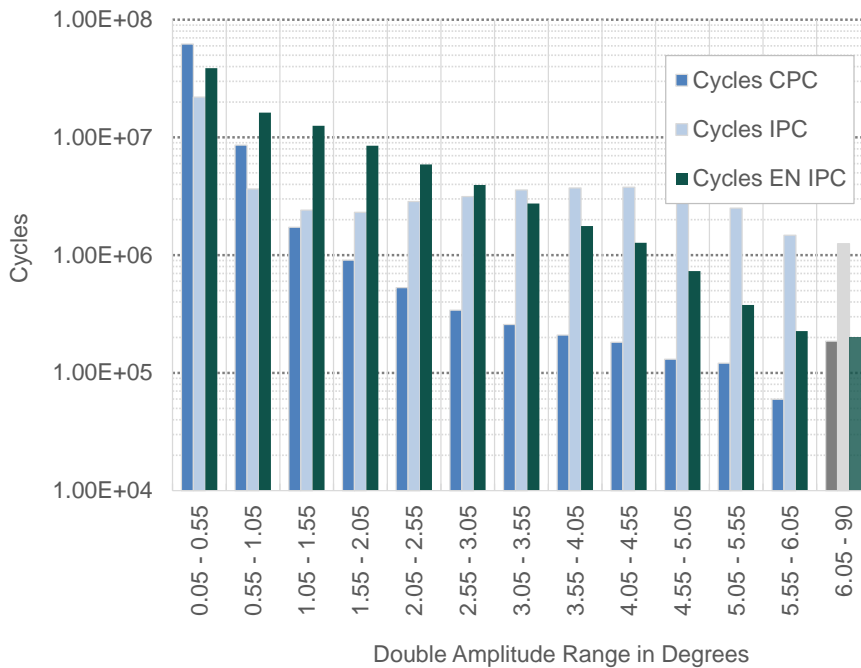


Figure 3.2: Results of cycle counting for the IWT with different controllers

The IWES IPC limits IPC activity to absolute pitch-angle values of 2.50° and higher (see [43] for further details on the controller), which corresponds to the turbine operating above rated speed. In comparison to the CPC, it has less cycles with a very small amplitude (below 1.05°) and more cycles with amplitudes from 1 to 6° . The CPC needs to control the generator power output close to and above rated speed and does this with very small movements. If the IPC is active, it executes larger movements to reduce the loads of the turbine, and by doing so, it also reduces the generator power output slightly, which makes the very small movements unnecessary. As a conclusion of [43], the author stated that the IPC reduces the risks for wear damage of the raceway. The Enercon controller (see the section on the IWT reference turbine) activates IPC also below rated speed, as the wind speeds slightly below rated contribute large time fractions to the turbine operation and fatigue loads. At these wind speeds, the IPC oscillations have smaller amplitudes. In comparison to the IWES IPC, the Enercon IPC executes more cycles, particularly with smaller amplitudes of below 2.05° .

The MATLAB program executes bin counting of other signals in addition to the cycle counting of pitch-angle signal. The visualization of these results allows to evaluate the controller behavior and do plausibility checks on the results. Figure 3.3 shows a stacked bin counting of resulting bending moments ($M_{res} = \sqrt{M_y^2 + M_x^2}$), grouped by cycle counting amplitude results. It compares the different controller variants.

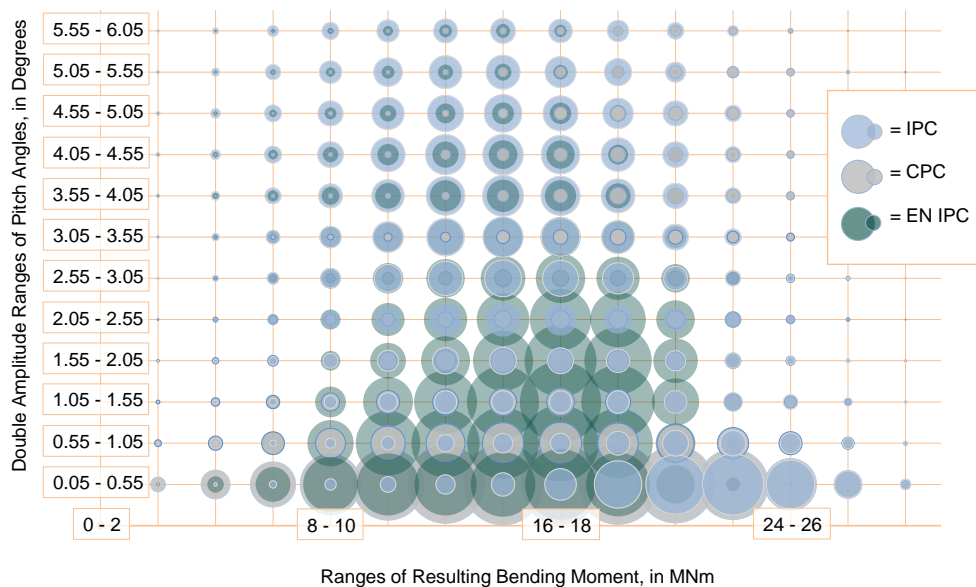


Figure 3.3: Oscillation amplitudes and resulting bending moments

Again, the CPC and IPC values are obtained for the IWES controller (published in [43]), the Enercon controller was added for this thesis. The size of a circle represents the time spent in a bin. For the sake of visual clarity, the order of the colors is changed throughout the figure so that the smallest circle is always on top. One bin is a range of double amplitudes and a range of

resulting bending moments. In the double-amplitude bin (range bin) of 0.05 to 0.55° combined with the bending-moment bin of 8 to 10 MNm, the IWES IPC spends the shortest time, and the CPC the longest. While pitching with double amplitudes between 0.05 and 0.55°, all controller variants spend most of the time in bending moment ranges between 8 and 26 MNm. It can be seen that the Enercon controller, in comparison to both other controllers, adds pitch activity for the ranges of 0.55 to 2.55° and 14 to 18 MNm. This behavior is as expected, as these loads occur for wind speeds below rated speed.

3.2 Movement Sequence Recognition

Section 2.3.2 on operating conditions of pitch bearings introduced four types of movement sequences. A movement sequence is a series of oscillations with certain properties (see Figure 2.20). Some types of sequences promote wear damage risk, others diminish it. The later section on scaled sequence tests gives results for different movement sequences. To design an endurance run program, it is necessary to understand the occurrence of different movement sequences in the time series. The MATLAB program uses the array of half cycles *cycleTstore* to identify movement sequences. Table 3.1 shows a shortened version of *cycleTstore* for one simulation file (power production for a mean wind speed of 6 m/s).

Table 3.1: CycleTstore example

Start line	End line	Double amp.	Bottom value	Mean value	Sequence length
-	-	o	o	o	-
182	252	1.117	0.035	0.594	0
252	331	1.088	0.064	0.608	0
331	395	0.619	0.064	0.374	8
395	486	0.700	-0.016	0.334	7
486	548	0.125	-0.016	0.046	6
548	631	0.125	-0.016	0.047	5
631	644	0	-0.016	-0.016	0
644	765	0.119	-0.016	0.044	4
765	809	0	0.103	0.103	0
809	875	0.205	0.103	0.206	3
875	946	0.326	-0.017	0.145	2
946	1022	0.311	-0.017	0.138	1

'Start line' and 'End line' refer to the line at the beginning and the end of the half cycle. 'Double amp' (double amplitude) is the range of the movement. The column 'Sequence length' lists the length of a movement sequence of type 1 with a certain set of tolerances. For this example, the tolerances are set to a maximum deviation of 0.1000° for the lower value and an allowable double-amplitude range of 0.05 to 1° . All tolerances refer to the first half cycle of a movement sequence. The filter also allows pauses of up to 2 s without interrupting a sequence. The MATLAB program cycles through all lines and calculates the length of the sequence that starts with each of them. For line 1 and 2, the sequence length is 0, as the double amplitude is out of the upper tolerance limit. Line 3 starts a sequence of 8 half cycles or 4 full oscillations, to the end of this example table. All following half cycles are within the tolerances of the lower value and the within the permissible double amplitude range. All other sequences are shorter, and the two recognized pauses in line 7 and 9 of the table do not start new sequences. Figure 3.4 shows the sequence that starts at line 3 of Table 3.1. The numbers identify the half cycles with 1 being the first half cycle of the sequence.

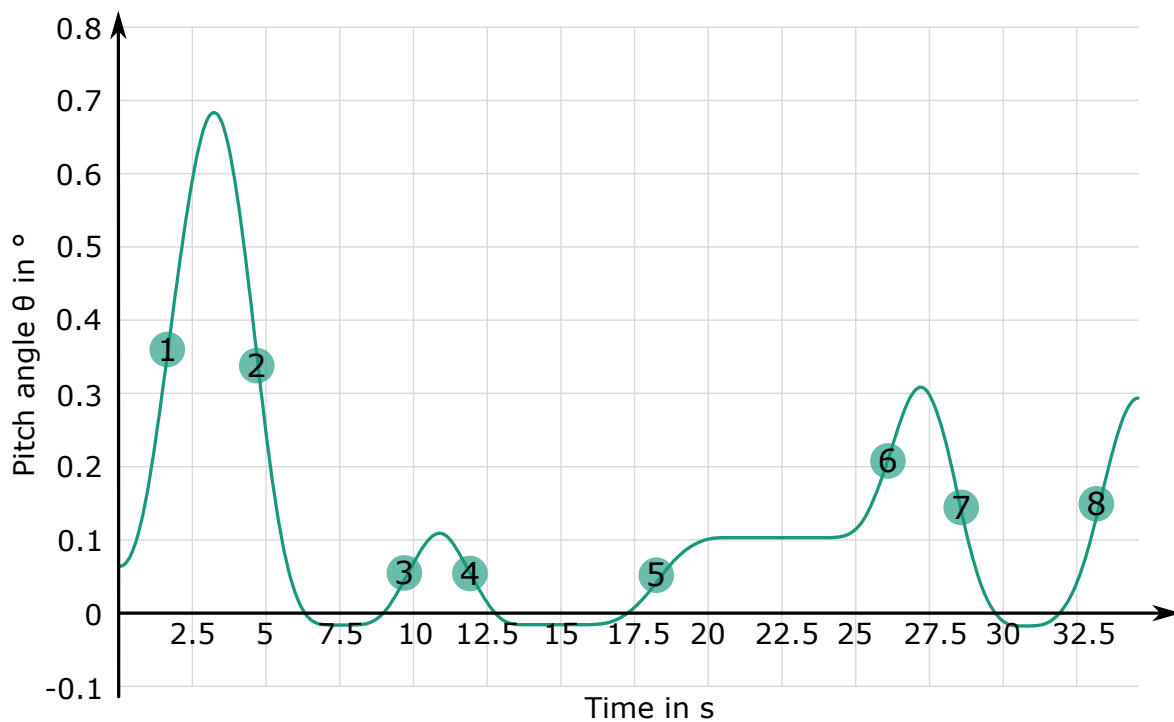


Figure 3.4: Visualization of example sequence

In this example, the sequence lengths for all three tolerance values (lower value, minimum and maximum amplitude) are not the same. If only bottom value tolerances were taken into account, the sequence length would be 10, but the allowable maximum amplitude eliminates the first two sequences. The algorithm keeps the lowest value of all tolerances. This value is 8, as described above. In this example, the longest sequence starts in line 3, and there is no longer sequence in any of the lines that belong to it. It is possible, however, to have longer sequences to start within previous sequences.

Hence, the MATLAB program needs to identify the longest uninterrupted sequences. Uninterrupted in this case means there are no longer sequences starting before a previous sequence has finished. The program processes each sequence and checks for any longer sequence that starts within its duration. If there is no longer sequence, the current sequence is kept and all sequences within the duration of the current sequence are discarded. If there is, the current sequence is discarded and the longer sequence is kept. Table 3.2 visualizes this concept. Each column of the Table is one step of the process and has an index. The rows are a set of sequence lengths, similar to the one shown in Table 3.1. The cells in green are the ones the algorithm processes in the respective step.

Table 3.2: Sequence Elimination Process

	Process step			
	0	1	2	3
Sequence length	Sequence length	Sequence length	Sequence length	Sequence length
3	3	3	3	3
2				
1				
4	4			
3	3			
6	6	6	6	6
5	5	5	5	
4	4	4	4	
3	3	3	3	
2	2	2	2	
1	1	1	1	

(0) shows the input array with the raw output of sequence lengths for each line. (1) shows the first step of the algorithm. The sequence length is 3, and within the two following lines of *cycleTstore*, no longer sequence starts. The sequence of line 1 is kept, the following two sequences are discarded. Line 2 and 3 are skipped as there are no more sequences. (2) is the evaluation of line 4 of *cycleTstore*. The sequence length is 4, but at line 6 there is a sequence with a length of 6. The algorithm discards the sequences that start in 4 and 5 and goes to line 6. As there are no longer sequences in the following lines, this sequence is kept and the following sequences are discarded (3). The final result are two sequences with lengths of 3 and 6 half cycles.

The result of the sequence recognition is a set of potentially harmful and potentially beneficial sequences. If a sequence is harmful or not depends on the movement type (see Section 2.3.2 on operating conditions and the later section on scaled sequence tests). Such sequences allow to compose a test run for raceway wear damage modes.

Chapter 4

Scaled Sequence Tests

4.1 Reasons for Scaled Sequence Tests

Of the four principal movement patterns of pitch bearings (see Section 2.3.2 on operating conditions), only one is clearly known as harmful for the raceways. Pattern type 1 with constant or almost constant (small) amplitudes and mean values will result in wear damage on a raceway, as numerous publications in this field have shown. As the conditions for lubricant film buildup and tribolayer get better with larger amplitudes, it can be assumed that this wear risk disappears with sufficiently large amplitudes. To the knowledge of the author, this amplitude is not yet known. Pattern 2 is suspected to facilitate tribolayer buildup and hence protect the raceway, whereas the influence of pattern 3 is unknown. Pauses (pattern 4) in combination with dynamic loads were shown to facilitate False Brinelling in [95], and the author has witnessed such a damage on a real pitch bearing (Figure 2.34 shows this).

This state of knowledge lacks some pieces of information to build up a test profile:

- Influence of pattern 3
- Confirmation of tribolayer buildup in pattern 2
- Influence of pattern 4

Over the course of the projects this work bases upon, test data available to the author confirmed the tribolayer buildup during movement pattern 2 and its beneficial influence on raceways. Unfortunately, this data is confidential and cannot serve as reference. Further data had to be created, and as real scale tests came at prohibitive costs, the author proposed to do scaled tests of sequences.

The underlying assumption of scaled tests is that it is possible to reproduce the occurrence of wear damage modes of full scale pitch bearings in smaller bearings. As wear is a fundamental principle in all contacts and the contact conditions are similar (pressure, material, lubricant), the author deems this assumption to be reasonable. The specific conditions of pitch bearings, as load distribution, large dimensions, and dynamic loads, influence the progression of wear damage, and an acceptance run has to be carried out under realistic conditions. General damage occurrence,

however, the understanding of which allows to set up a profile for an acceptance run, is assumed to be similar in small scale. To verify this assumption, a fraction of the scaled tests should be executed on full scale bearings as well.

4.2 Scaling Criteria and Bearing Choice

Wear phenomena are influenced by the energy in the contact, which itself depends on the contact pressure. It is therefore necessary to calculate the contact pressure as a function of the outer loads of the pitch bearings and apply loads to the small scale bearings that result in the same pressure values. Some publications on wear damage [126, 127] showed that the contact pressure has limited influence on the wear damage progression, as long as it is above a threshold value. Hence, it is not necessary to achieve an exact load to understand the influence of movement patterns on wear phenomena. Table 4.1 lists the contact pressure values of the IWT pitch bearing on the inner ring as a function of axial load. These values have been calculated with the method shown in Section 2.2.2. This method does not allow to calculate the free contact angle, and in this case the manufacturing contact angle of 45° was kept constant. This results in slight inaccuracies, which are acceptable as per the above note on loads and wear damage. As the load influence is limited, it is also reasonable to apply static loads, which reduces the test costs significantly.

Table 4.1: Contact pressure as a function of axial loads of the IMO 12480 bearing

Axial load kN	Contact pressure MPa
0	0.00
2000	1178.47
4000	1484.78
6000	1699.65
8000	1870.70
10000	2015.15

Oscillatory movements of bearings have two main properties which are the amplitude and the frequency / speed. The amplitude as absolute value, however, is a misleading property, as the relation between travel and contact area width changes with bearing size. This relation $x/2b$ (introduced in Section 2.2.3 on bearing kinematics) is to be kept constant for any scaled tests. For frequency and speed, this is not possible, as either frequency is constant and speeds gets slower, or speed is constant and frequency rises with smaller bearing sizes. Research on tribolayers indicates that buildup is a function of available time [59]. Therefore, the frequency is kept similar to the movement of full scale bearings.

The slip behavior in the contact should be as close as possible to the full scale situation. The rolling body has to be a ball, and it needs a contact angle in the range of 40 – 60° to have similar

slip components. The lubricant is the same as in the full scale tests. The flooding of the contact area can be different due to its smaller dimensions, but to the knowledge of the author there is no means to counteract this. As lubricant film buildup is deemed less important than tribolayer formation, it is of higher importance to have the same additive package and overall composition of the grease than to have similar flooding times.

There are other geometrical dimensions like the oscillation angle necessary to make one rolling element reach the position another rolling element had at the beginning of the movement, and like the angle necessary to do a half or full rotation of a rolling element. These dimensions appear in some publications and guidelines as thresholds for damage risks [9]. To the knowledge of the author, there are no scientific test results available to support these assumptions, hence they are not considered for the scaling.

In summary, these are the criteria for scaled bearing tests of grease-lubricated, oscillating bearings:

- Contact pressure close to full scale
- $x/2b$ equal to full scale
- Frequency close to full scale
- Lubricant identical to full scale
- Similar contact type (kinematics, kinetics)

Within the HAPT project, Schwack ran tests on type 7208 bearings with an outer diameter of 80 mm. These are angular contact ball bearings with an outer diameter of 80 mm. For the scaled tests with different movement patterns, a new test rig had to be created. This gave the possibility to choose other bearing types. As the 7208 bearings have a similar contact type to four-point contact bearings, it was reasonable to stick to this bearing type, also to maintain comparability with these tests done by Schwack. However, it was possible to get closer to the full scale conditions within the allowable budget, and the author chose larger 7220 bearings. Figure 4.1 shows a sketch of a 7220 bearing.

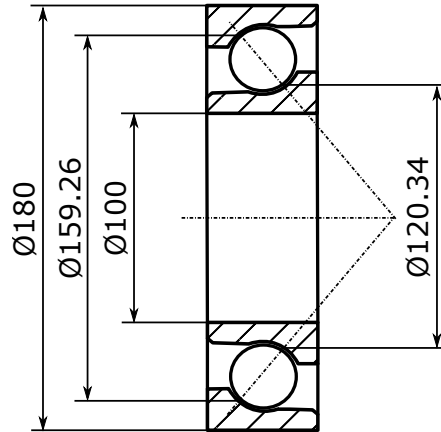


Figure 4.1: Sketch of the type 7220 bearing

Table 4.2 lists additional properties of the type 7220 bearing. The osculation was measured with a laser-scan microscope.

Table 4.2: Main properties of the type 7220 bearings

Property	Symbol	Value	Unit
Ball count per row	z	15	-
Ball radius	R_{x_1}, R_{y_1}	12.700	mm
Outer raceway radius in x	R_{x_2O}	79.630	mm
Inner raceway radius in x	R_{x_2I}	60.170	mm
Osculation (outer ring)	ϕ_O	0.522	-
Osculation (inner ring)	ϕ_I	0.520	-
Contact angle	α_c	40	$^\circ$

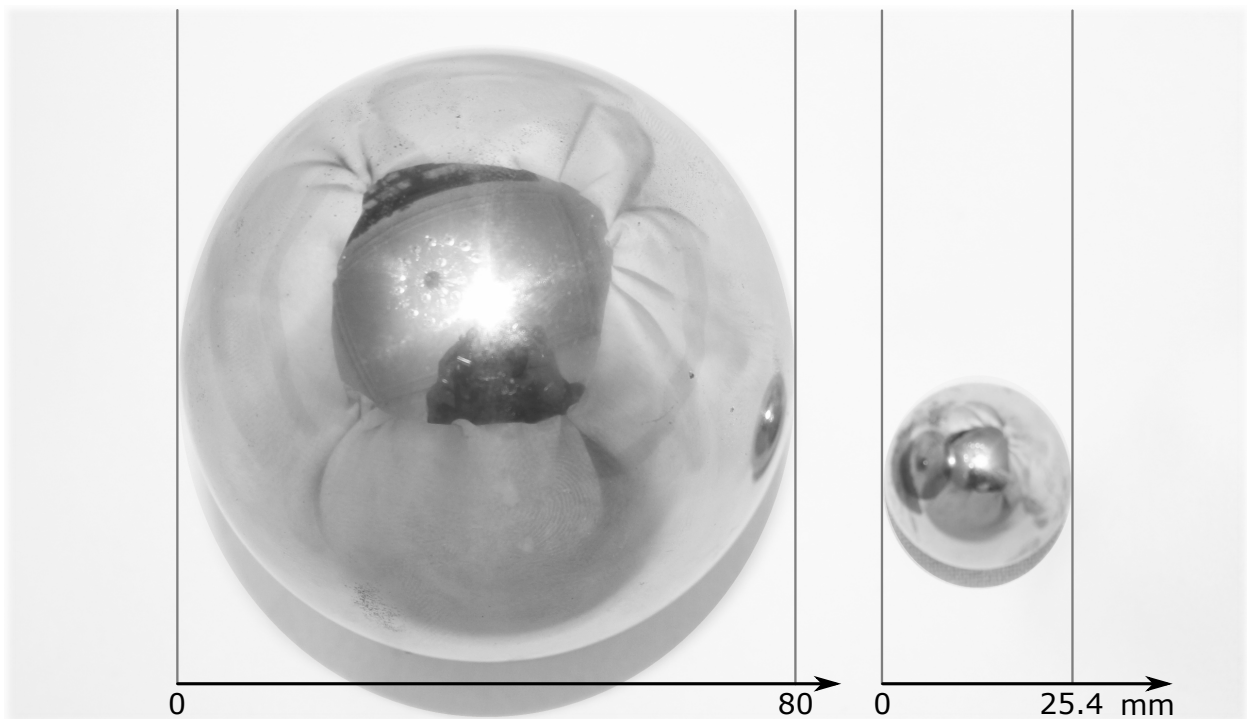
Table 4.3 repeats the layout of Table 4.1 and shows the contact pressures as function of the axial load, this time for the type 7220 bearing. Similar contact pressures need 0.5% of the axial force. 90 kN is added as an additional load step to reach approximately 2.5 GPa, as this is a value commonly used for other wear tests.

The bearing friction was calculated using the equations published by SKF in their catalogue [128]. According to these, the friction torque at 500 rpm and an outer load of 100 kN, the friction torque results in 10.8 Nm. A typical shaft design incorporates two angular contact bearings, which results in 21.6 Nm of friction torque.

Figure 4.2 is a photograph of a ball of the IWT pitch bearing and a ball of the type 7220 bearing. It shows the considerable difference between the ball sizes (and consequentially the sizes of the contact areas).

Table 4.3: Inner ring contact pressure as a function of axial loads of the type 7220 bearing

Axial load kN	Contact pressure MPa
0	0.00
10	1187.73
20	1496.45
30	1713.01
40	1885.41
50	2031.00
90	2470.58

**Figure 4.2:** Photograph of a ball of the IWT pitch bearing (left) next to a 7220 ball (right)

4.3 BEAT0.1 Test Rig and Test Program

The author used the aforementioned requirements to develop a test rig concept for the scaled tests. The name of this rig is BEAT0.1 (Bearing Endurance and Acceptance Test rig, the zero refers to the pitch bearing diameter well below 1 m and the .1 indicates it is the first test rig of this size class at the Fraunhofer IWES). The test rig for the scaled tests has to fulfill the following requirements:

- Shaft and housing for type 7220 bearings
- Application of static axial loads up to 90 kN
- Ability to run any movement sequences
- Minimum drive torque of 21.6 Nm
- Suitability to test a high number of bearings (exchange time, overall lifetime)

The evaluation of a test result consists mainly in the visual inspection of the bearing rings and balls. In a basic approach, the test rig thus does not need any data acquisition. However, any drive with the capability to execute complex movements needs to have a position sensor. As the rig should also allow other test types, the author added the following requirements to this list:

- Position and torque measurement
- Data acquisition with up to eight channels
- Data base to store any measurement data
- Graphical interface that allows to configure test and data acquisition configurations

The load application is realized with a rigging cylinder and a manual pump with a locking valve and an analogue manometer. The bearing drive is a servo drive motor with a peak torque of 50 Nm and a maximum speed of 76 rpm at the output. It is powered by a converter with an allowable continuous power of 2 kW. The torque and position measurement are combined in a HBM T21M torque and velocity sensor. Any parasitical loads on the torque measurement are decoupled with two bellow clutches between main shaft and torque meter and torque meter and drive. Figure 4.3 shows the assembly. The main shaft needs two bearings, hence each test delivers results for two bearings.

As the angular contact ball bearings convert axial loads into radial loads, it is possible that parts of the loads are not supported by the balls, but are transferred directly from the outer ring into the housing. Figure 4.4 shows how the cylinder force leads to bearing forces (labeled 1) and the overall reaction force in the drive-side cover (labeled 3). The forces labeled 2 are parasitical loads between the cylinder-side outer ring and the housing of the rig, which reduce the bearing forces. It is not possible to calculate the exact magnitude of these forces. This is a limitation shared with other test rigs for axial load applications (see for example the test rig sketches in [129]). Given the aforementioned permissible tolerance of the applied load, it does not prevent the tests from

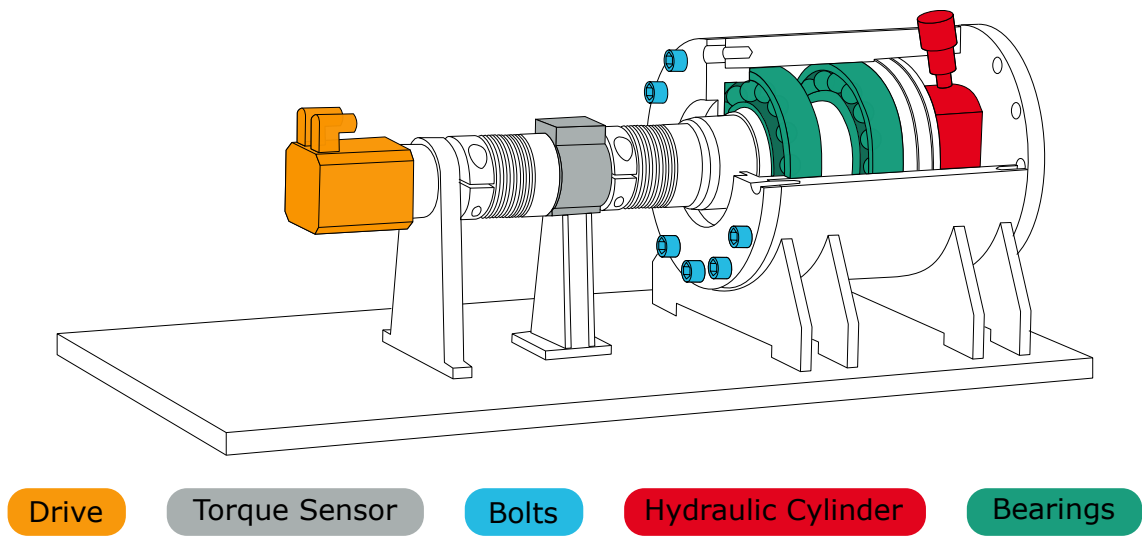


Figure 4.3: Sketch of the BEAT0.1 rig

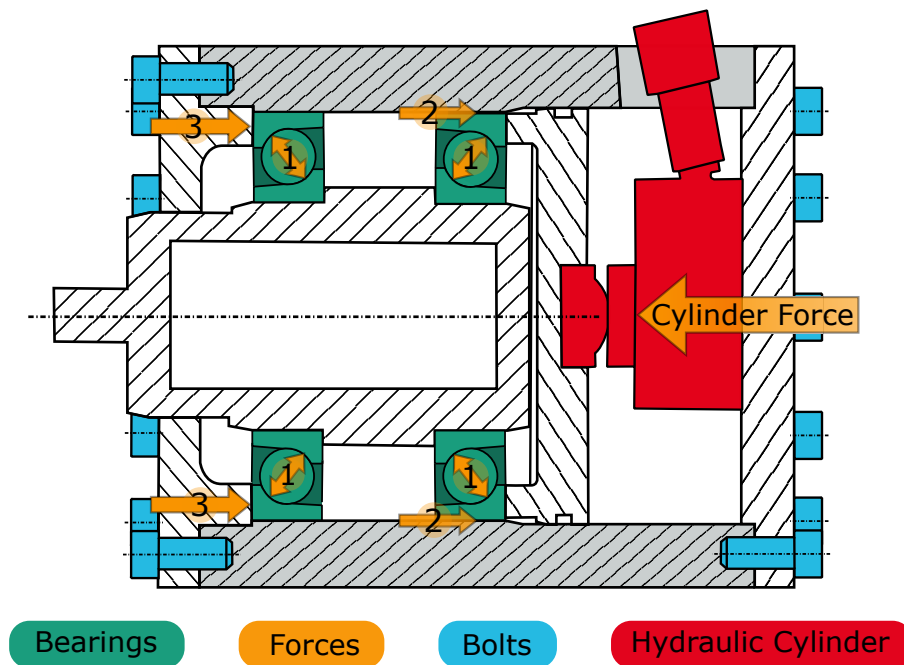


Figure 4.4: Possible paths of parasitical loads in the BEAT0.1 rig

delivering meaningful results. With the later results, the height of damage patches was compared to the expected height of the contact ellipse at the target load, and this comparison confirmed the minor influence of the parasitical loads.

In [130], the author published test results of the BEAT0.1. The following test description and test results partly stem from this publication. Based on the aforementioned test results of the initial 3 MW blade bearing test rig (see Figure 2.42 in Section 2.6), the author defined a reference wear test that resembles movement pattern 1. This test comprises 40000 full cycles of ramps with a double amplitude of 3.95° at a load of 90 kN and a speed of $4^\circ/\text{s}$ (see Figure 4.5). The $x/2b$ for this double amplitude equals approximately 4.7.

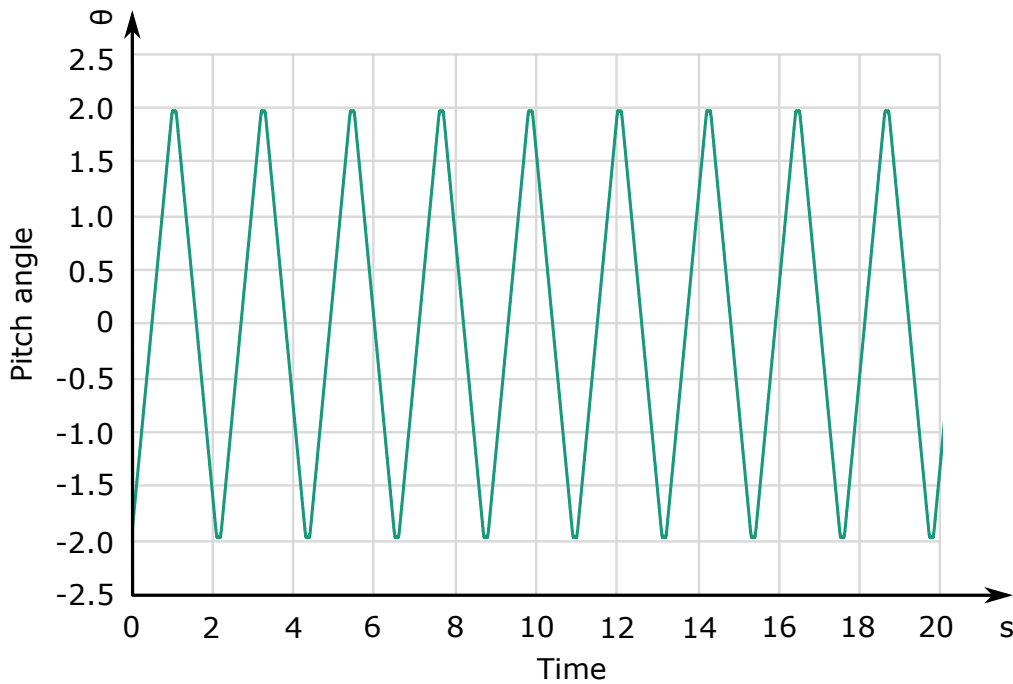


Figure 4.5: Reference test of movement pattern 1

Table 4.4 lists the complete test program. In the header, DA stands for double amplitude. All tests comprised 40000 cycles of a low double amplitude, and some of them had additional longer movements to replicate movement patterns 2 and 3. Test ID 2 has an increased double amplitude of 8.74° (corresponding to an $x/2b$ of 12) to evaluate a possible upper limit of wear creation.

Test ID 3 varies ID 1 and 2 in a way that is closer to the behavior of the IWT controller, with one end value being constant and the other randomized (see Figure 4.6). Test IDs 4 to 8 include different variants of possible protection runs (see Figures 4.7 and 4.8). A protection run is any movement capable of building up tribolayers that protect the raceway against wear damage. If a movement is an actual protection run has to be determined by tests. Test ID 9 repeats ID 1 with a lower axial load that corresponds to 2 GPa contact pressure. This load variation serves to validate the low influence of load on wear damage. In addition to these tests, one test with full rotations at a speed of $4^\circ/\text{s}$, 90 kN, and a duration of 22 hours ensured that the test conditions do not

Table 4.4: Test program for scaled sequence test

Test ID	Bearing IDs	Axial Load kN	Movement Pattern	Low DA °	High DA °	High DA Cycles
1	0005 0006	90	1	3.95	-	-
2	0019 0020	90	1	8.74	-	-
3	0025 0026	90	1	3.5 to 17.4	-	-
4	0007 0008	90	2	3.95	19.75	1000
5	0009 0010	90	2	3.95	79	1333
6	0021 0022	90	2	3.95	79	4000
7	0023 0024	90	2	3.95	79	400
8	0017 0018	90	3	3.95	79	1333
9	0013 0014	50	1	3.95	-	-

cause wear if the bearing does not oscillate. The author published the program and results of IDs 1 – 8 in [130], whereas ID 9 and the reference test with full scale bearings are first published in this thesis.

To obtain reference results from full scale bearings, two type 12480 bearings ran two tests with movement types 1 and 2 (see Table 4.5). The mean value of the small oscillation was varied by 0.80° between these tests to acquire results on different areas of the raceway. The $x/2b$ value of these runs is smaller than of the type 7220 reference test (3 instead of 4.7). Within the HAPT project, Schwack obtained results for bearings with 700 mm diameter and an identical $x/2b$ of 3. These results are comparable to those with an $x/2b$ of 4.7. The load was set to 10 MN axial load, which corresponds to 2 GPa contact pressure. The pitch speed of the test was $3^\circ/\text{s}$, this speed is similar to the test speed of the BEAT0.1 rig.

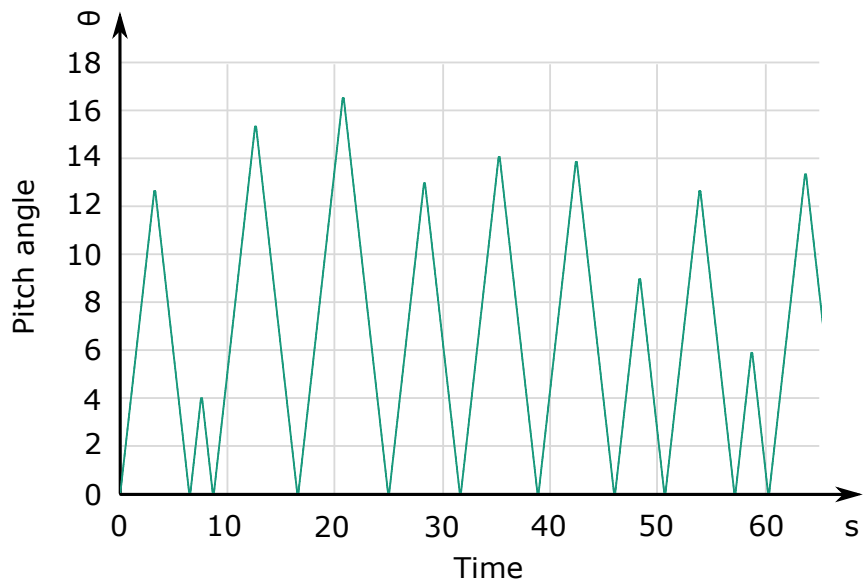


Figure 4.6: Test ID 3 with random amplitudes

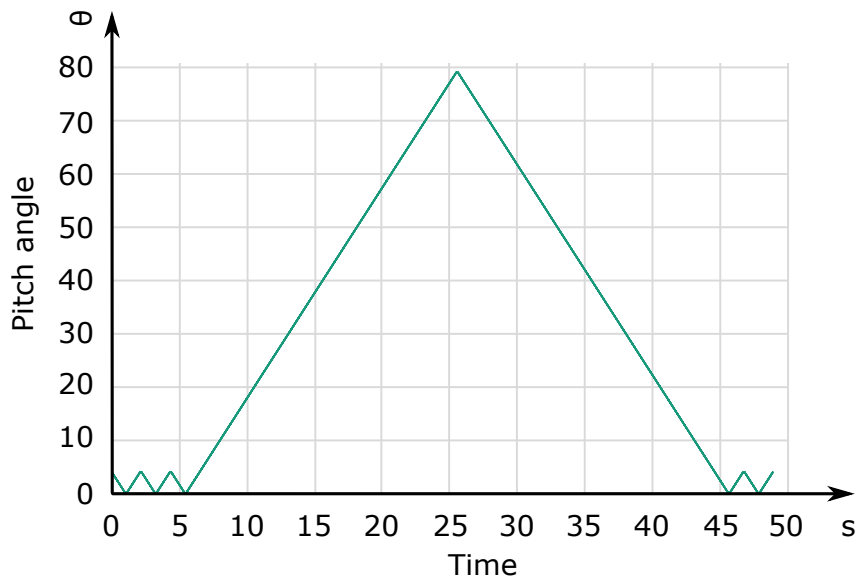


Figure 4.7: Test IDs 4 to 7 with continuous protection runs

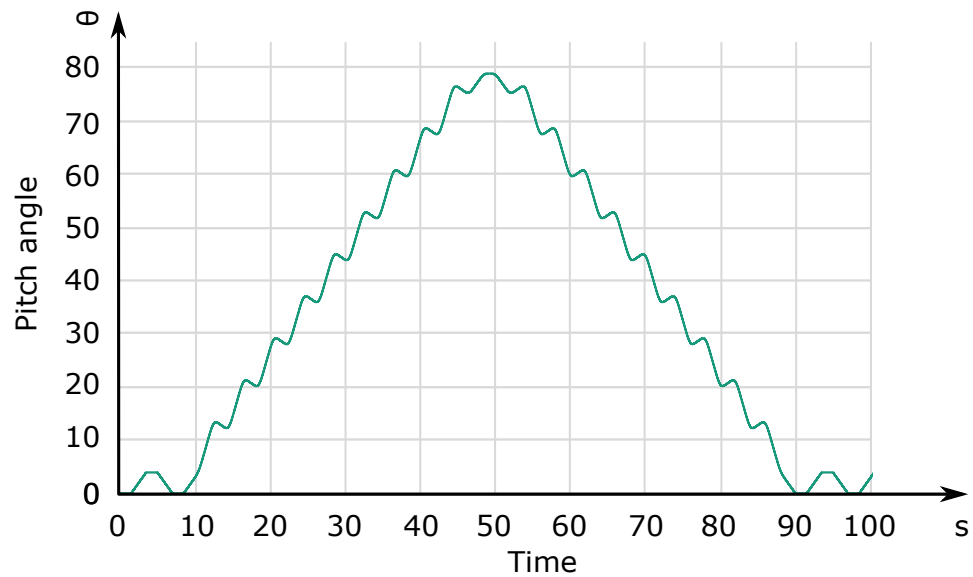


Figure 4.8: Test IDs 8 with interrupted protection run

Table 4.5: Reference tests with type 12480 pitch bearings

Test ID	Bearing IDs	Axial Load kN	Movement Pattern	Low DA °	High DA °	High DA Cycles
-	-	-	-	°	°	°
10	0001 0002	10000	1	0.4	-	-
11	0001 0002	10000	2	0.4	8	1333

4.4 Results of Scaled Sequence Tests and Reference Tests

The following figures show the condition of the inner raceway after each test. These photographs were taken with an optical microscope, except for the full scale bearings, where the pictures were taken with a digital camera. Note that the surface of the bearings shows a reflection of the microscope lense on all pictures. The figures in this section show exemplary raceway condition, a more exhaustive collection of raceway conditions is part of the annex. The test with full rotations did not provoke any visible damage to the raceways.

Figure 4.9 shows two exemplary damage patches for test ID 1 without protection runs. The bearings of test ID show a clearly visible damage patch for each rolling contact. The patches contain corrosion products and have an increased surface roughness.

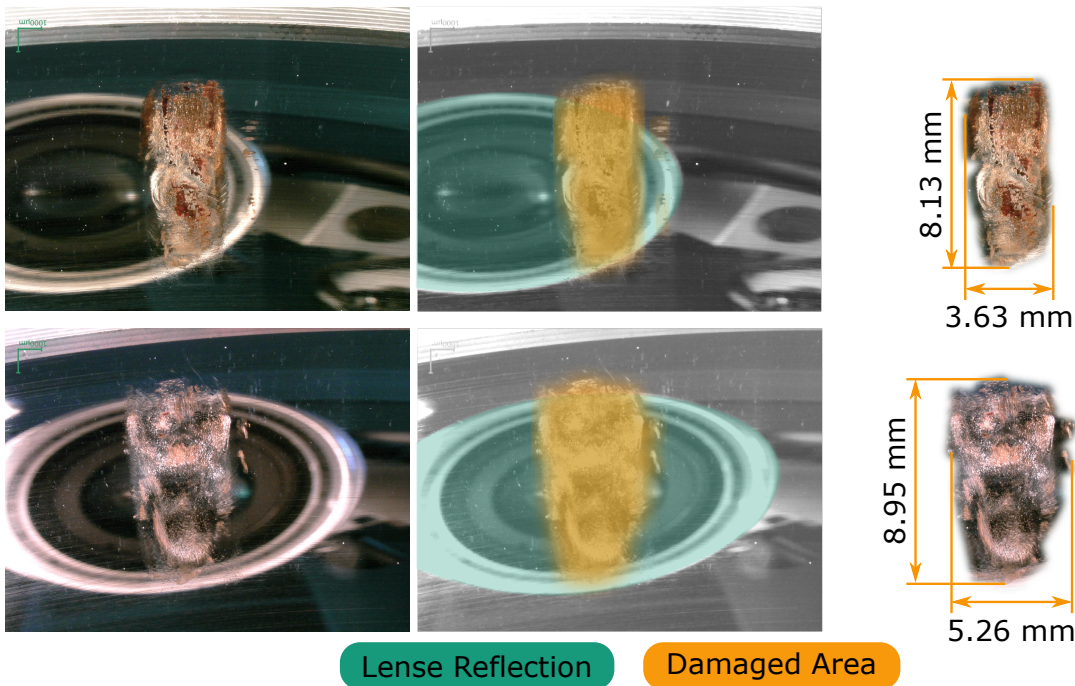


Figure 4.9: Exemplary raceway condition inner ring, Test ID 1, Bearing ID 0006

Test ID 2 has more than twice the travel compared to test ID 1, note that the severely damaged area does not increase accordingly. Figure 4.10 shows two exemplary damage patches of this test. In comparison to test ID1, the corrosional damage is less pronounced in the influenced area, with a significant fraction being polished in comparison to the manufacturing state.

Test ID 3 (Figure 4.11) displays the most severe damage on the raceways, the turning point shared by all cycles is on the right side of the picture, the variable turning points are on the left side.

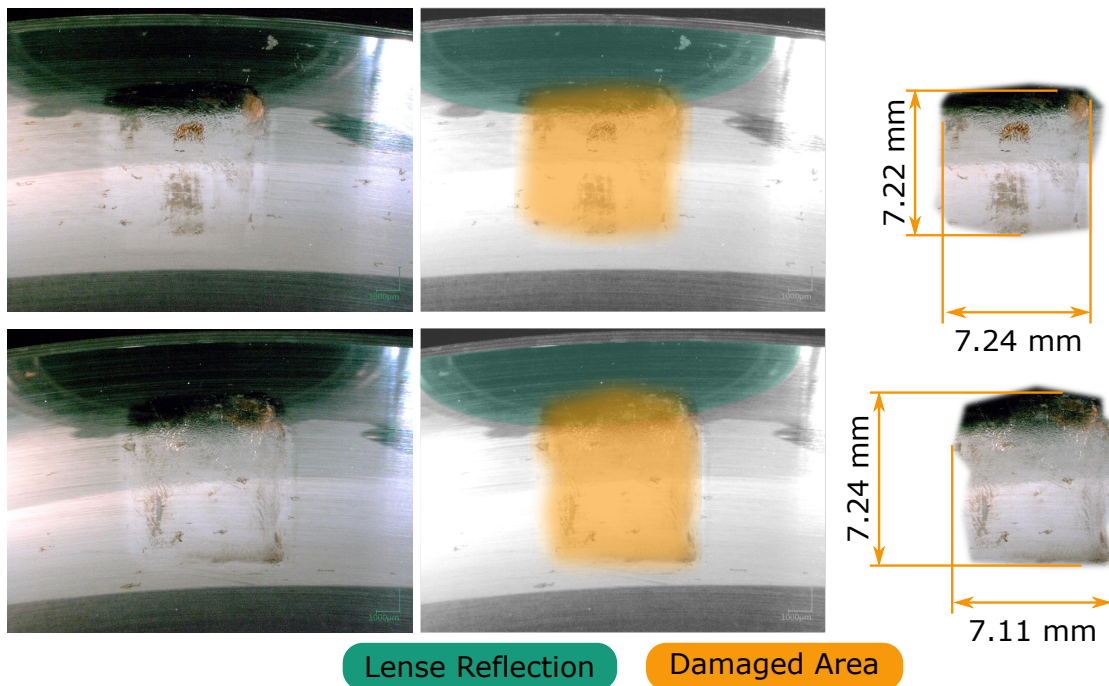


Figure 4.10: Exemplary raceway condition inner ring, Test ID 2, Bearing ID 0019

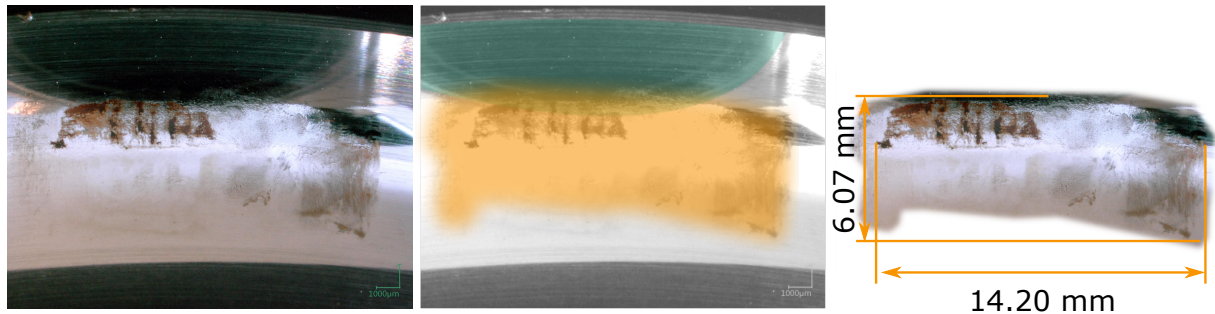


Figure 4.11: Exemplary raceway condition inner ring, Test ID 3, Bearing ID 0026

All these results (ID 1,2, and 3) correspond to the result of the full scale reference test of movement pattern 1 (Test ID 10, see Figure 4.12): The damage patches are clearly visible on the raceway and contain corrosion products. In contrast to the results of the type 7220 bearings, the varying contact angle of the full scale bearings indicates a variation in the load along the circumference. This load variation stems from inhomogeneous interface structures of the test rig. Despite the load variation the damage patches look similar throughout the full bearing, which supports the aforementioned statement of a relatively low load influence on wear damage. The written number is a counter for the balls, 'A' indicates the position of test ID 10, and 'B' indicates the position of test ID 11.

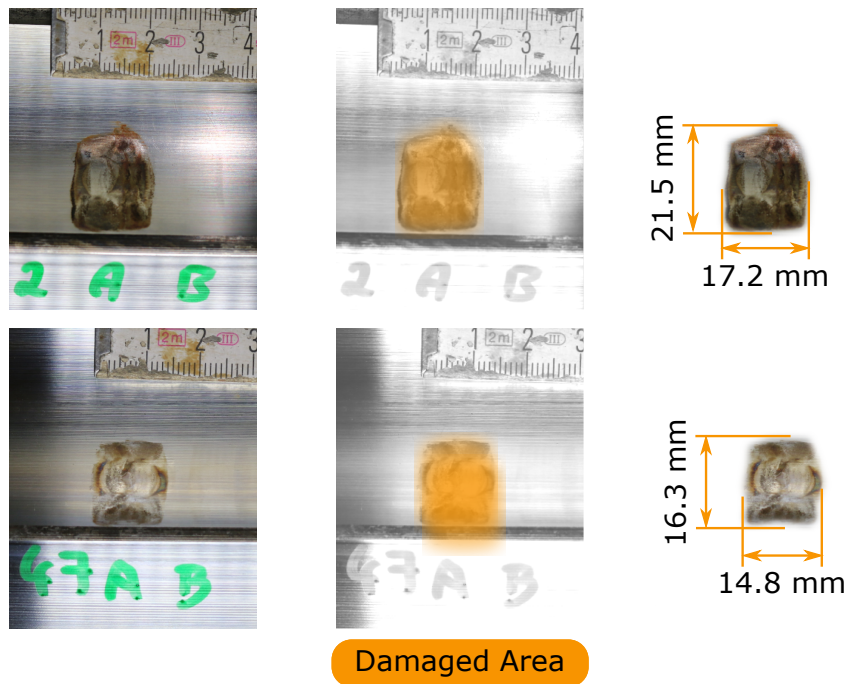


Figure 4.12: Exemplary raceway condition inner ring, Test ID 10, Bearing ID 0001

The results of the test ID 9 with a reduced contact pressure of 2 GPa (see Figure 4.13) further underline this assumption, as they show similar damage areas as those of test ID 1 with higher contact pressure.

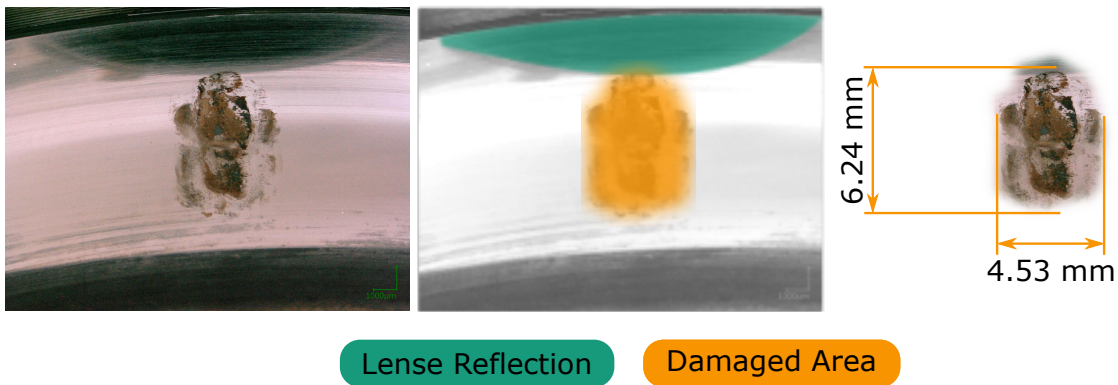


Figure 4.13: Exemplary raceway condition inner ring, Test ID 9, Bearing ID 0013

Figures 4.14 to 4.18 show raceway conditions after tests with assumed protection runs. These are the tests with the ID 4 to 8, which showed varying results. Test ID 4, with a relatively short assumed protection run, resulted in clearly visible damage areas with corrosion products. In some of the areas, black reaction products were found on the surface (Figure 4.14).

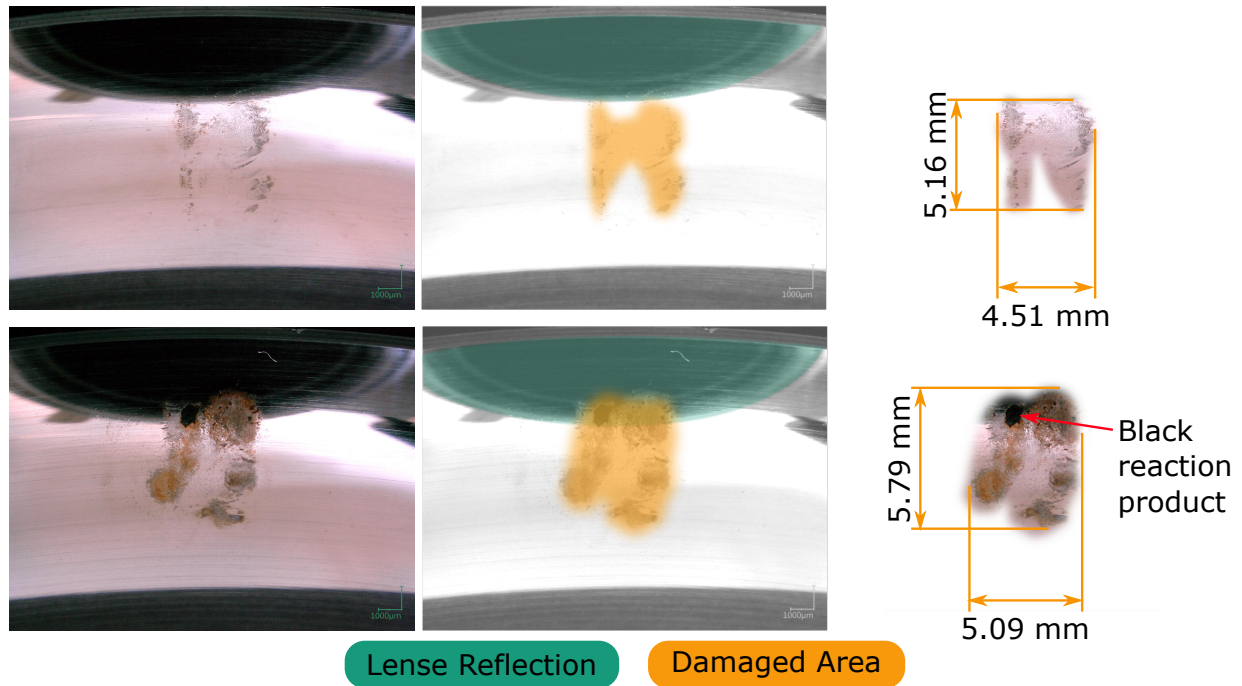


Figure 4.14: Exemplary raceway condition inner ring, Test ID 4, Bearing ID 0007

Test ID 5, with a significantly longer protection run, does not display any corrosion products (Figure 4.15). The visible change on the raceway is limited to a gray area. Of the 15 contact areas, 12 show recognizable changes on the raceway of bearing ID 0009. The shape resembles an incomplete outline of an ellipse and the perpendicular lines that fade out in rolling direction. The manufactured surface structure seems unchanged.

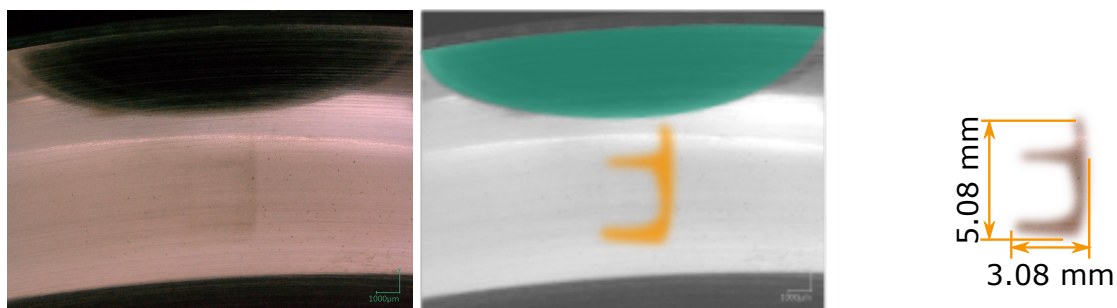


Figure 4.15: Exemplary raceway condition inner ring, Test ID 5, Bearing ID 0009

Test ID 6 (Figure 4.16), which had the same protection run length as ID 5, but more frequent protection runs, does not show any changes to the raceway, similar to bearings with full rotations.

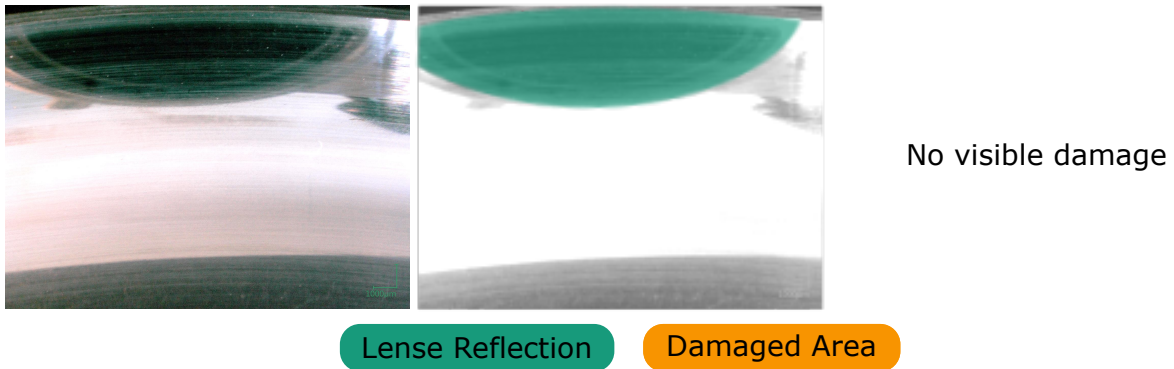


Figure 4.16: Exemplary raceway condition inner ring, Test ID 6, Bearing ID 0021

Test ID 7 and 8 (Figure 4.17 and Figure 4.18) show similar results as Test ID 5. ID 7 showed two small patches with increased roughness. Both IDs do not display any corrosion products.

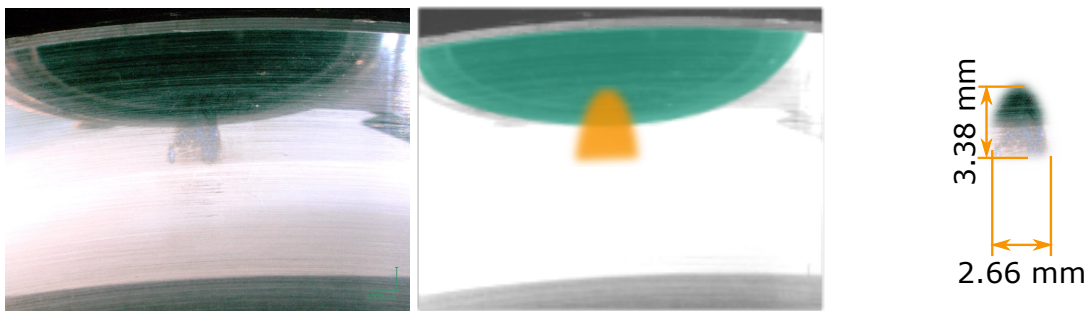


Figure 4.17: Exemplary raceway condition inner ring, Test ID 7, Bearing ID 0023

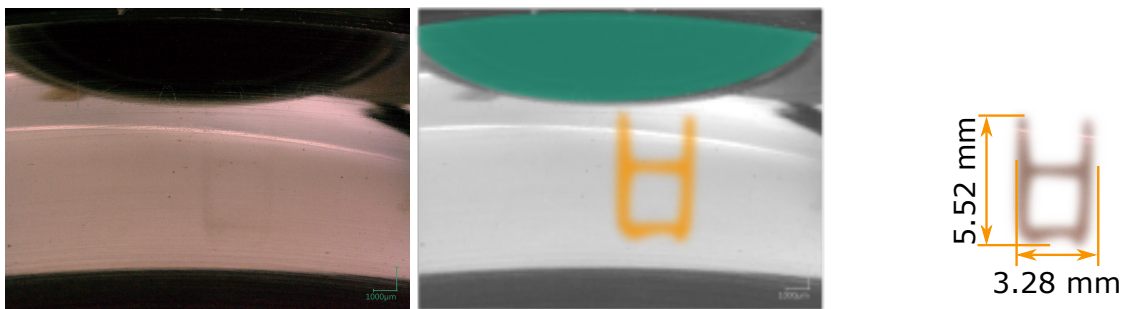


Figure 4.18: Exemplary raceway condition inner ring, Test ID 8, Bearing ID 0017

Test ID 11 (Figure 4.19, indicated by 'B') shows varying results. In most of the contact areas, the protection run was able to protect the raceway, in some cases a smaller damaged area was

found. In contrast to test IDs 5 to 8 with successful protection runs, this protection run had a smaller $x/2b$ of 60 instead of 95. This was a (suspectedly successful) attempt to get closer to a lower boundary for effective protection runs.

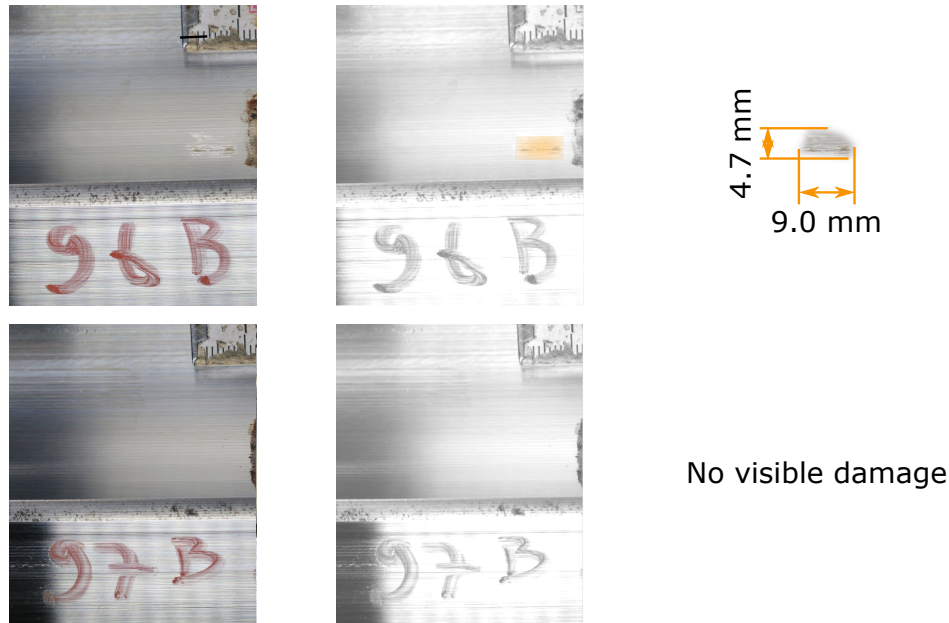


Figure 4.19: Raceway condition inner ring, Test ID 11, Bearing ID 0002

All tests without protection runs resulted in clearly visible damage marks after 40000 cycles. These damage marks contain hematite as a corrosion product. The damage mode is fretting corrosion. In relation to the travel of the ball on the raceway, test ID 2 displays a less severe damage than test ID 1. The author concludes that at some point during the movement with $x/2b$ of 12, lubricant enters the contact and prevents further fretting. Among the tests with protection runs, only the test IDs 5 to 8 were able to prevent fretting corrosion. This is most likely related to the travel of the protection run, which was shortest in test ID 4. The results of ID 11 further support this assumption, as the shorter protection run resulted in damaged raceway areas in some contact patches. The number of cycles in between protection runs seems less relevant for damage formation, as test IDs 5, 6, and 7 demonstrate. However, as 40000 small oscillations provoke clear damages, it can be reasoned that very large numbers of cycles between protection runs render them inefficient.

Test ID 4 showed, in addition to the fretting corrosion, broken flakes on the raceway. For any practical application, this test result is the most critical, as the flakes can cause more damage rapidly if they get into contact areas. Test ID 8 showed similar results to those of test ID 5. The protection run is effective, even if the movement contains interruptions. The interruptions were done at travels similar to the 3.95° of the 40000 reference cycles, and they replicate movement pattern 3. This indicates that it is not necessary to build up a lubricant film to provide the protective capacity of a larger movement. Lubricant films build up with constant, long movements. In the absence of a lubricant film, it is very likely that tribolayers provide the protective effect.

The reference tests with full scale bearings (Test IDs 10 and 11) confirmed the general validity of the concept. For movement pattern 1, they produced similar damage patterns as the small bearings, and the test run of movement pattern 2 showed a significantly reduced overall damage to the raceway in comparison to the one with movement pattern 1.

These results allow the following conclusion for the creation of a wear test run:

- Movement pattern 1 is harmful to the raceway if there is a sufficiently high number of cycles
- Movement patterns 2 and 3 are beneficiary to the raceway if they span a sufficiently high enough overall distance x on the raceway

Chapter 5

Creation of the Test Environment

5.1 Test Rig Purpose

Sections 2.4 and 2.5 established a fundamental concept for pitch bearing tests:

As some damage modes are not completely understood, full scale acceptance runs with realistic interface conditions and loads are the only means to minimize pitch bearing failures prior to the installation in wind turbines.

Of the test rigs shown in Section 2.6, none is capable of reproducing the interface conditions while at the same time applying dynamic loads. The lack of realistic interface conditions for all-steel test rigs of bearing manufacturers is obvious and does not need any further explanation. For the rigs with real interfaces, the lack of dynamic load application is less obvious, but can be explained as follows: The blade structure is designed to cope with loads that spread along the length of the blade. Applying the entire load to one individual point would destroy the local structure. For this reason, extreme load test setups for blades apply the loads to several points along the length of the blade. Figure 5.1 shows a test setup for an extreme load test at Fraunhofer IWES [131].

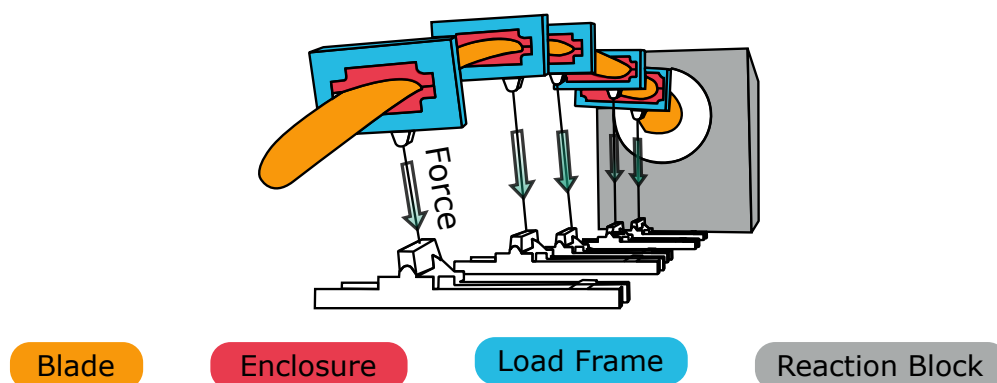


Figure 5.1: Load application for an extreme load test of a blade

The loads are introduced at five points by ropes that attach to load frames which replicate the outer shape of the blade. Coming back to the initial issue of dynamic load application in various degrees of freedom: The necessary structures and control system to apply the loads dynamically to five points along the blade would come at very high costs and complexity, and it seems impossible to the author to apply dynamic axial loads without altering the blade's structure.

These rigs hence cannot execute full acceptance runs, but serve other purposes:

- Understand real-size contact phenomena
- Rolling contact fatigue tests (based on currently available calculation methods)
- Functionality tests of pitch systems (bearing + interfaces)
- Extreme load tests

As such, they deliver valuable results that broaden the understanding of pitch bearings, but fail to give the abovementioned indication. The VDI guideline 2206 [132] defines a V-model for the development of mechatronic systems (see Figure 5.2).

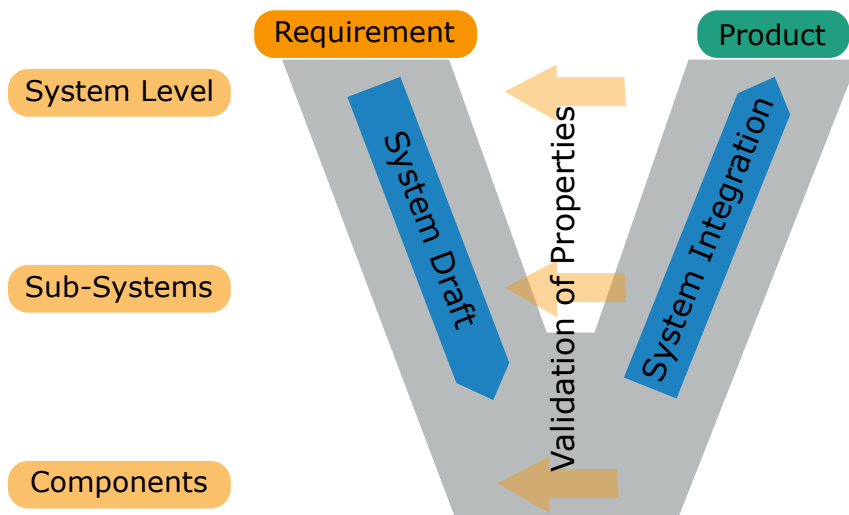


Figure 5.2: V-model according to VDI 2206

This model describes the path from requirements to the final product. It starts at the upper left point of the V with the definition of system-wide requirements. Requirements are further developed down to component level. With these requirements, the components are designed and assembled to the top-level system. At each design level, the model foresees a validation loop to compare the component's capabilities (as defined by the design) with the requirements. In the case of a pitch system (see Figure 5.3), the top system is a wind turbine. Requirements for a wind turbine are rated power, wind class, expected lifetime, availability, capital and operational costs. These are further split into subsystems like the rotor, the drivetrain, or the tower. Requirements for the tower could be height, cost, and loads. The loads stem from the load simulations described

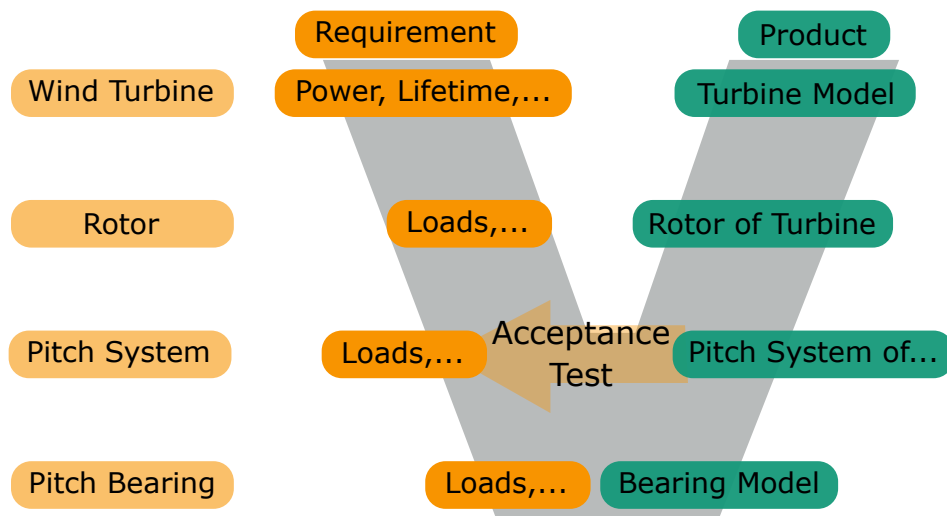


Figure 5.3: V-model for a pitch system

earlier in this work. A sub-subsystem of the rotor is the pitch system, comprising pitch bearing, pitch drives, and additional interfaces. Requirements for the pitch system are loads, pitch speed, reliability, fail safety, costs. A component is the pitch bearing or the bolts that connect the pitch bearing with the hub.

Existing test rigs can validate pitch bearings on a component level, but not for every relevant failure mode. They cannot validate complete pitch systems at all. Closing this gap is the purpose of the test environment that the author describes in this work.

5.2 Design Requirements

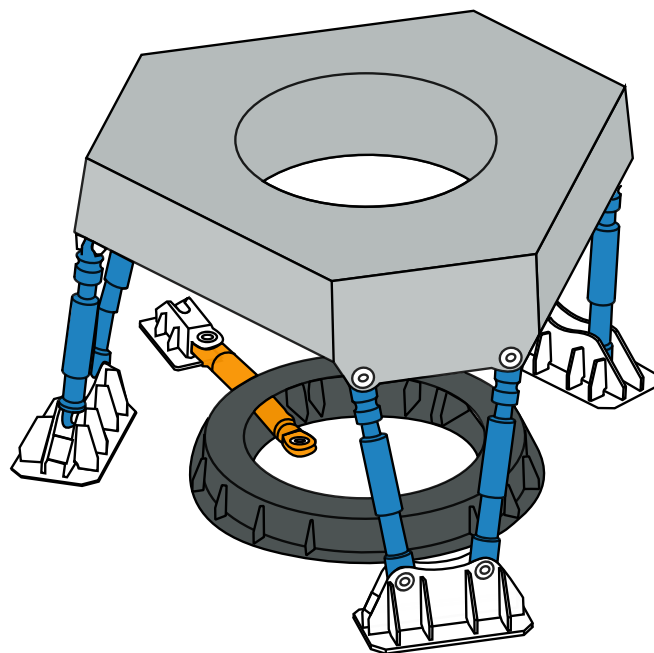
Broer, Steinkuhl, and the author defined the requirements for the test environment in a specification (German: *Lastenheft*). This specification was part of a public tender [133]. The following section refers to this specification.

The two core requirements for the test environment are the ability to apply dynamic loads and the ability to provide realistic interface conditions. Further requirements are:

- Overall costs within the available budget
- Exchangeability of test bearings and interfaces
- Size of the test rig (must fit within test hall)
- Orientation of the bearing
- Safety of workforce and material

- Autonomous operation 24 hours a day, 7 days a week
- Ability to test other bearings or structures than pitch bearings
- Execution of complex test profiles

The application of dynamic loads in various degrees of freedom (DOF) makes hydraulic cylinders the common choice. The arrangement of the cylinders should allow for a high flexibility in terms of load directions. While structures like the KIMM test rig or the test rig by Rothe Erde (see Section 2.6 on test rigs) need a low number of cylinders, they are limited in the co-application of radial loads, bending moments and axial loads [134]. Fraunhofer IWES already gained operating experience with a hexapod platform with the nacelle test rig, and this arrangement is in widespread use for testing and robotic applications. These reasons made a hexapod layout the final choice. As the weight of the structures for the desired load range is significant, due to the space restriction in the test hall, and for a simple connection of the rig to the strong floor, the design team defined the bearing orientation as horizontal. This orientation is also closer to the real conditions in the hub, as the constant rotation of the bearings causes a centrifugal force in z direction, as the gravitational force does for a horizontally oriented bearing. Figure 5.4 shows the main components of the hexapod concept.



Pitch cylinder

Reaction Frame

Load Platform

Load Application System

Figure 5.4: Main components of the hexapod concept

The six quasi-upright hydraulic cylinders form the Load Application System (LAS). A seventh cylinder applies M_z and / or rotates the bearings. The upper steel structure that transmits the

loads from the cylinders to the bearings is called Load Platform (LP). Its lower counterpart which connects the bearings with the foundation is called Reaction Frame (RF).

Hub Adapters (HA), which emulate the behavior of the rotor hub, connect the pitch bearings with the structures of the test rig. Two pitch systems or Devices Under Test (DUT) connect to the HAs, and one Force Transmitting Element (FTE) joins the two DUT and emulates the behavior of the blade. The rig always tests two bearings at the same time. As the test runs will cover wear modes, and given the current state of knowledge about these damage modes, it is not reasonable to have one permanent bearing at the rig. The loads differ slightly between DUT 1 (the lower or primary DUT) and DUT 2 (the upper or secondary DUT), but the author deems the differences to be negligible.

5.3 BEAT6.1 Rig

The final rig is called BEAT6.1 (Bearing Endurance and Acceptance Test rig, the six refers to the pitch bearing diameter of about 6 m and the .1 indicates it is the first test rig of this size class at Fraunhofer IWES). Figure 5.5 shows the test rig with the test assembly that has been used for the acceptance runs described in this thesis. The maximum static load of the rig are 50 MNm bending moment, 10 MN axial load and 1 MN radial load. The pitch cylinder can apply a torque of 2 MNm and move at a speed of up to $10^\circ/\text{s}$. The Hydraulic Power Unit (HPU) has a peak power of 800 kW and a nominal flow of 1480 l/min. Each hydraulic cylinder has a calibrated load cell and position sensor. The overall weight of the test rig is approximately 300 tons, the strong floor has a weight of 2500 tons.



Figure 5.5: BEAT6.1 test rig with hybrid Force Transmitting Element
©: Fraunhofer IWES / Ulrich Perrey

BEAT6.1 has a fully integrated measurement and control system with approximately 500 channels. The control is able to run mathematical (ramps, sinuses) profiles and time series for all 6 DOF independently. Most of the measurement channels store data with a sample rate of 200 Hz in standard operation mode. Vibration and acoustic sensors allow higher frequencies of up to 20 kHz. A five-camera 4k video system can be used for optical analysis of any desired states and 75 TB server capacity allow to store high-frequency data of several months.

The exchange process for upright oriented bearings is straightforward if the overhead cranes have sufficient capacity. For horizontally oriented bearings, one part of the test rig is always above them and prevents the exchange with the overhead cranes. The rig supplier suggested a solution with sliding rails, where an entire test assembly would be pulled out of the rig and disassembled top to bottom (see Figure 5.6). This solution brings the major advantage of bolting operations on horizontal bolt circles and is used in the operation of the rig.

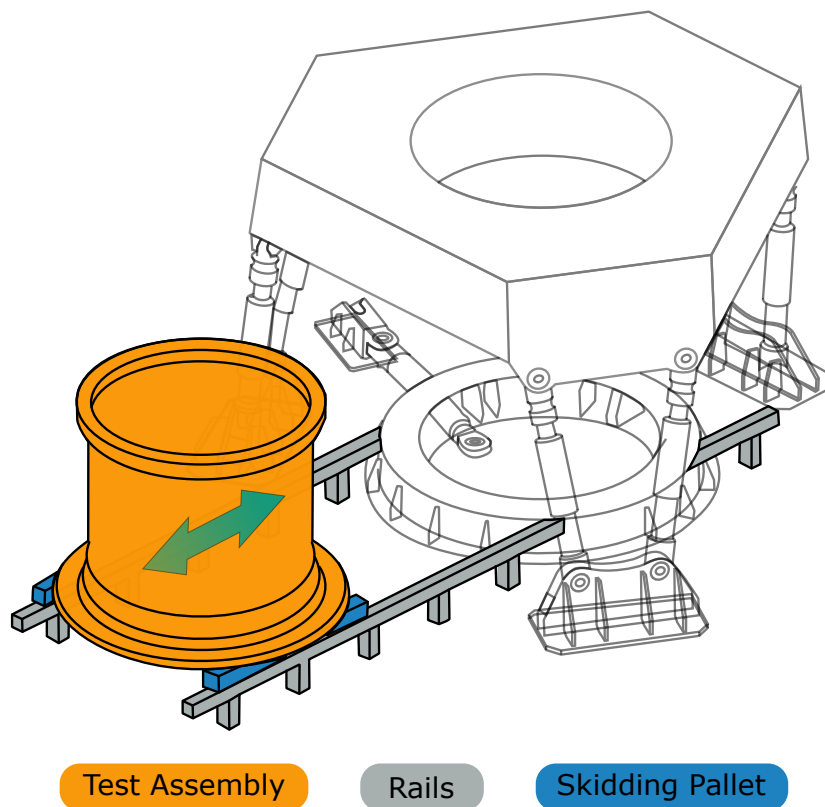


Figure 5.6: Exchange concept for test assemblies

5.4 Emulation Parts

5.4.1 Requirements

The test rig installation space between the lower and upper structures of the rig is 5 m in height and approximately 7 m in diameter. In case of a pitch bearing test, it is necessary to emulate the behavior of hubs and blades and fit the pitch bearings with all stiffener elements in this space.

The main requirement for these adapters is:

Under a given load situation, the load distribution of the rolling bodies (and their contact angle in case of four-point bearings) in the test rig must match the load distribution in the rotor star with a certain tolerance.

Besides this main requirement, the parts need to survive the extreme and fatigue loads of the test. As established in the section on pitch bearing design, FE simulations are the only means to calculate load distributions in pitch bearings. This is the same for the detailed design of the emulation parts. The conceptual phase, however, needs some simplifications. One of them is to limit any calculations to individual interface parts. The other is to limit calculations to axial and radial deformations to get an idea of the underlying behavior of the part.

5.4.2 Hub Adapter

The reference for the Hub Adapter is the hub of the IWT. To understand the possibility of replicating its behavior within the limited available space, the first calculations were done with a hub without any interface parts attached to it. If the pitch bearing flange of the hub (see Figure 2.29) is subjected to an uniform axial load, it deforms in a characteristic way. Figure 5.7 shows this deformation in a sketch and by absolute values for the IWT hub and a M_y of 50 MNm. The green deformation curve is the result of a FE simulation.

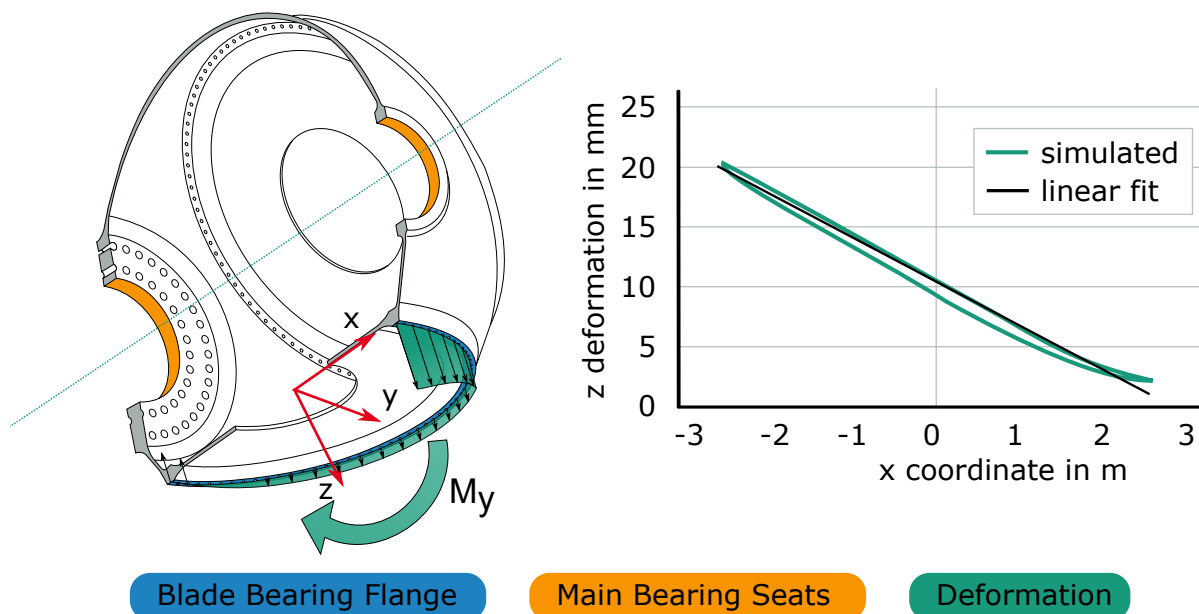


Figure 5.7: Axial deformation of a hub flange under uniform load

Close to the main shaft, the deformation is smallest, while it is largest on the opposite side. This is to be expected, as the hub is fixed to the main shaft. The overall deformation can be approximated as a tilting of the entire flange. The maximum deformation is about 20 mm. The available space in the test rig is limited, and of the 5 m in height it would be reasonable to assume a maximum of 450 mm in Z for each hub adapter. A deformation of 15 mm on 450 mm total length would be a plastic deformation for steel. As a consequence, it is not possible to reproduce the overall deformation in the test rig. The deformation does not change linearly between the two extremes, but shows some deviations from this behavior (see the right part of Figure 5.7). These deviations are caused by the connections to the other blades and other geometric irregularities along the circumference.

The pure tilting part of this movement can be visualized by a plane (or a straight line as in Figure 5.7). This plane does not influence the internal load distribution of the bearing, so the deformation behavior of the Hub Adapter does not need to replicate the absolute deformation of the hub, but only the deformation that resides when a tilting plane is deduced from the absolute values. However, the linear fit plane shown in Figure 5.7 is not a valid approach. It limits the residue deformations to the lowest overall values, but negative and positive deviations from the plane are split by approximately 90° . Figure 5.8 shows this plane in a three dimensional sketch, positive deviations of the hub deformations are shown in green, and negative ones in orange.

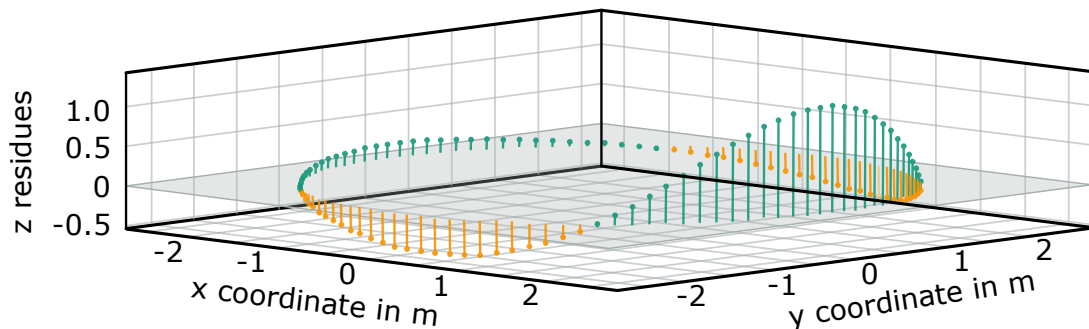


Figure 5.8: Linear fit for axial deformation

The pitch bearing is mostly subject to bending moments (M_y), and the deviations from this plane equal the absolute deformations of the Hub Adapter. Thus, such a plane should fit into the axial deformations in a way that 180° of the circumference have higher values than the plane and the other 180° lower values. Figure 5.9 shows an example custom plane approach. Steinkuhl developed this approach which he and Wenske published in [68]. The custom plane results in higher absolute deformations, but achieves a split into 180° sections.

As the absolute deformations are at approximately 2 mm, it is possible to design a part – within the available space – which axial deformations match those of the hub that influence the pitch bearing. The sections of such a part can be varied in various geometrical parameters to achieve the stiffness variations. Figure 5.10 shows such sections, which form a single-ring Hub Adapter.

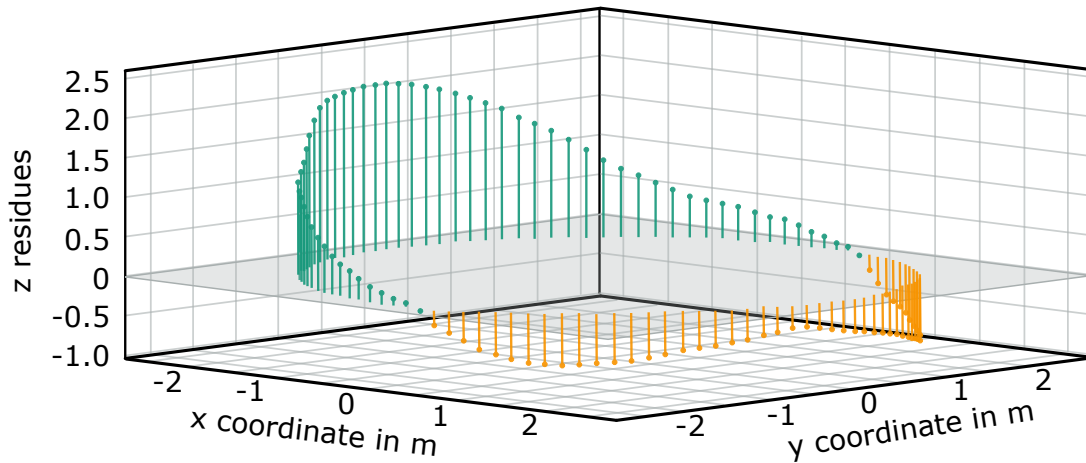


Figure 5.9: Custom plane fit for axial deformation

Such a single ring concept was the initial concept for the Hub Adapter, but proved to have a major disadvantage: If the individual sections deform axially, they behave like beams with one fixed end and bend (see left part of Figure 5.11). This bending results in a tilting of the bearing ring that would influence the bearing load distribution in an unacceptable way. One possible solution is to add another ring that counteracts the tilting of the first (see center part of Figure 5.11). Another solution is to envisage two connection flanges to the test rig structure and the connection to the bearing in the center of them. The right part of Figure 5.11 shows this bridge concept.

In case of the IWT, a double-ring concept was chosen. A bridge concept is more suitable for larger bearings, where the bolt circle of the bearing is in between two bolt circles of the test rig structure, but in the case of the IWT the bearing bolt circle has a smaller diameter than the test rig bolt circles. Figure 5.12 shows this Hub Adapter.

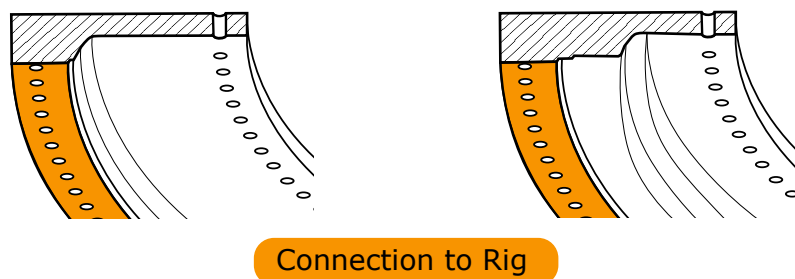


Figure 5.10: Single ring Hub Adapter section

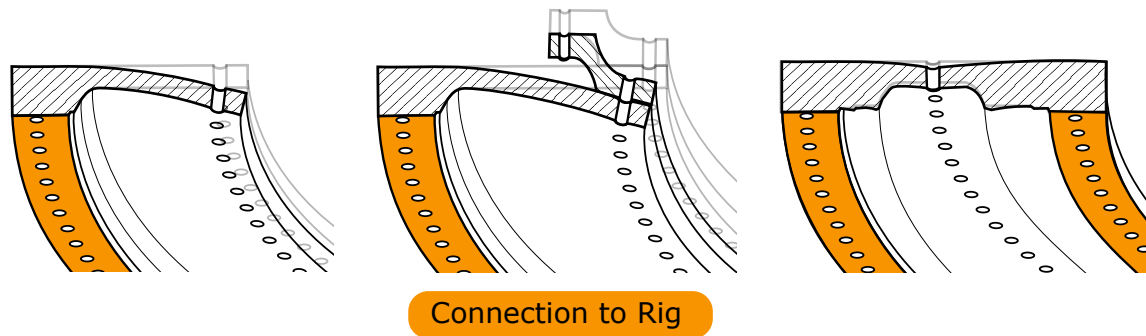


Figure 5.11: Tilting of single ring (left), double ring (center), bridge section (right)

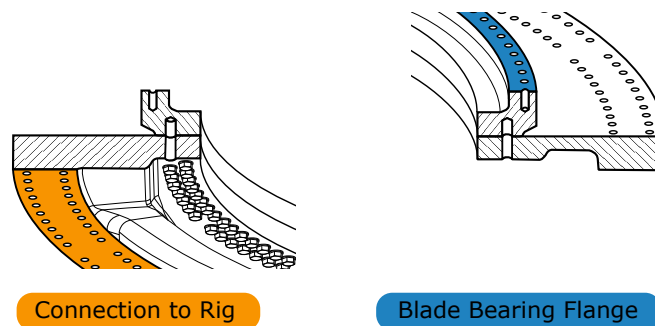


Figure 5.12: Double ring Hub Adapter of the IWT

5.4.3 Force Transition Element

The blade side needs to cover more aspects than this axial deformation. Section 2.3.3 on pitch bearing interfaces defined a set of characteristics that influence the blade – pitch bearing interaction:

- Blade ovalization
- Bolt interfaces
- Axial load distribution

In addition to these, there might be less pronounced properties of the blade, which yet have some influence on the bearing. As such, it seems reasonable to stick to a blade-like structure. Such a structure is a tube made of GFRP (the blade of the IWT is made of GFRP as well) which has the same interface to the bearing as the real blade. In this case, the interface are T-Bolts. In the blade of the IWT, the transition of the quasi-isotropic root material to the spar caps and shear webs takes about 4 m. In the earliest concepts for a FTE, its overall length was set to 10 m

(2 times 4 m plus reserves) [115]. This length allowed to use an all-GFRP part which design is close to a real blade. The later test rig prohibited this solution as it was too long, and the author suggested a hybrid concept of two GFRP rings and steel section in between. The steel sections should take over the part of the spar caps and shear webs, in particular with regard to the axial load distribution, and the GFRP rings should provide realistic bolts interfaces and general blade root behavior. At this point, it seemed reasonable to assume that the natural ovalization of the two 1 m GFRP rings would not be as strong as the ovalization of a full-scale blade. To overcome this, the concept incorporated ovalization cylinders that would introduce additional deformations into the ring.

First simulations with a 3 MW-class bearing and hub showed the general capability of this concept to introduce blade-like loads, but a major concern at this stage was the structural capacity of the GFRP ring interfaces (bolts and ovalization cylinders). On very limited space, the concept brought two full bolt circles and a major ovalization load introduction into the rings, and it was not clear if they could cope with the fatigue loads and deformations.

Later simulations brought some relief on the aspect of ovalization: As described in the Section 2.3.3 on interfaces, a connection of blade and inner ring causes a natural ovalization that needs to be counteracted by a stiffener plate. A stiffener plate on the other side reduces the ovalization to a level even lower than the natural ovalization of the hybrid FTE. Hence, the ovalization cylinders became superfluous, and the hybrid FTE was equipped with a stiffener plate. This greatly reduced the requirements for the GFRP rings, which then only had to incorporate two bolt circles. Over the course of the detailed design (carried out by the company IDOM), tests with individual T-Bolts demonstrated the capability of this interface. Figure 5.13 shows the test setup.

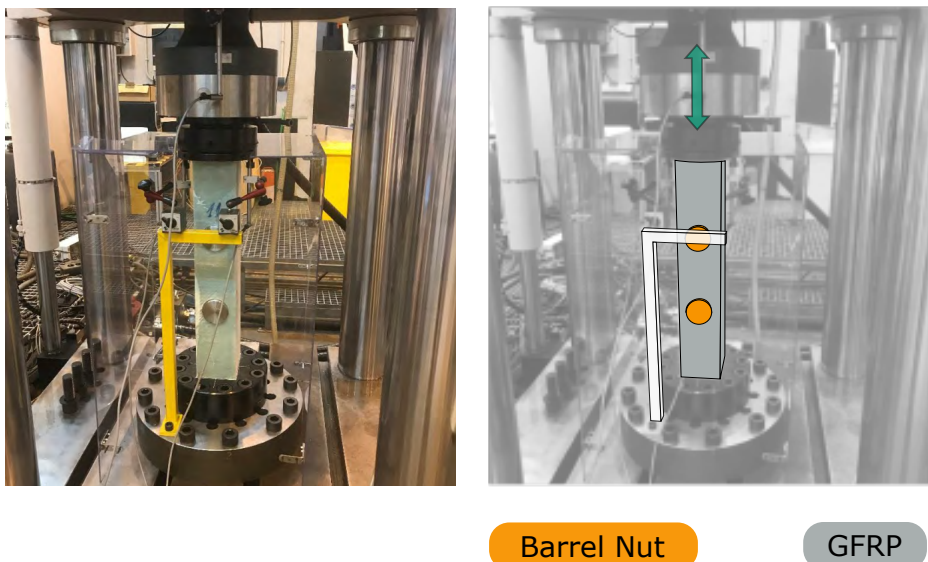


Figure 5.13: Test setup of the T-Bolts
Courtesy of and ©: IDOM / ELEMENT SEVILLA

Figure 5.14 shows the final design of the hybrid FTE. The steel segments can be mounted in any combination along the circumference to simulate different blades (as long as the load carrying capabilities suffice). While they emulate the load distribution for a pure M_y with a high accuracy, the emulation for M_x or combined bending moments needs to be a compromise between capacity and accuracy of the emulation. In this particular design, the maximum M_x -capacity requires steel sections along the x -axis that are slightly too wide to emulate the behavior of the blade accurately.

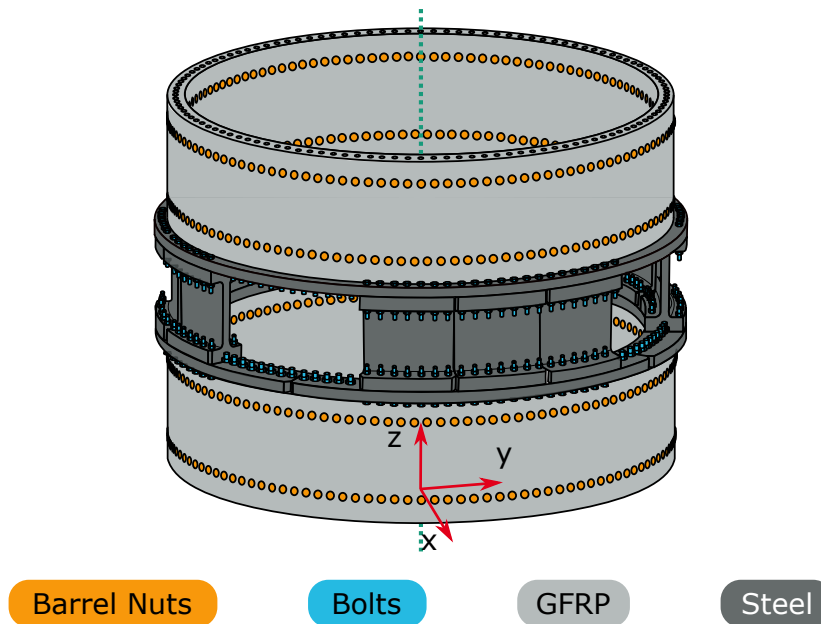


Figure 5.14: Hybrid FTE for the IWT

Chapter 6

Endurance Run Program

6.1 Wear Profile Input

From Section 2.3.2 on pitch bearing operating conditions and Section 4.4 on the results of the scaled sequence tests, the author derives the components of a wear endurance run for pitch bearings. The wear profile consists of any relevant situations in the turbine life and omits any non-relevant conditions. Meaningful situations are those of the movement types 1,2 and 3.

In the MATLAB program (see Section 3.2 on sequence recognition) the parameters listed in Table 6.1 were set to find occurrences of movement pattern 1. Pattern 3 was defined as any movement with a total span of 15° or higher. Pattern 2 occurrences are limited to start and stop situations. For the latter, two simulation files of DLCs 3.1 and 4.1 were chosen.

Table 6.1: Sequence recognition for endurance run parameters of the IWT

Parameter	Value	Unit
Tolerance of lower turning point	0.20	°
Minimum sequence length	20	Cycles
Minimum double amplitude	0.05	°
Maximum double amplitude	1	°
Maximum allowable pause time	10	s

The limits for the sequence recognition of pattern 1 are a compromise between the current state of knowledge and the available test time. For pattern 1, the results of the scaled sequences tests indicate that any sequence with 30 or more cycles can be harmful to the raceway in the long run. According to the same test results, any sequence below 10 full cycles should not be harmful, but proof of this for real pitch bearings does not exist yet. Sequences of 30 cycles do not exist in the simulation data of the IWT, whereas there are abundant sequences of 10 to 20 cycles. Including those into the test profile was not possible due to the above mentioned time restrictions. For the parameters of Table 6.1, the following Figures 6.1, 6.2, and 6.3 show these

sequences. Table 6.2 lists their properties. *Seq. ID* is a counter for the recognized sequences of pattern 1. *Full Cycle Count* refers to the number of cycles in the sequence. The column *Multiplier* contains multiplication values for the entire turbine lifetime. These multipliers are a result of the aero-elastic load simulation. The first sequence is repeated 11308 times. All multiplied sequences have a total duration of 84.4 days.

Table 6.2: Pattern 1 sequences for IWT wear test

Seq. ID	Mean Double Amp	Mean Frequency	Full Cycle Count	Duration	Multiplier
-	°	Hz	-	s	-
1	0.43	0.24	26	241.80	11308
2	0.49	0.22	22.5	238.60	11308
3	0.52	0.28	22	163.00	11416

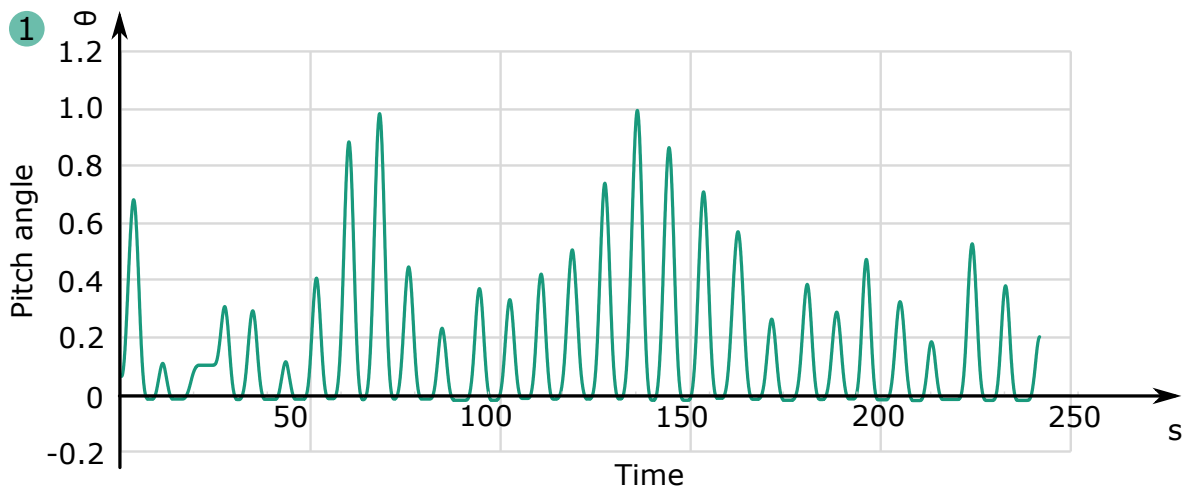


Figure 6.1: Visualization of sequence ID 1 for IWT wear test

The limit for pattern 3 (15°) is about two times the travel of the successful protection run of test ID 11 in Section 4.4. This test (ID11) resulted in some visible damage on the raceway, but this damage was significantly reduced in comparison to the reference test without protection runs. The tests with type 7220 bearings have shown a high influence of the protection run travel on its effectiveness, and the author reasoned that a 15° travel results in an effective protection run with a very high probability. The recognized pattern 3 occurrences are not limited at a travel of 15° , but use the longest travel recognized in the simulation files.

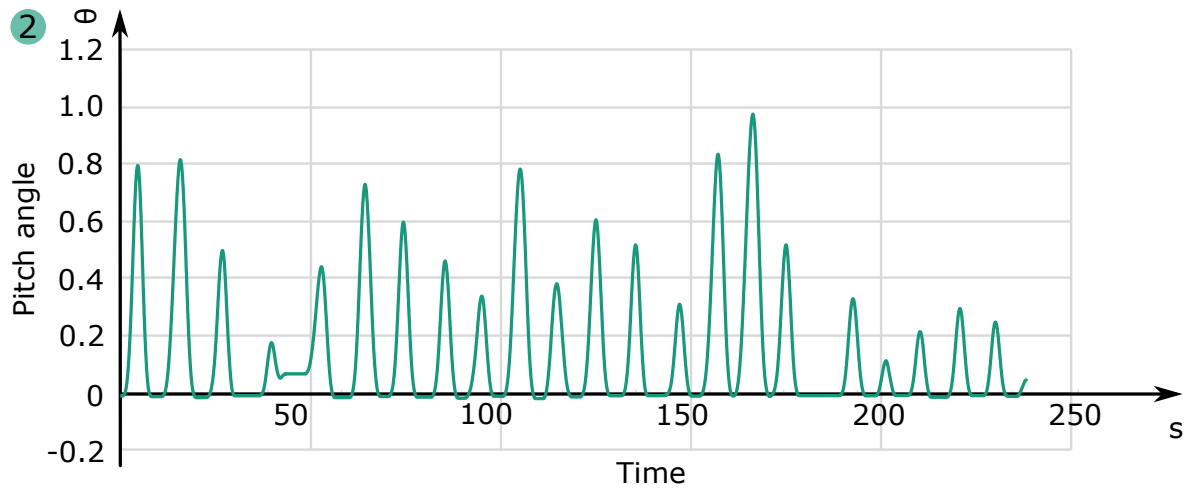


Figure 6.2: Visualization of sequence ID 2 for IWT wear test

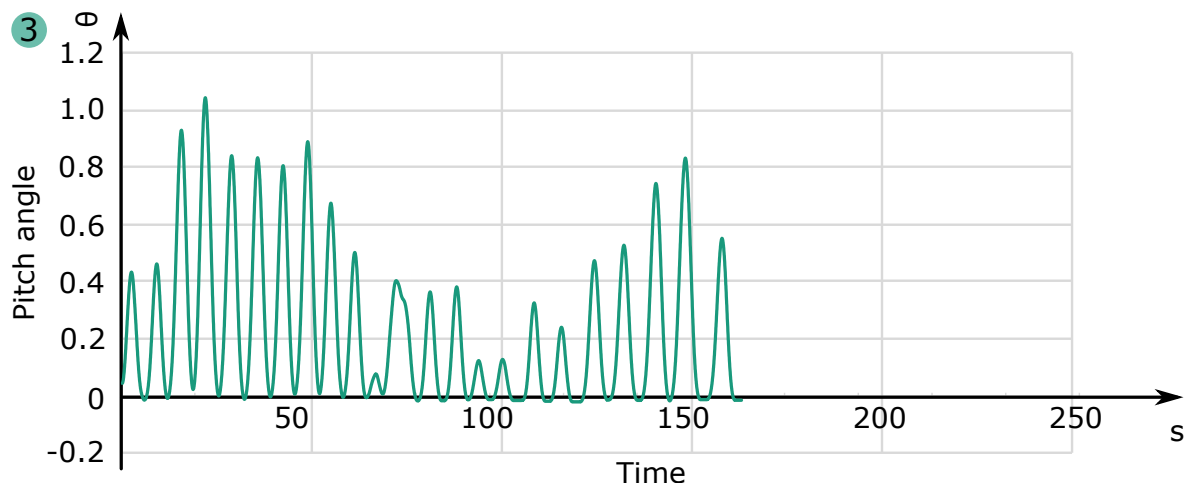


Figure 6.3: Visualization of sequence ID 3 for IWT wear test

As an additional rule for the integration of pattern 3 into the test run, one pattern 3 occurrences may not follow directly after each other. The formation of tribolayers is limited to conditions where the tribochemical reactions can develop on the raceway surface. Once there are effective tribolayers, these conditions are not given, as the surface get less reactive. As such, the execution more than one protection run in a row does not provide additional protection to the raceways. This in turn reduces the final number of pattern 3 occurrences. As the order of the sequences is defined later, the number of protection runs has to be found in an iterative process. Again, this number can also be a result of a compromise between test accuracy and available time. Table 6.3 lists the type 3 sequences for the IWT. The multipliers are lower than the ones for the type 1

sequences, as these movements generally occur at higher wind speeds. Figure 6.4 shows the first three of these sequences. The overall duration of these sequences is 42.3 days, but as some of them are dropped in the test program creation (if they follow other pattern 3 occurrences), the time sum of the later test program is smaller than the sum of the sequences.

Table 6.3: Type 3 sequences for IWT wear test

Sequence ID	Duration	Multiplier	Sequence ID	Duration	Multiplier
-	sec	-	-	sec	-
4	192.15	3404	19	516.65	1032
5	354.05	51	20	393.60	21
6	434.25	23	21	76.65	30
7	262.65	503	22	319.65	21
8	459.95	30	23	106.70	1958
9	108.25	1958	24	295.85	1958
10	68.10	51	25	110.50	30
11	130.90	23	26	177.15	1958
12	349.00	231	27	468.90	51
13	436.75	30	28	428.30	231
14	110.25	30	29	344.45	51
15	350.95	21	30	416.45	23
16	261.35	23	31	342.35	1032
17	78.90	3404	32	432.40	21
18	295.25	30	33	351.75	51

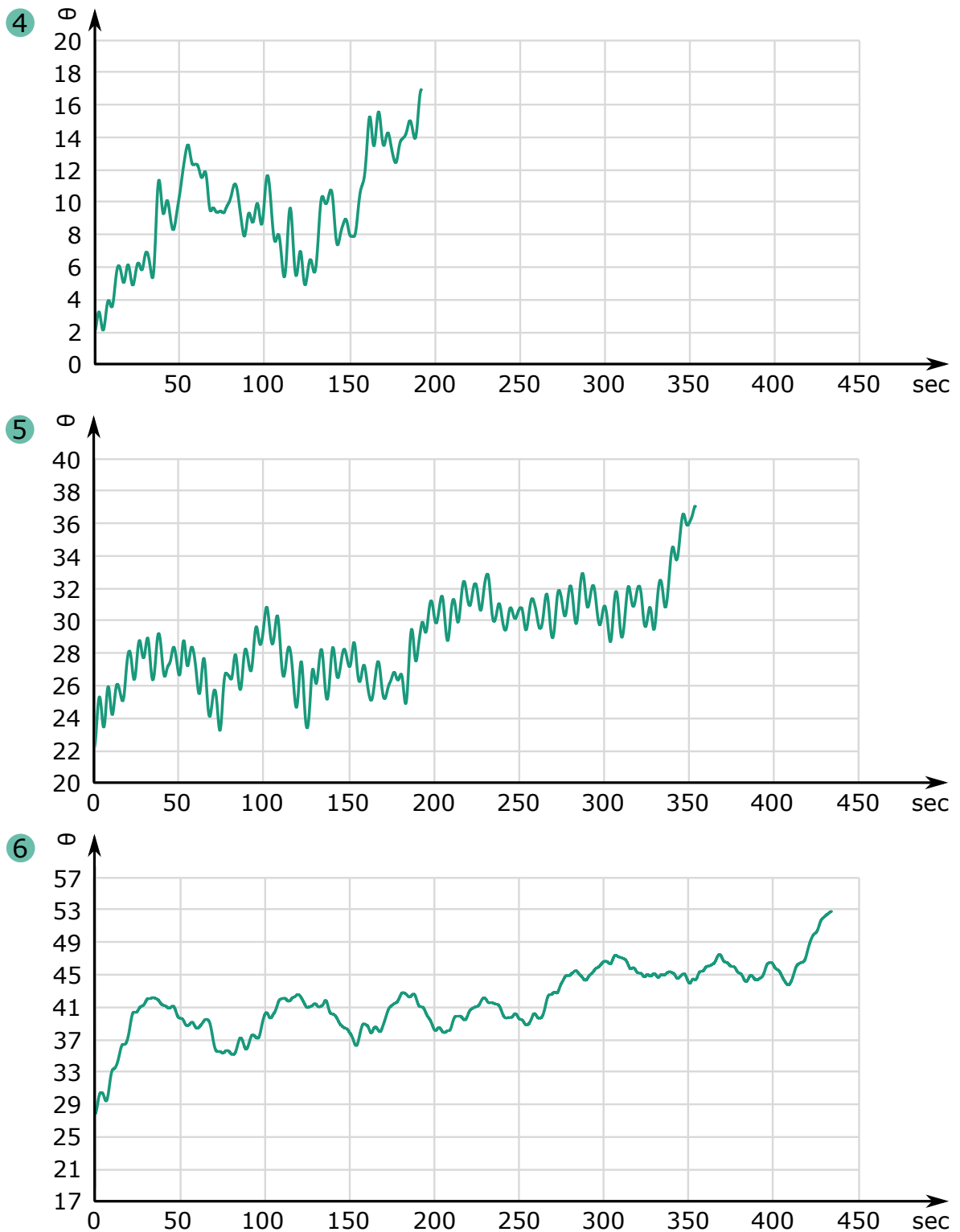


Figure 6.4: Visualization of sequence IDs 4,5 and 6 for IWT wear test

Figure 6.5 shows a comparison of the lifetime cycle count and the cycle count of the test run. The number of cycles is significantly reduced, as one would expect.

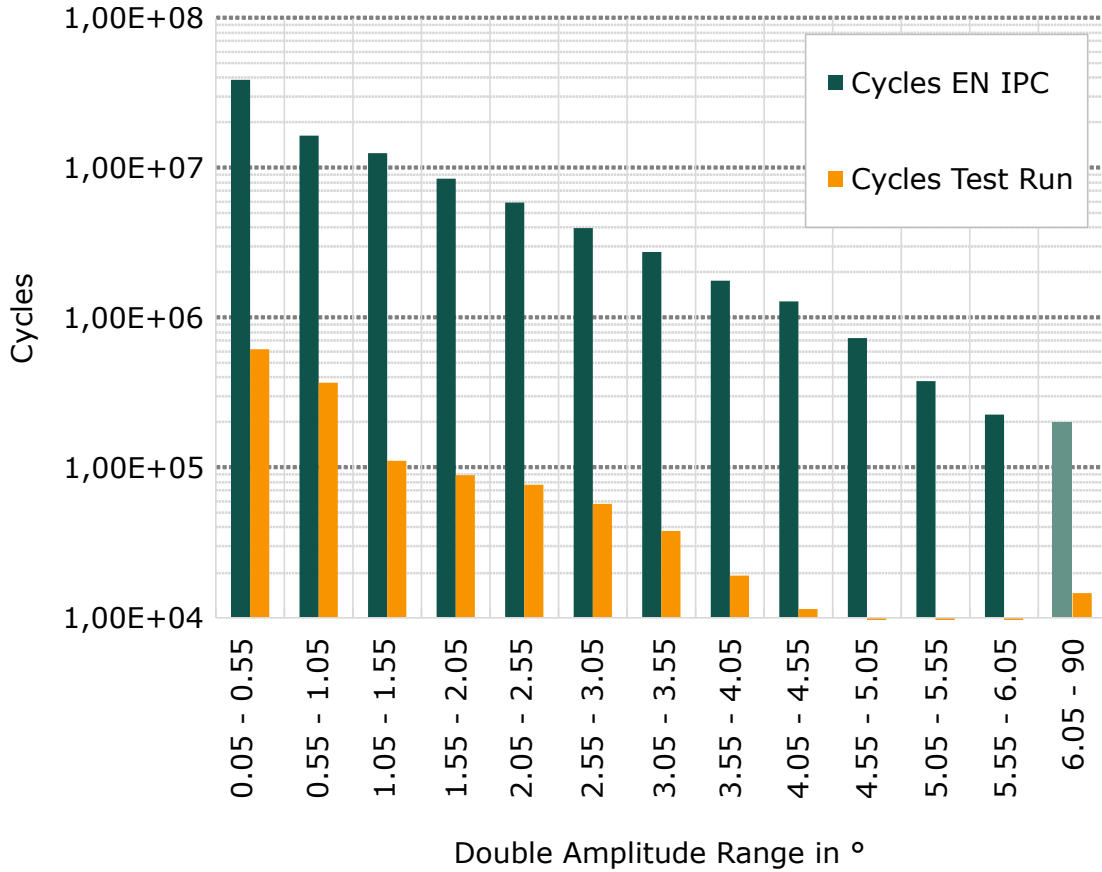


Figure 6.5: Cycles of IWT lifetime simulation and wear profile cycles

6.2 Wear Profile Composition

The sequence recognition and manual selection of pattern 2 occurrences returned a list of sequences that are to be part of the test profile. These sequences need to be brought into an order, and the transitions between the sequences have to be created.

Each sequence consists of the pitch angle θ and the load components M_x , M_y , M_z , F_x , F_y , and F_z .

Each sequence is connected to one file ID of the simulation files. One simulation file can contain more than one sequence. With the list of sequences, the MATLAB program creates a list of simulation files, where each ID is repeated according to the multiplier value. This list is put into an order for the final test run, and the program provides two possibilities to do so:

- Random order
- Order the mean value of a signal according to a target function for one year of turbine lifetime

The first option is simple and straightforward to implement, the latter option tries to make the simulation run more realistic. A signal for such a target function can be the wind speed. Over the course of a year, average wind speeds in Europe are usually higher in winter and lower in summer. [1] Figure 6.6 shows example normalized values (orange circles) for each month of a year and a polynomial fit (green curve).

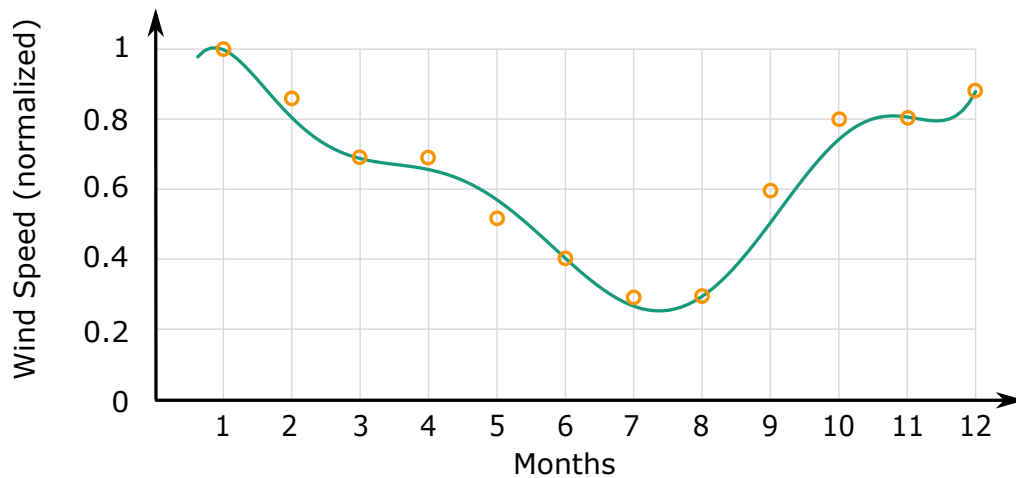


Figure 6.6: Average wind speed over a year

The program allows to introduce such a distribution for any signal. Possible signals that reflect the changes in wind speed are obviously the measured wind speed at hub height, but if this is not available it is reasonable to use the power output of the turbine instead. Equation (6.1) describes the polynomial fit of Figure 6.6). In this example t is given in months, and $f(t)$ is the normalized wind speed.

$$f(t) = -0.0013 \cdot t^6 + 0.023 \cdot t^5 - 0.2107 \cdot t^4 + 1.0453 \cdot t^3 - 2.7532 \cdot t^2 + 3.3609 \cdot t - 0.4636 \quad (6.1)$$

The target signal values of the simulation sequences that make up the test run are normalized and split into bins as well. Table 6.4 lists the hours spent in bins for target function and sequences, each for one year of turbine operation. The sequences that make up the test run do not necessarily have the same time spent in the bins as the target function.

Yet it is mandatory to keep the sequences, so the bins of the target functions have to be adapted in order to have enough time for the sequences. The result is a deformed target function, which does not respect the time share of the original target function, but the sequence of values. Figure 6.7

Table 6.4: Duration distribution of wind speed for target function and simulation sequences

Normalized Speed	Hours in Bin (Target)	Hours in Bin (Sequences)	Sequence ID(s)
0.90 – 1.00	355	49	6, 11, 14, 15, 16, 20, 21, 22, 25, 30
0.80 – 0.90	1639	94	5, 8, 10, 13, 18, 27, 29, 33
0.70 – 0.80	1084	0	
0.60 – 0.70	1723	248	7, 12, 28
0.50 – 0.60	778	1165	19, 24, 31
0.40 – 0.50	704	1343	4, 9, 17, 23, 26
0.30 – 0.40	830	0	
0.20 – 0.30	1167	1478	3
0.10 – 0.20	0	4316	1, 2
0.00 – 0.10	0	0	

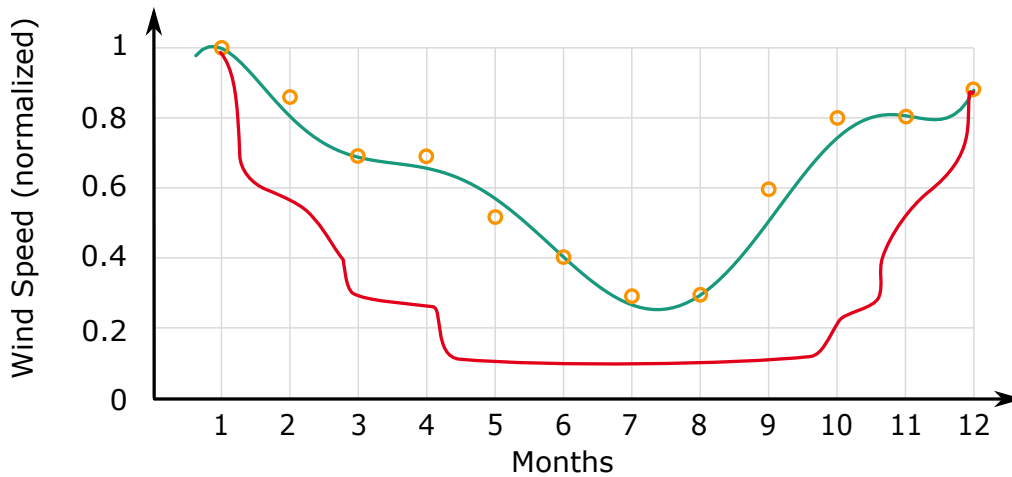


Figure 6.7: Deformation of target function to match spent times of sequences

visualizes this transformation, the deformed target function is shown in red. This deformed target function is again split into discrete bins of the function values, but this time the split takes account of the sequence of values. The process is designed as a sequential process, and each change of the function across bin borders assigns a new position ID (see Figure 6.8).

With the positions IDs and the adapted duration, the algorithm now assigns sequences to position IDs until the time spent in the positions ID is filled. The sequences are drawn from a sequence repository, each element is only assigned once. If there is more than one sequence within the same bin, they are randomly chosen at each step and added to the position ID. In such a case the

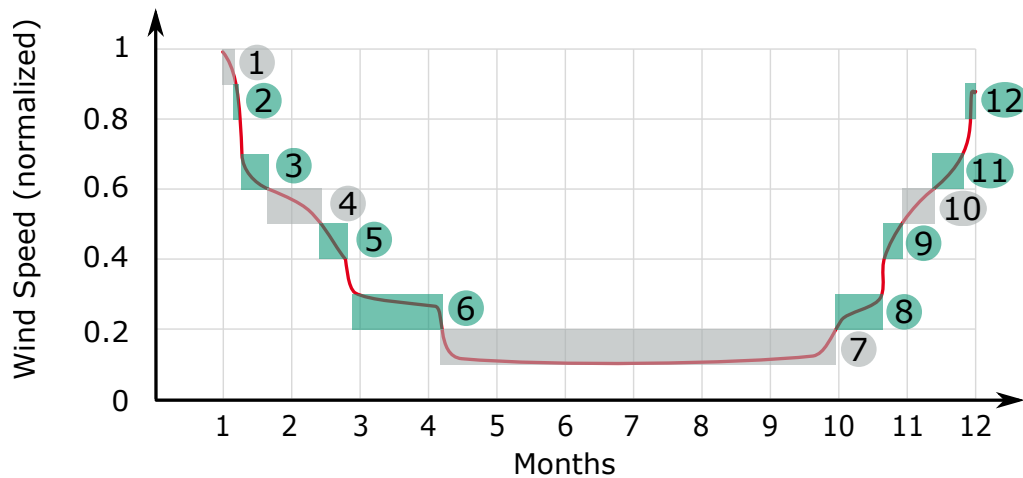


Figure 6.8: Assignment of positions IDs

duration is not necessarily matched for each position ID. The algorithm accepts overlong position IDs unless there is no sequence with a bin left. In the end, all sequences are in an order that corresponds to the order of the target function. In the example, position ID 4 and 10 are in the speed bin of 0.5 to 0.6, and so are the sequences 19, 24, and 31. Position ID 4 is randomly filled with sequences 19, 24, and 31, until the duration is matched or exceeded. If it is exceeded, the duration of positions ID 10 will be slightly reduced in turn.

In case of IWT, the order of the sequences is randomly set. To have a target function of high value for the test program would mean to have either long-term power output data of the turbine or long-term wind speed measurements on an IEC class 1A site.

At this point, the sequences for the test program and their order are set. The end values for θ and the loads of one sequence do not necessarily match the start values of the next sequence, there is always a gap. The transitions between these values need time which adds to the overall test time, see Figure 6.9. While it is possible to use simple transfers like ramps, the author thought it worthwhile to take transitions from the input data. The idea behind this is to use the time that has to be spent for transitions with more realistic data and, by this, add additional value to the test.

The algorithm defines a transition database (designated Transfer Time Series Repository, TTSR) which contains positive and negative transitions for each signal. The longest transition is the longest delta in the simulation data. For the pitch angle θ , this is typically a value of about 90° . In addition to this value, it searches for transitions of 5, 10 and 15% length of the longest value. The reason to add this smaller values is that in most cases shorter transitions show a different behavior (slope) than longer transitions. Table 6.5 shows the positive transition deltas for the IWT.

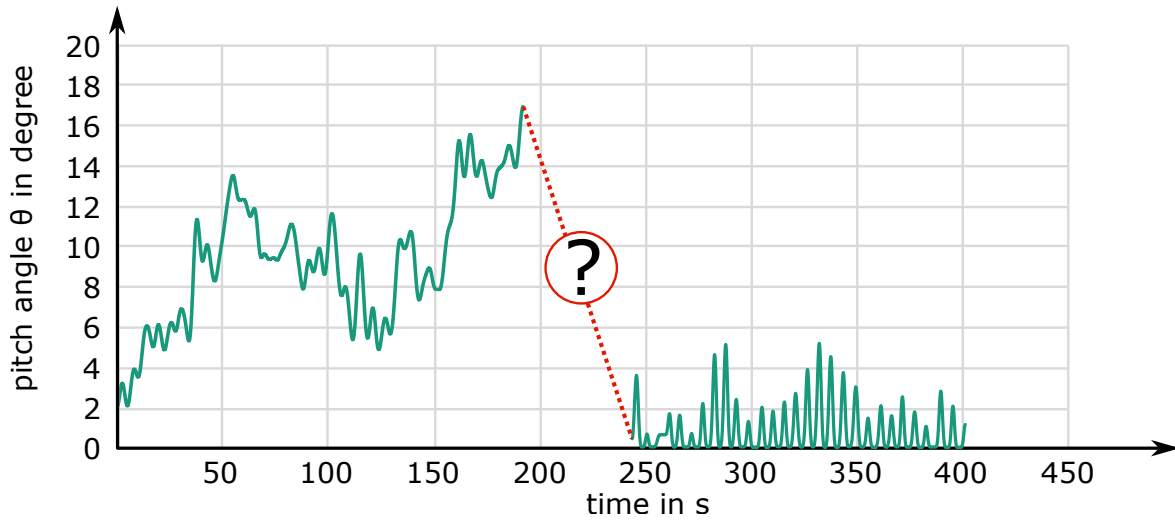


Figure 6.9: Transition time between sequences

Table 6.5: Positive transition values in TTSR of IWT

θ °	F_x kN	F_y kN	F_z kN	M_x kNm	M_y kNm	M_z kNm
4.0	23.7	60.3	47.5	1083.8	884.7	18.7
8.2	52.3	99.6	109.1	2363.1	1906.9	49.8
-	70.2	117.5	172.2	3132.6	3037.1	64.3
90.0	485.9	834.1	1180.7	20256.7	20669.2	449.2

Figure 6.10 visualizes the time series for the pitch angle θ and bending moment (M_y) transitions. Within the time series, the algorithm could not find a 12°-transition of θ , therefore this field is empty in Table 6.5 and Figure 6.10.

With the ordered list of sequences, the algorithm starts to stitch time series for the test run. Any transition is filled with data from the TTSR, this is done individually for each signal. In case a necessary transition is longer than the longest available transition, the transition slope is stretched to match the needed delta. In case the needed transition is shorter than the longest available transition in the database, the next longer transition is cut at the target delta. As the time for the transitions can be different for each channel, the channels that finish their transition wait at the last value until all transitions are finished.

The slope of the transition does not necessarily match the slope of the prior or following sequence. Such cases cause unrealistically high load or pitch dynamics. As a countermeasure, the algorithm applies a low pass filter to a fixed sample length before and after each transition start and end.

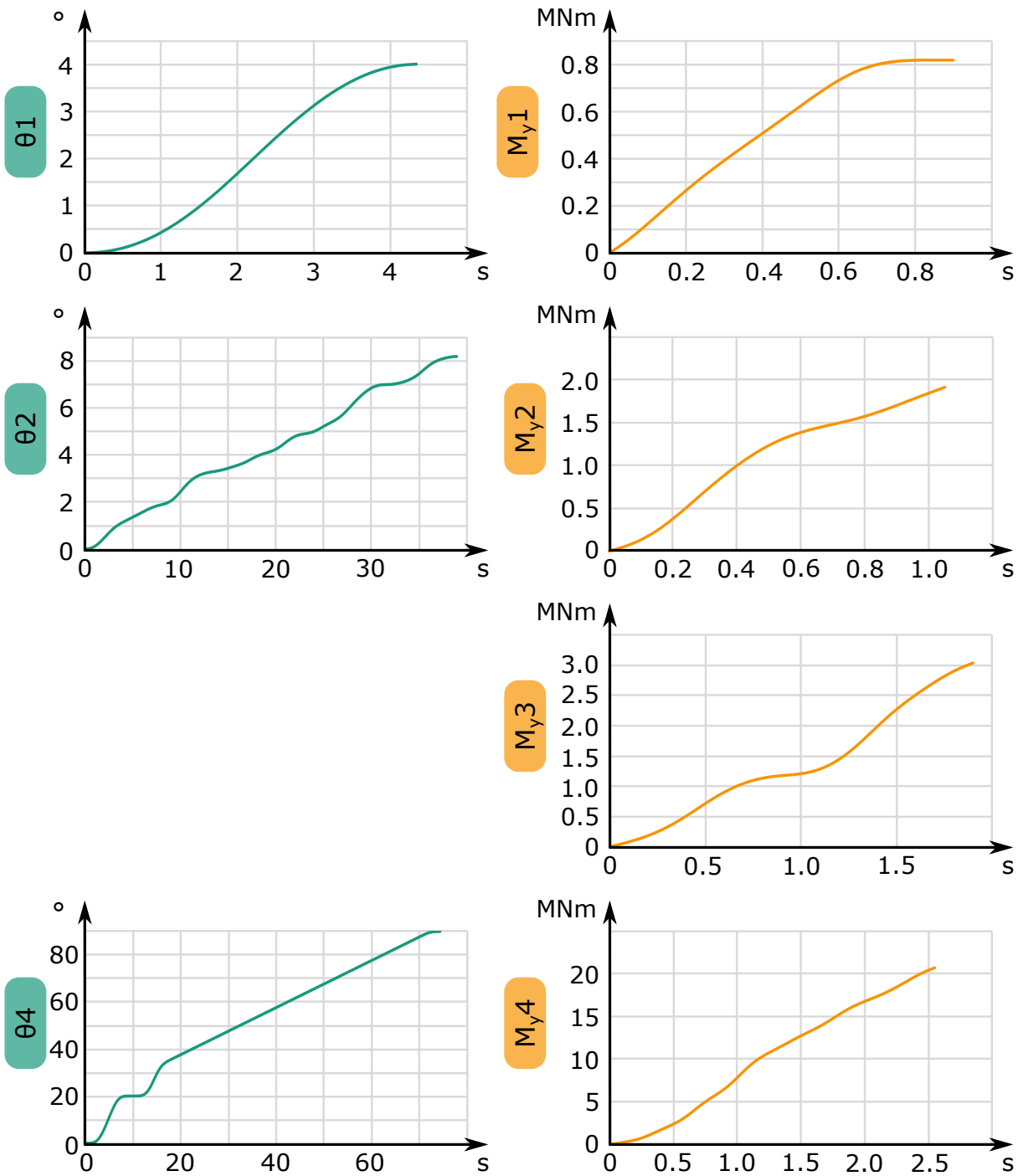


Figure 6.10: TTSR positive time series for θ and M_y

The algorithm has the possibility to force the execution of complete simulation files at a given frequency. In case of the IWT, a simulation file of a turbine start at cut-in wind speed (3 m/s) is executed with the start of each test day, and a simulation of a turbine stop from 12 m/s is executed at the end of each test day. Real wind turbines have numerous starts and stops over the course of a year. These type 2 movements are effectively protection runs for the bearings. The daily execution in the test does suffice to replicate the influence of these situations, as the type 3 movements occur frequently throughout the test profile as well.

Figure 6.11 shows the time series of the pitch angle for the first test day. The periods with small θ -values below 5° contain pattern 1 sequences, the periods with higher pitch angle variations those of pattern 3. At the beginning and the end θ reaches values of 90° , these are the start and stop time series (movement pattern 2).

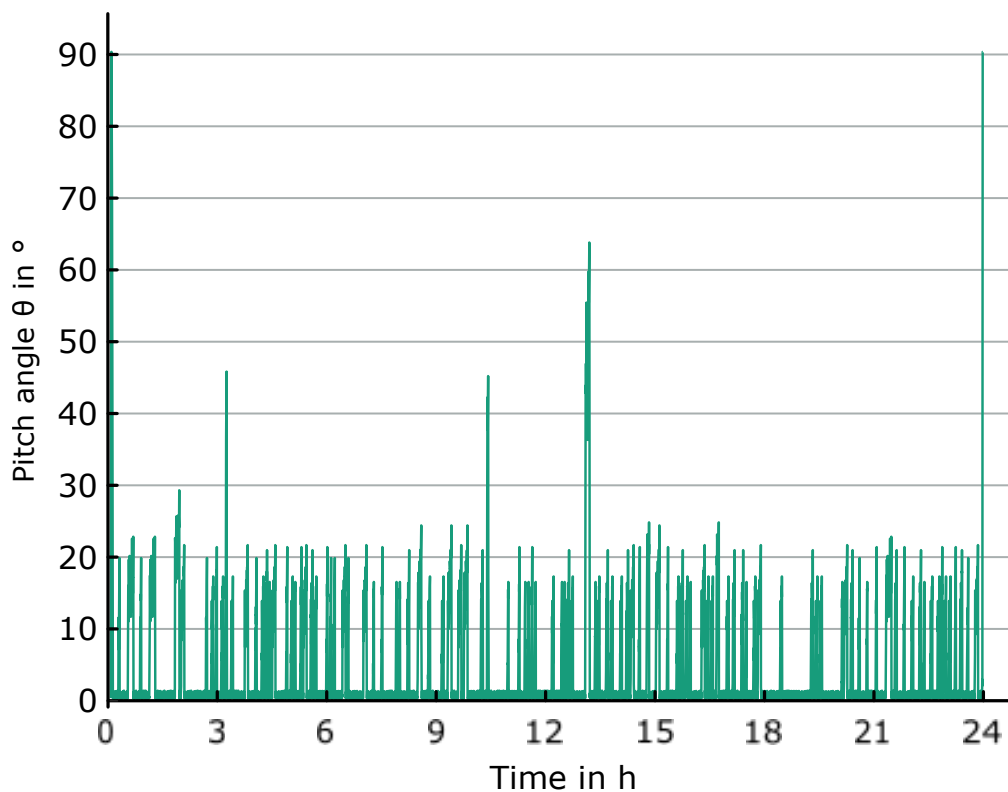


Figure 6.11: Wear endurance run IWT: Pitch angle of day 1

The test run time series are split at a maximum length of 24 hours. This is a technical restriction of the test rig main controller, and it is also handy for daily visual inspections and similar tasks at the test rig. Since the algorithm cannot know the length of the transition before calculating the time series, it adds elements to the time series until its duration is longer than 24 hours and then removes the last elements, until the duration fits the limits.

The wear test run for the IWT has a duration of 5.86 days or 140.5 hours for one year of turbine lifetime. The overall duration is 117.1 days. This duration is lower than the duration of all input sequences, as the execution of protection runs is limited to one at a time, and serial execution is prohibited in the final test program (see Section 6.1).

6.3 Rolling Contact Fatigue Profile

In Section 2.4 on damage modes, we introduced rolling contact fatigue. Although the calculation methods need further development for oscillating applications, the damage mode itself allows to set up an accelerated run by altering the load and speed.

Input for such an alteration is a simplified cycle counting and bin counting of the loads. In case of the IWT, the algorithm is set to respect any movement between 0.05° and 90° , and to read out the mean values of the pitch speed and all force components (F_x , F_y , and F_z). The travel of all oscillations is converted into larger movements (to make sure the later run does not trigger wear damage modes) of about 25° double amplitude. Table 6.6 shows these values for the IWT. The initial cycle count of 61.07 million cycles of 1.18° equals 2.88 million cycles of 25° .

Table 6.6: RCF run input parameters, cycle count

Parameter	Value	Unit
Cycle count	61.07	Million Cycles
Mean double amplitude	1.18	$^\circ$
Mean absolute pitch speed	0.51	$^\circ/\text{s}$
Mean radial force in x	267.61	kN
Mean radial force in y	-35.37	kN
Mean combined radial force F_r	269.94	kN
Mean axial force in z	596.06	kN

The resulting bending moment M_{res} is the dominating load component, and a simple mean value calculation would underestimate the equivalent bearing load P_a – and thanks to the exponent p of 3, it would heavily overestimate the resulting lifetime. Hence, the algorithm executes a bin counting for M_{res} . In this case, the bins are set to 5 MNm width each, and the upper border of the bin is taken as the later input load value for the P_a calculation. To perfectly understand the relation between M_{res} and P_a , one would need to execute several FE simulations of a full rotor star and build empirical functions that describe $P_a(M_{res})$. In case of the IWT, the scope of the project did not include such calculations, and the RCF runs are not part of the project either. For the sake of an exemplary run design, we can use an approximate function for P_a . One of those is part of the *NREL Design Guideline 03* [9], see Equation (6.2). F_r refers to the combined radial load. Unfortunately, this equation heavily underestimates P_a in relation to M_{res} , as Menck showed

clearly in [106]. Menck compared the results of Equation (6.2) with the factor 2 for the bending moment with a P_a based in FE-calculated load distribution and found significant deviations. He found a factor of 3.2 to be more suitable for the task. This factor transforms Equation (6.2) into Equation (6.3). Table 6.7 lists the bins for the resulting bending moment, the related P_a according to Equation (6.3) and the time spent in those bins. For P_a , the mean radial and axial forces are taken into account.

$$P_a = 0.75F_r + F_z + \frac{2M_{res}}{d_m} \quad (6.2)$$

$$P_a = 0.75F_r + F_z + \frac{3.2M_{res}}{d_m} \quad (6.3)$$

Table 6.7: RCF run input parameters, M_{res} bin count

M_{res} kNm	P_a kN	Time spent in bin T_{bin} h
5000	4210.03	2023.15
10000	7621.54	27435.58
15000	11033.06	52672.37
20000	14444.57	38839.41
25000	17856.08	1004.14

With the results of this bin counting, the maximum permissible bending moment of the BEAT6.1 test rig (50 MNm), and the basic lifetime equation from Section 2.4, the P_a bins can now be converted into one final P_a . As the test rigs geometry makes it easier to reach 50 MNm with a combined radial load of 300 kN, Equation (6.4) yields a P_a of 34340 kN.

$$P_{a_{max}} = 0.75 \cdot 300 + \frac{3.2 \cdot 50000}{4.69} \quad (6.4)$$

Reordering Equation (2.12) from the section on RCF damage to get the time T_{test} that has to be spent if the load of each bin is raised to $P_{a_{max}}$:

$$T_{test} = T_{bin} \cdot \left(\frac{P_a}{P_{a_{max}}} \right)^3 \quad (6.5)$$

The sum of all individual T_{test} are 5082.3 hours. To further accelerate the test run, the pitch seed is set to the maximum value of the pitch drive ($6^\circ/s$), which in relation to the mean pitch speed from Table 6.6 gives a multiplier of 5.087. The resulting test time are 999.53 hours. As the cycles

are pure ramps, it is reasonable to smoothen the turning points to avoid damage of the pitch drive. This adds another 0.6 seconds per cycle, so the final test time are 1479.5 hours or 61.64 days.

To avoid any risk of wear damage, it is reasonable to shift the turning points of the large oscillation with every cycle. This can be done by adding a slower sine function to the ramp cycles. Figure 6.12 shows an overview of a 2-hour-profile, Figure 6.13 shows the first minute of this profile.

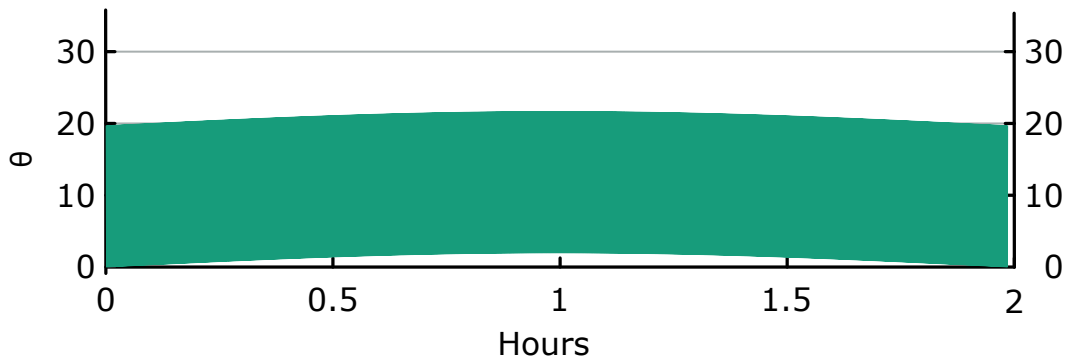


Figure 6.12: Fatigue endurance run, pitch-angle profile overview

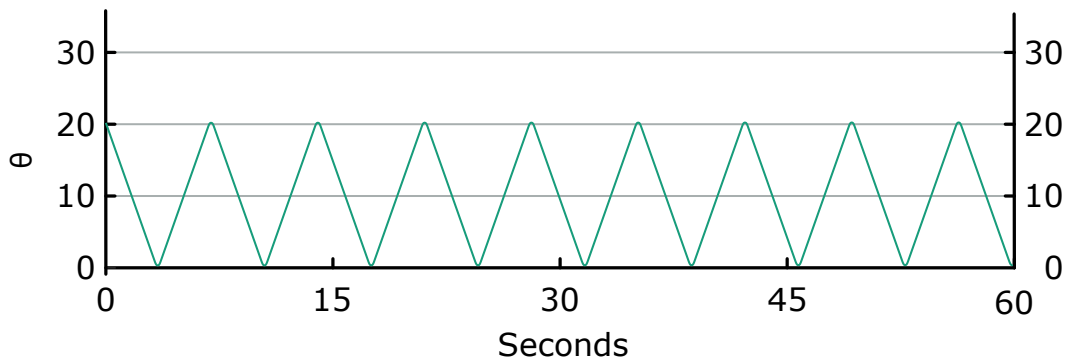


Figure 6.13: Fatigue endurance run, pitch-angle profile detail

Chapter 7

Conclusions and Outlook

The objective of this thesis was to develop an accelerated endurance run program for pitch bearings. Pitch bearings connect the rotor blade and the rotor hub of a wind turbine. They allow pitch movements of the blades. These movements control aerodynamic loads. Pitch control is the state of the art control and primary safety mechanism of wind turbines. The incoming, ever-turbulent wind causes stochastic, dynamic loads in six degree of freedom, and the pitch control demands oscillating movements of the bearings. The interfaces have a limited and inhomogeneous stiffness along their circumference. Dynamic loads, oscillating movements and complex interfaces form a set of requirements unique to pitch bearings.

The possible damage modes of pitch bearings are manifold, but most of them can be handled with existing models and calculation methods. Of the remaining, raceway wear is one that cannot be calculated at all. As the understanding of this damage mode is limited, and for the objective of having a true acceptance run, the two basic requirements for the test environment were defined. It has to apply realistic dynamic loads and it has to have realistic interfaces to the pitch bearing. The criteria to evaluate the interface parts that represent hub and blade is the internal load distribution of the bearing.

Obtaining internal load distributions from outer loads of pitch bearings needs finite-element simulations of full rotors. The methods for such simulations are not completely standardized, and this work contributes to the aspect of contact angle calculation.

Data analysis of time series is necessary to process the vast amounts of data that result from aero-elastic simulations. In this work, the author develops an algorithm to analyze sequences of pitch bearing movements and classified those movements into harmful and beneficiary patterns. The knowledge about beneficiary movements was very limited prior this work, and the scaled sequence test in combination with reference tests of full scale pitch bearings add substantial findings to this field. The scaled sequence test shows that larger movements embedded in harmful, small oscillations, can protect the raceway. This protection happens through the formation of tribolayers on the surface. For such a formation, time, energy and presence of lubricant are necessary. A lubricant film that separates the rolling partners is not.

With the example of the IWT7.5-164 reference turbine and having in mind larger bearing sizes for any future projects, the test environment BEAT6.1 is specified. This rig is a hexapod design with a maximum bending moment of 50 MNm. It has dedicated interface parts that emulate the specific

behavior of hub and blade. For the hub, this is the stiffness variation along the circumference of the bearing flanges that is emulated by a double-ring Hub Adapter. For the blade, ovalization, axial load distribution and bolt interfaces are the key requirements for an emulation part. The hybrid Force Transmitting Element made of two glass-fiber reinforced plastic tubes with steel segments in the center matches these requirements.

The final test program should be able to allow a profound risk assessment prior to mounting the bearing into a turbine. Such a program is called an acceptance test. It allows the responsible design engineer to make a statement about the ability of the bearing to withstand operating conditions. This objective is accomplished. Within this work, the requirements for both a test run and a test environment for pitch bearings are defined. Based on the results of the data analysis and the scaled sequence tests, the author develops a work flow to derive time series for the wear part of an acceptance run. The BEAT6.1 ran these time series on two four-point contact ball bearings and will run it on other bearing types with the same diameter. The full wear run profile has a duration of approximately 117 days. The author developed a program of a rolling contact fatigue test as well, but the execution of this profile is outside of the scope of this work.

There is still a lot of room for future research. This could for example cover the following tasks:

- Broaden the understanding of influence of sequences on wear
- Further understand scaling of tests
- Develop new approaches for interface emulations
- Develop empirical models for wear occurrence and progression

Some of those tasks are and will be part of ongoing and future projects at the Large Bearing Laboratory of Fraunhofer IWES.

References

- [1] Erich Hau. *Windkraftanlagen: Grundlagen. Technik. Einsatz. Wirtschaftlichkeit*. Springer Berlin Heidelberg, Berlin, Heidelberg, sixth edition, 2017.
- [2] Tony Burton. *Wind Energy Handbook*. Wiley, Chichester and New York, second edition, 2011.
- [3] Robert Gasch. *Windkraftanlagen: Grundlagen, Entwurf, Planung und Betrieb*. Studium. Vieweg + Teubner, Wiesbaden, seventh edition, 2011.
- [4] Matthias Stammler, Andreas Reuter, and Gerhard Poll. Cycle counting of roller bearing oscillations – case study of wind turbine individual pitching system. *Renewable Energy Focus*, 25:40–47, 2018.
- [5] F. Schwack, M. Stammler, H. Flory, and G. Poll. Free contact angles in pitch bearings and their impact on contact and stress conditions. *WindEurope Conference, Hamburg*, 2016.
- [6] Matthias Stammler, Sebastian Baust, Andreas Reuter, and Gerhard Poll. Load distribution in a roller-type rotor blade bearing. *Journal of Physics: Conference Series*, 1037, 2018.
- [7] Matthias Stammler and Gerhard Poll. Schadensmechanismen in Rotorblattlagern. GfT-Reibung, Schmierung und Verschleiss, Göttingen, 2014.
- [8] Matthias Stammler and Andreas Reuter. Blade bearings: Damage mechanisms and test strategies. Conference for Wind Power Drives, Aachen, 3/4/2015.
- [9] T. Harris, J. H. Rumbarger, and C. P. Butterfield. *Wind Turbine Design Guideline DG03: Yaw and Pitch Rolling Bearing Life*. Golden, Colorado, 2009.
- [10] F. Schwack, M. Stammler, G. Poll, and A. Reuter. Comparison of life calculations for oscillating bearings considering individual pitch control in wind turbines. *Journal of Physics: Conference Series*, 753, 2016.
- [11] DNVGL-ST-0438. Control and protection systems for wind turbines. Guideline, DNV GL, 2016.
- [12] David Weston. Most turbine models fail to make a profit. <https://www.windpowermonthly.com/article/1525529/turbine-models-fail-profit>, 2019. Online; accessed August 19 2019.
- [13] E. A. Bossanyi. Individual blade pitch control for load reduction. *Wind Energy*, 6(2):119–128, 2003.

- [14] Bert Verdyck, Kris Smolders, and Michiel van den Donker. Advanced test program to increase reliability and reduce time-to-market for new MMW wind turbine gearbox designs. International Conference on Gears, München, 2013. VDI Verlag.
- [15] Shanghai Oujikete. Fatigue test of pitch bearing (033.50.2410) for 2.5mw/3mw wind turbines under full loads completed. <https://tinyurl.com/so43um7>, 2012. Online; accessed September 23 2013.
- [16] R. K. Pachauri and Leo Mayer, editors. *Climate change 2014: Synthesis report*. Intergovernmental Panel on Climate Change, Geneva, Switzerland, 2015.
- [17] Earth overshoot day 2019: Ressourcenbudget verbraucht. <https://tinyurl.com/tzneb3k>, 2019. Online; accessed August 11 2019.
- [18] Munich Re. *Ein Jahr der Stürme*. München, 2018.
- [19] Marcus Jauer. Bis sie versinken. *Die Zeit*, 2019(25/2019), June 13 2019.
- [20] MIDEM. *Jahresbericht 2018: Migration und Populismus*. Dresden, 2018.
- [21] Manfred Kriener. Die Kraft aus der Luft: Geschichte der Windenergie. <http://www.zeit.de/2012/06/Windkraft>, 2012. Online, accessed June 5 2013.
- [22] John K. Kaldellis and D. Zafirakis. The wind energy (r)evolution: A short review of a long history. *Renewable Energy*, 36(7):1887–1901, 2011.
- [23] Michael McGovern. Wind was spain's cheapest power. <https://www.windpowermonthly.com/article/1378082/wind-spains-cheapest-power>, 2016. Online, accessed April 25 2016.
- [24] The International Renewable Energy Agency. Renewable power generation costs in 2018. 2019.
- [25] Craig Richard. Vattenfall wins second subsidy-free dutch tender. <https://tinyurl.com/sgsb66n>, 2019. Online; accessed August 19 2019.
- [26] Energiedaten: Gesamtausgabe: Stand: August 2018. <https://tinyurl.com/ycqz8c5a>, 2018. Online, accessed October 27 2019.
- [27] Cerstin Gammelin. Oettinger schön Subventionsbericht. <https://tinyurl.com/ktgx7m6>, 2013. Online; accessed October 25 2019.
- [28] Peter Jamieson. *Innovation in wind turbine design*. Wiley, Hoboken, N.J, first edition, 2011.
- [29] Fraunhofer IEE. *Windenergie Report Deutschland 2018*. Fraunhofer Verlag, Stuttgart, 2018.
- [30] GE announces Haliade-X, the world's most powerful offshore wind turbine. <https://tinyurl.com/v3cpzja>, 2018. Online; accessed August 11 2019.

-
- [31] L. Fingersh, M. Hand, and A. S. Laxson. *Wind Turbine Design Cost and Scaling Model*. National Renewable Energy Laboratory, Golden, Colorado, 2006.
- [32] IEC 61400-1 third edition. Wind turbines - part 1: Design requirements. Standard, IEC, Geneva, 2005.
- [33] A. D. Garrad and U. Hassan. Taking the guesswork out of wind turbine design. In *Proceedings: Wind Energy Expo '86, Cambridge, USA*, pages 164–176, 1986.
- [34] M. Matsuishi and T. Endo. Fatigue of metals subjected to varying stress. Japan Society of Mechanical Engineers, Fukuoka, Japan, 1968.
- [35] H. B. Hendriks and B. H. Bulder. *Fatigue Equivalent Load Cycle Method: A General Method to Compare the Fatigue Loading of Different Load Spectrums*. ECN, 1995.
- [36] Torben Juul Larsen, Helge A. Madsen, and Kenneth Thomsen. Active load reduction using individual pitch, based on local blade flow measurements. *Wind Energy*, 8(1):67–80, 2005.
- [37] C. L. Bottasso, A. Croce, C. E. D. Riboldi, and M. Salvetti. Cyclic pitch control for the reduction of ultimate loads on wind turbines. *Journal of Physics: Conference Series*, 524:12063, 2014.
- [38] Panagiotis Panousis, Li Qiang, and Ou Fashun. Individual pitch control system on-field test. China Wind Power, Beijing, October 24 2014.
- [39] J. Jonkman, Butterfield S., W. Musial, and G. Scott. *Definition of a 5-MW Reference Wind Turbine for Offshore System Development*. National Renewable Energy Laboratory, Golden, Colorado, 2009.
- [40] Bak et al. Description of the dtu 10 mw reference wind turbine. <http://dtu-10mw-rwt.vindenergi.dtu.dk>, 2013. Online; accessed August 15 2018.
- [41] O. Bleich, F. Meng, E. Daniele, P. Thomas, and W. Popko. IWES Wind Turbine IWT-7.5-164 rev. 2.5. <https://tinyurl.com/qvzwjox>, 2016. Online; accessed November 7 2017.
- [42] IWES Wind Turbine. <https://tinyurl.com/sna4wrq>, 2018. Online; accessed August 22 2019.
- [43] Matthias Stammer, Philipp Thomas, Andreas Reuter, Fabian Schwack, and Gerhard Poll. Effect of load reduction mechanisms on loads and blade bearing movements of wind turbines. *Wind Energy*, 6(2):119, 2019.
- [44] D. Dowson. *History of Tribology*. Longman Inc., New York, 1979.
- [45] René Goscinny and Albert Uderzo. *Asterix and Cleopatra*. 1969.
- [46] Tedric A. Harris and Michael N. Kotzalas. *Rolling bearing analysis*. CRC, Taylor & Francis, Boca Raton, fifth edition, 2007.

- [47] ABMA bearing timeline. <https://tinyurl.com/ww9bpjm>, 2006. Online, accessed August 6 2013.
- [48] Heinrich Rudolf Hertz. Über die Berührung fester elastischer Körper. *Journal für die reine und angewandte Mathematik*, 92:156–171, 1881.
- [49] Heinrich Rudolf Hertz. Über die Berührung fester elastischer Körper und über die Härte. *Verhandlungen des Vereins zur Beförderung des Gewerbefleißes*, pages 449–463, 1882.
- [50] J. Brändlein, P. Eschmann, and L. Hasbargen. *Die Wälzlagerpraxis - Handbuch für die Berechnung und Gestaltung von Lagerungen*. Vereinigte Fachverlage, Mainz, 3 edition, 1998.
- [51] Luc Houpert. An engineering approach to hertzian contact elasticity—part i. *Journal of Tribology*, 123(3):582, 2001.
- [52] F. Schwack, F. Prigge, and G. Poll. Finite element simulation and experimental analysis of false brinelling and fretting corrosion. *Tribology International*, 126:352–362, 2018.
- [53] Piet M. Lugt. A review on grease lubrication in rolling bearings. *Tribology Transactions*, 52(4):470–480, 2009.
- [54] D. Dowson and P. Ehret. Past, present and future studies in elasto-hydrodynamics. *Proceedings of the Institution of Mechanical Engineers, Part J: Journal of Engineering Tribology*, 213(5):317–333, 1999.
- [55] Taisuke Maruyama and Tsuyoshi Saitoh. Oil film behavior under minute vibrating conditions in EHL point contacts. *Tribology International*, 43(8):1279–1286, 2010.
- [56] Piet M. Lugt, Slavco Velickov, and John H. Tripp. On the chaotic behavior of grease lubrication in rolling bearings. *Tribology Transactions*, 52(5):581–590, 2009.
- [57] Joachim Schulz and Ekkard Brinksmeier. Interactions of anti wear additives with metal surfaces - new findings. *Tribology - industrial and automotive lubrication*, Ostfildern, 2014. Techn. Akad. Esslingen.
- [58] Triboschutzschichtcharakterisierung: Untersuchung zur Bildung, Charakterisierung und Wirkungsweise von Triboschutzschichten. FVA-Forschungsvorhaben 289 I + II, FVA, Frankfurt, 2000.
- [59] Triboschutzschichten II: Zusammenhänge zwischen Zahnrad- und Wälzlagerschäden und tribologischen Veränderungen des oberflächennahen Werkstoffbereichs. FVA-Forschungsvorhaben 289 Ib + IIb, FVA, Frankfurt, 2004.
- [60] Jens Thomsen and Kim Thomsen. Pitch bearing, 2012. European Patent EP 2511 521 A1.
- [61] Michael Jüttner. *Konzeptentwicklung für die Rotorblattlagerung von Windenergieanlagen mit Individual Pitch Control*. Master thesis, Universität Erlangen, Lehrstuhl für Konstruktionstechnik, Erlangen, 2016.

- [62] IMO Holding GmbH. Wälzlageranordnung, 2007. German Patent DE 20 2007 011 577 U1.
- [63] Liebherr. *Großwälzlager: Produktkatalog*. 2016.
- [64] Rothe Erde. *Großwälzlager: Gesamtlieferprogramm*. 2016.
- [65] IMO GmbH & Co. KG. *Produktkatalog Drehverbindungen*. 2013.
- [66] Sebastian Baust. *The Influence of Geometrical and Structural Properties of Wind Turbine Blades on Blade Bearings*. Master thesis, DTU, Kongens Lyngby, 2019.
- [67] Fabian Schwack. *Auslegung Rotornabe der IWES 7,5 MW Referenzanlage*. Project thesis, Leibniz Universität Hannover, Institut für Maschinenkonstruktion und Tribologie, Hannover, 2014.
- [68] Felix Steinkuhl and J. Wenske. Emulation of interface stiffnesses for full scale tests on wind turbine blade bearing. DEWEK 2017, 13th Germany Wind Energy Conference, Bremen, October 18 2017.
- [69] D. Todd Griffith and Thomas D. Ashwill. *The Sandia 100-meter All-glass Baseline Wind Turbine Blade: SNL100-00*. Sandia National Laboratories.
- [70] Juna Bueno Gayo. Reliawind: Project final report. <https://cordis.europa.eu/project/rcn/88411/reporting/en>, 2011. Online; accessed August 15 2018.
- [71] DIN ISO 281. Wälzlager - Dynamische Tragzahlen und nominelle Lebensdauer (ISO 281:2007). Technical report, Beuth-Verlag, Berlin, 2010.
- [72] August Wöhler. Über die Festigkeits-Versuche mit Eisen und Stahl. *Zeitschrift für Bauwesen*, 20:73–105, 1870.
- [73] Howard Rice Thomas and Victor August Hoersch. *Stresses due to the pressure of one elastic solid upon another*. PhD thesis, University of Illinois, Illinois, 1930.
- [74] Richard H. Stribeck. Die wesentlichen Eigenschaften der Gleit- und Rollenlager. *Mitteilungen über Forschungsarbeiten auf dem Gebiete des Ingenieurwesens, insbesondere aus den Laboratorien der technischen Hochschulen*, (7), 1903.
- [75] M. A. Miner. Cumulative damage in fatigue. *Journal of Applied mechanics*, 67:159, 1945.
- [76] Waloddi Weibull. A statistical distribution function of wide applicability. *Journal of Applied mechanics*, 18:293–297, 1951.
- [77] G. Lundberg and A. Palmgren. *Dynamic capacity of rolling bearings*, volume 196 of *Proceedings of the Royal Swedish Academy of Engineering Sciences*. Generalstabens Litografiska Anstalts Förl., Stockholm, 1947.
- [78] G. Lundberg and A. Palmgren. *Dynamic Capacity of Roller Bearings*, volume 210 of *Proceedings of the Royal Swedish Academy of Engineering Sciences*. Generalstabens Litografiska Anstalts Förl., Stockholm, 1952.

- [79] ASME. *Life Adjustment Factors for Ball and Roller Bearings: An Engineering Design Guide*. Madison, USA, 1971.
- [80] D. Dowson and G. R. Higginson. *Elasto-hydrodynamic lubrication: the fundamentals of roller and gear lubrication*. Pergamon Press, Oxford, first edition, 1966.
- [81] D. Dowson and G. R. Higginson. *Elasto-hydrodynamic lubrication: SI edition*. Pergamon Press, Oxford, 1977.
- [82] E. Ioannides and T. A. Harris. A new fatigue life model for rolling bearings. *Journal of Tribology*, 107(3):367, 1985.
- [83] L. Houpert. Bearing life calculation in oscillatory applications. *Tribology Transactions*, 42(1):136–143, 1999.
- [84] Ernest Rabinowicz. *Friction and wear of materials*. Wiley, New York, second edition, 1995.
- [85] Reaktionsschichtbildung: Verschleiß- und Reibungsminderung durch Reaktionsschichtbildung bei langsamlaufenden Wälzlagern und Zahnrädern. FVA-Forschungsvorhaben 126 I, FVA, Frankfurt, 1988.
- [86] Reaktionsschichtbildung: Verschleiß- und Reibungsminderung durch Reaktionsschichtbildung bei langsamlaufenden Wälzlagern und Zahnrädern. FVA-Forschungsvorhaben 126 II, FVA, Frankfurt, 1991.
- [87] Oszillierende Bewegungen: Wirkung von Schmierstoffen bei langsamen oszillierenden Gleit- und Wälzbewegungen. FVA-Forschungsvorhaben 315, FVA, Frankfurt, 1999.
- [88] J. O. Almen. Lubricants and false brinelling of ball and roller bearing. *Journal of Mechanical Engineering*, pages 415–422, 1937.
- [89] Long Chen, Xin Tao Xia, and M. Qiu. Analysis and control of fretting wear for blade bearing in wind turbine. *Applied Mechanics and Materials*, 26-28:167–170, 2010.
- [90] Hans Pitroff and Robert Mundt. Riffelbildung bei Wälzlagern als Folge von Stillstandserschütterungen. *VDI-Zeitschrift*, 105(26):1219–1230, 1963.
- [91] M. J. Beward. Lagerlebensdauer bei Schwingungsbeanspruchung. *SKF Kugellager-Zeitschrift*, (174), 1973.
- [92] Richard Karbacher. Fettschmierung von Wälzlagern bei oszillierender Beanspruchung. *Tribologie & Schmierungstechnik*, 1998.
- [93] Oszillierende Bewegungen: Schmierungsverhalten bei oszillierenden Gleit- und Wälzbewegungen. FVA-Forschungsvorhaben 315 II, FVA, Frankfurt, 2003.
- [94] M. Grebe and P. Feinle. Brinelling, False-Brinelling, false False-Brinelling. GfT- Reibung, Schmierung und Verschleiss, Aachen, 2006.
- [95] False Brinelling: Stillstehende fettgeschmierte Wälzlager unter dynamischer Belastung. FVA-Forschungsvorhaben 540 I, FVA, Frankfurt, 2010.

-
- [96] Daniel Becker. *Hoch belastete Großwälzlagerungen in Windenergieanlagen*. PhD thesis, Institut für Tribologie und Energiewandlungsmaschinen der TU Clausthal, Clausthal, 2012.
- [97] M. Grebe. *False Brinelling - Standstill marks at roller bearings*. PhD thesis, Slovak University of Technology, Faculty of Material Science, Bratislava, 2012.
- [98] M. Grebe, P. Feinle, and Pavol Blaškovič. Failure of roller bearings without macroscopic motion - influence of the pivoting angle on the contact mechanics and the wear mechanisms in the contact between roller and raceway. *Tribology - industrial and automotive lubrication*, Ostfildern, 2014. Techn. Akad. Esslingen.
- [99] Robert Errichello. Another perspective: False brinelling and fretting corrosion. *Tribology & Lubrication Technology*, 60:34–36, 2004.
- [100] Daniel García Erill. Method for dynamically lubricating a wind turbine pitch blade bearing, 2010. US Patent US 2010/0068055 A1.
- [101] M. Stammler. Verfahren zum Ermitteln einer Notwendigkeit, einen Schmierzustand eines Rotorblattlagers einer Windkraftanlage zu verbessern, Steuervorrichtung zum Durchführen eines solchen Verfahrens und Windkraftanlage mit einer solchen Steuervorrichtung, 2017. German Patent DE 10 2015 218 659 A1.
- [102] Germanischer Lloyd. Richtlinie für die Zertifizierung von Windenergieanlagen. Guideline, Hamburg, 2010.
- [103] DIN ISO 76. Wälzlager - Statische Tragzahlen (ISO 76:2006). Technical report, Berlin, 2009.
- [104] Drehverbindungen für exakte Positionierung. <https://tinyurl.com/uryuu8o>, 26.05.2010. Online; accessed January 28 2014.
- [105] VDI 2230 Blatt 1. Systematische Berechnung hochbeanspruchter Schraubenverbindungen. Guideline, VDI, Düsseldorf, 2014.
- [106] Oliver Menck and Matthias Stammler. Fatigue lifetime calculation of blade bearings considering blade-dependent load distribution. Wind Energy Science Conference, Cork, June 17 2019.
- [107] Josu Aguirrebeitia, Rafael Aviles, Igor Fernandez de Bustos, and Mikel Abasolo. Calculation of general static load-carrying capacity for the design of four-contact-point slewing bearings. *Journal of Mechanical Design*, 132(6):64501, 2010.
- [108] Josu Aguirrebeitia, Mikel Abasolo, Rafael Aviles, and Igor Fernandez de Bustos. General static load-carrying capacity for the design and selection of four contact point slewing bearings: Finite element calculations and theoretical model validation. *Finite Elements in Analysis and Design*, 55:23–30, 2012.

- [109] Josu Aguirrebeitia, Jon Plaza, Mikel Abasolo, and Javier Vallejo. General static load-carrying capacity of four-contact-point slewing bearings for wind turbine generator actuation systems. *Wind Energy*, 16(5):759–774, 2013.
- [110] Iker Heras, Josu Aguirrebeitia, Mikel Abasolo, and Ibai Coria. An engineering approach for the estimation of slewing bearing stiffness in wind turbine generators. *Wind Energy*, 22(3):376–391, 2019.
- [111] ANSYS, Inc. ANSYS Mechanical APDL Basic Analysis Guide, 2019.
- [112] A. Daidie, Z. Chaib, and A. Ghosn. 3d simplified finite elements analysis of load and contact angle in a slewing ball bearing. *Journal of Mechanical Design*, 2008(130), 2008.
- [113] X. H. Gao, X. D. Huang, H. Wang, and J. Chen. Modelling of ball-raceway contacts in a slewing bearing with non-linear springs. *Proceedings of the Institution of Mechanical Engineers, Part C: Journal of Mechanical Engineering Science*, 225(4):827–831, 2011.
- [114] Hua Wang, Pieyu He, Bitao Pang, and Xuehai Gao. A new computational model of large three-row roller slewing bearings using nonlinear springs. *Proceedings of the Institution of Mechanical Engineers, Part C: Journal of Mechanical Engineering Science*, 130:095440621770422, 2017.
- [115] Arne Bartschat. *Entwicklung eines Kraftübertragungselements für die realitätsnahe Erzeugung von Rotorblattbelastungen an einem Prüfstand*. Master thesis, HTW, Fachbereich Ingenieurwissenschaften - Energie und Information, Berlin, 2014.
- [116] Florian Schleich. *Methodenentwicklung zum Entwurf einer Prüfstandskomponente zur realitätsnahen Abbildung von Rotorblattlagerbelastungen durch ein Rotorblatt einer Windenergieanlage*. Master thesis, Technische Universität Hamburg-Harburg, Institut für Laser- und Anlagensystemtechnik, Hamburg, 2018.
- [117] ISO 16701:2015. Corrosion of metals and alloys – corrosion in artificial atmosphere – accelerated corrosion test involving exposure under controlled conditions of humidity cycling and intermittent spraying of a salt solution. Technical report, ISO, 2015.
- [118] Liebherr-Components. Großkomponenten für Offshore-Windkraftanlagen (Broschüre), 2011.
- [119] Josie Olk. Lippstadt auf dem Weg zum Technologiestandort. <http://www.lippstadt.de/wirtschaft/2013-02-18-Artikel-SM.pdf>, 2012. Online, Accessed September 23 2013.
- [120] Solutions&co - Pays de la Loire. Rollix. <https://tinyurl.com/wo7yqx2>, 2017. Online; accessed August 15 2019.
- [121] Jeong Woo Han, Ju Seok Nam, Young Jun Park, Geun Ho Lee, and Yong Yun Nam. An experimental study on the performance and fatigue life of pitch bearing for wind turbine. *Journal of Mechanical Science and Technology*, 29(5):1963–1971, 2015.

-
- [122] Fangyuan Blade Bearing Test Rig. <http://www.cfmif.com/n8911c52.aspx>, 2019. Online; accessed September 14 2019.
- [123] E de Vries. Close up - testing the v164 80-metre blade. *WindPower Monthly*, 2013, 13. Januar 2013.
- [124] Nordex SE. *Geschäftsbericht 2010*. Hamburg, 2011.
- [125] M. Stammler, Karsten Ohde, and Sven Sagner. Blade bearing test rig. DEWEK 2015, 12th Germany Wind Energy Conference, Bremen, 19.5.2015.
- [126] M. Grebe, P. Feinle, and W. Hunsicker. Einfluß verschiedener Faktoren auf die Entstehung von Stillstandsmarkierungen (False-Brinelling-Effekt). GfT - Reibung, Schmierung und Verschleiß, Aachen, 2007.
- [127] Größeneinfluss Wälzlagerverschleiß: Einfluss der Wälzlager-baugröße auf das Verschleißverhalten von Wälzlagern. FVA-Forschungsvorhaben 327 III, FVA, Frankfurt, 2011.
- [128] SKF. *Wälzlager: Hauptkatalog*. 2014.
- [129] E. Wittek, M. Kriese, H. Tischmacher, S. Gattermann, B. Poniek, and G. Poll. Capacitances and lubricant film thicknesses of motor bearings under different operating conditions. XIX International Conference on Electrical Machines, Rome, Italy, September 6-8 2010.
- [130] M. Stammler, A. Reuter, and G. Poll. The influence of oscillation sequences on rolling bearing wear: Under review. *Bearing World Journal*, 2019.
- [131] Fraunhofer IWES. Full scale blade testing. <https://tinyurl.com/tg6aurx>, 2019. Online; accessed September 21 2019.
- [132] VDI 2206. Entwicklungsmethodik für mechatronische Systeme. Guideline, VDI, Düsseldorf, 2010.
- [133] Christian Broer, Felix Steinkuhl, and M. Stammler. HAPT - Ausschreibung eines Blattlagerprüfstandes für den Einsatz im Prüfzentrum Hamburg-Bergedorf: Lastenheft. <http://www.deutsche-evergabe.de/>. Online; accessed March 20 2017.
- [134] Gesa Frerichs. *Konzeptionierung eines Blattlagerprüfstandes*. Project thesis, Leibniz Universität Hannover, Institut für Maschinenkonstruktion und Tribologie, Hannover, 2014.

Annex

Section 4.4 contained exemplary microscopic pictures of the raceway conditions of type 7220 and type 12480 bearings after different tests. The following figures show further microscopic pictures of said bearings to give an impression of variances between different contact areas.

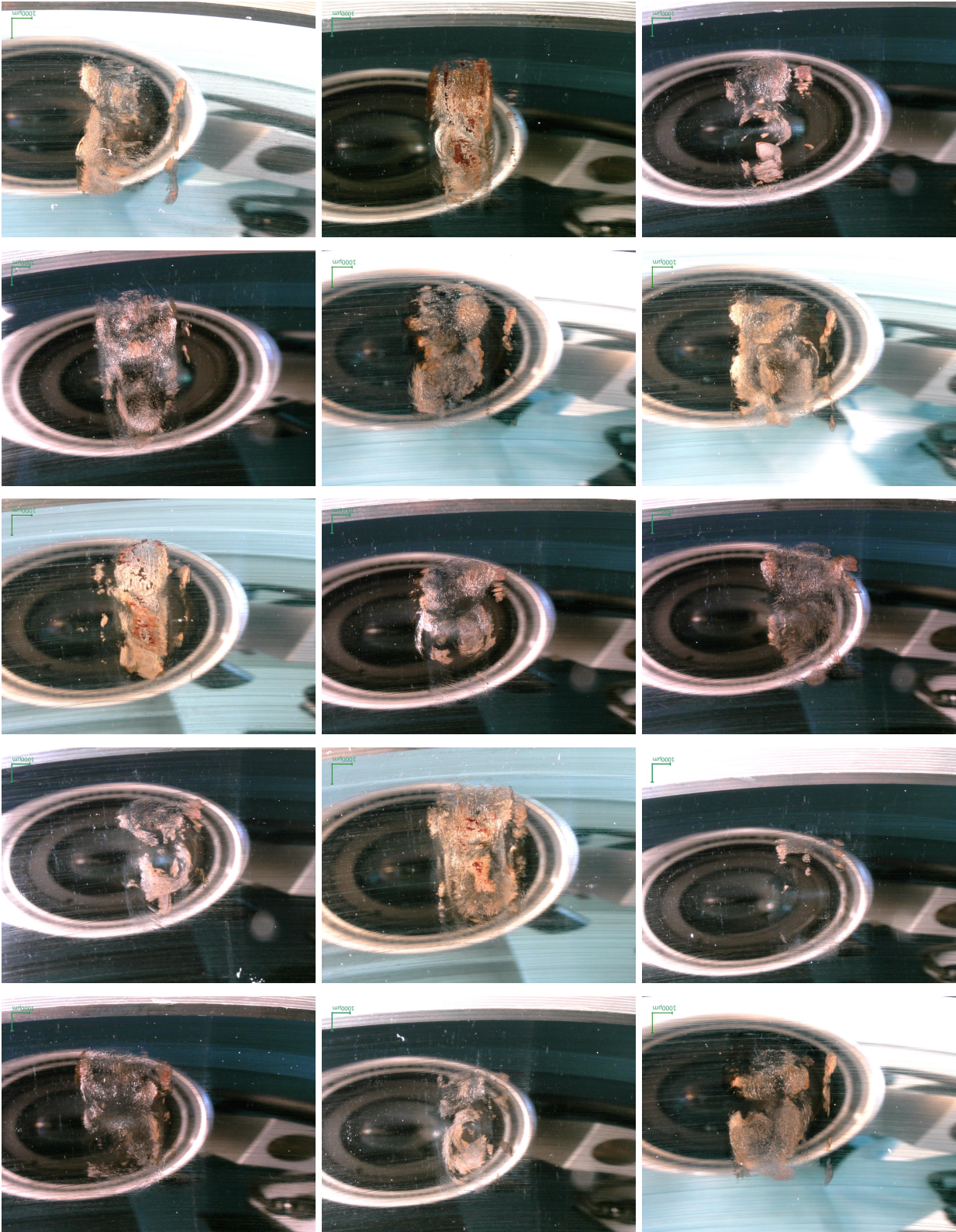


Figure .1: Raceway condition inner ring, Test ID 1, Bearing ID 0006

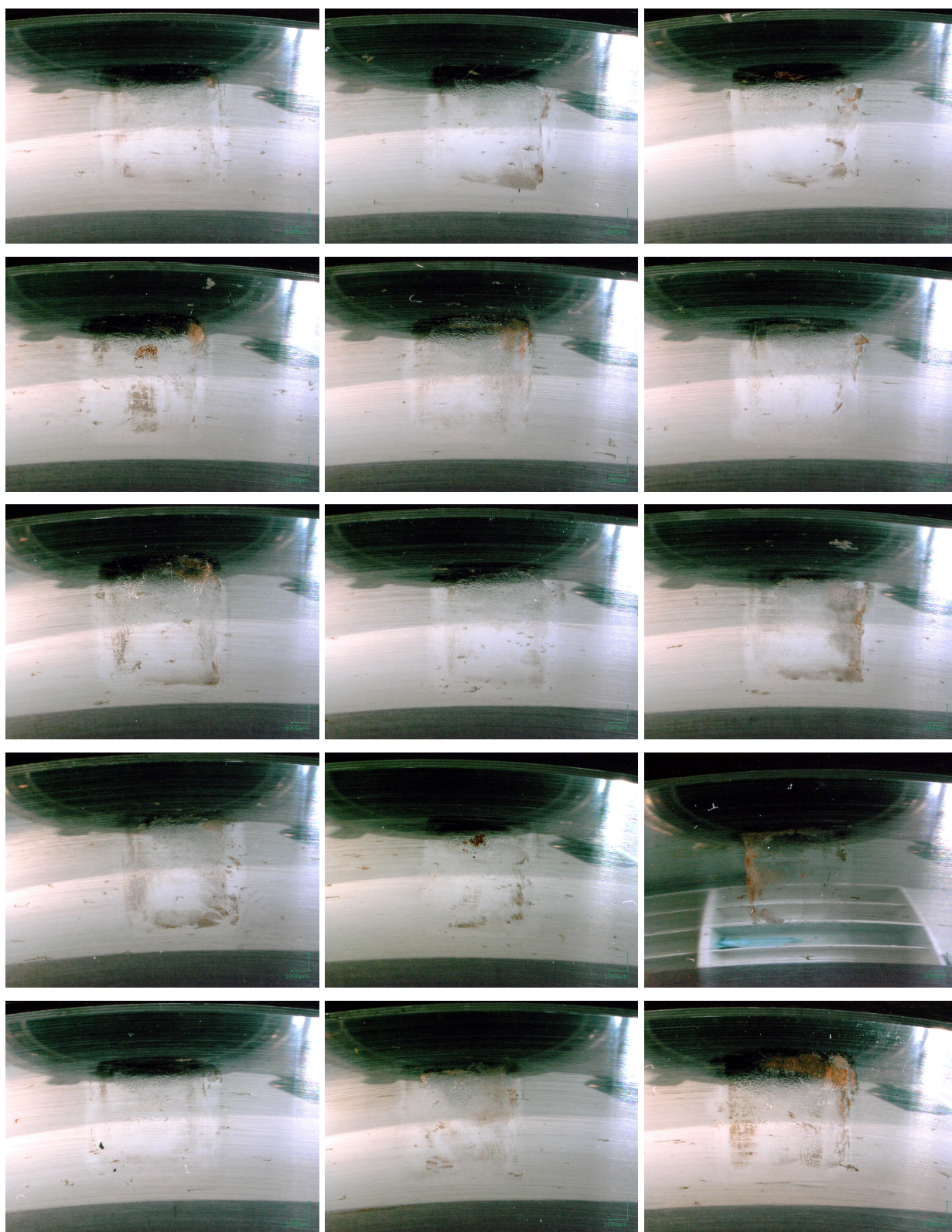


Figure .2: Raceway condition inner ring, Test ID 2, Bearing ID 0019

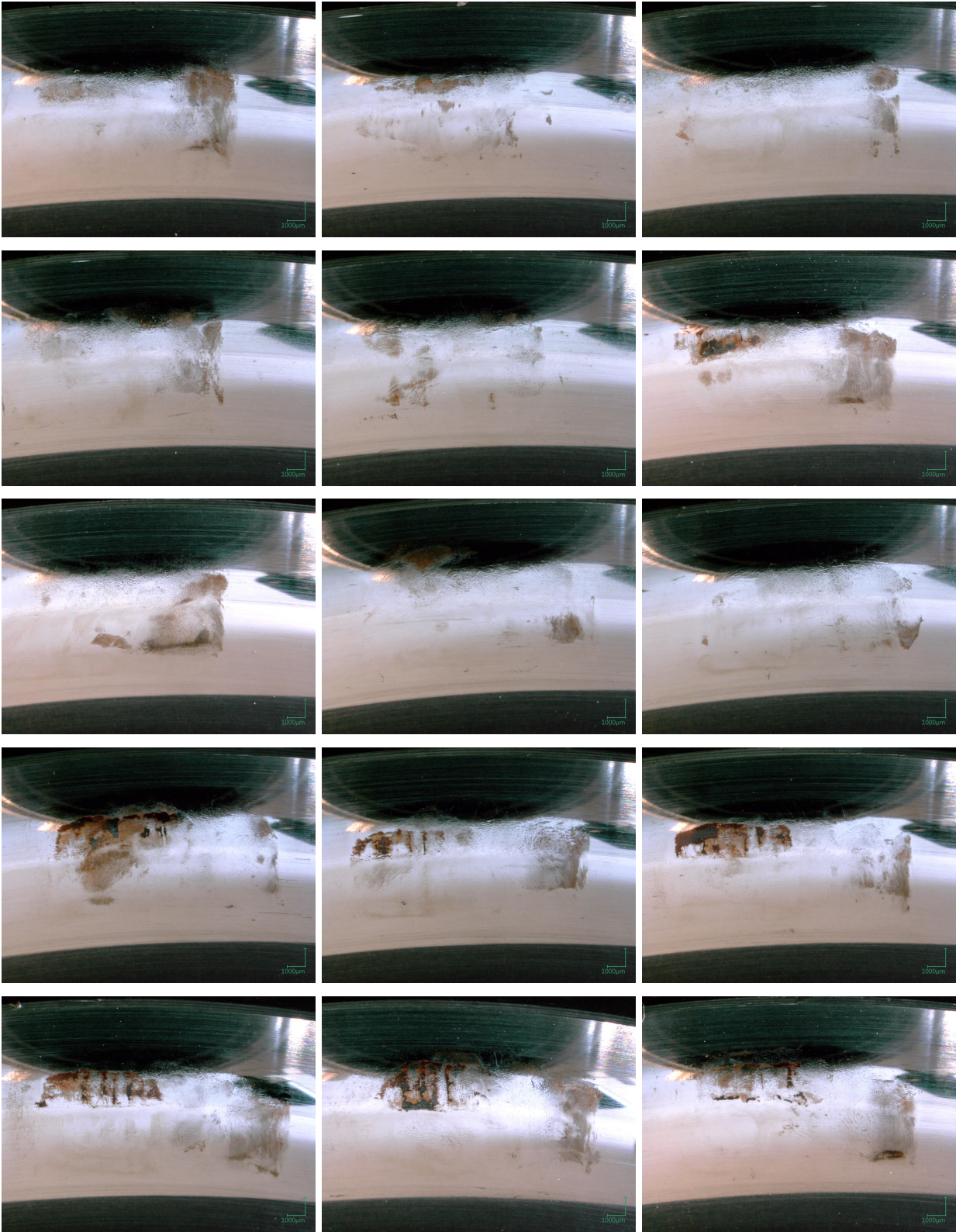


Figure .3: Raceway condition inner ring, Test ID 3, Bearing ID 0026

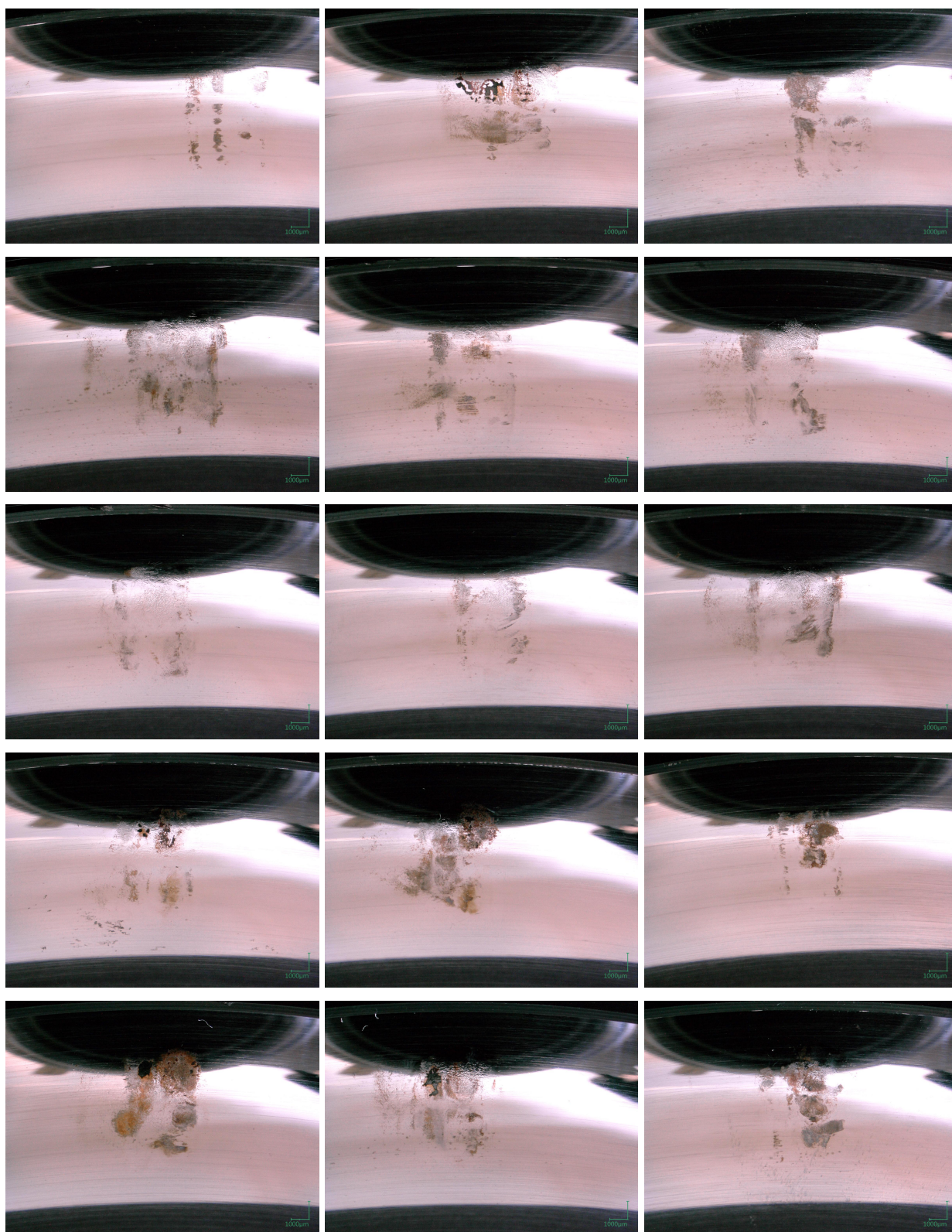


Figure .4: Raceway condition inner ring, Test ID 4, Bearing ID 0007

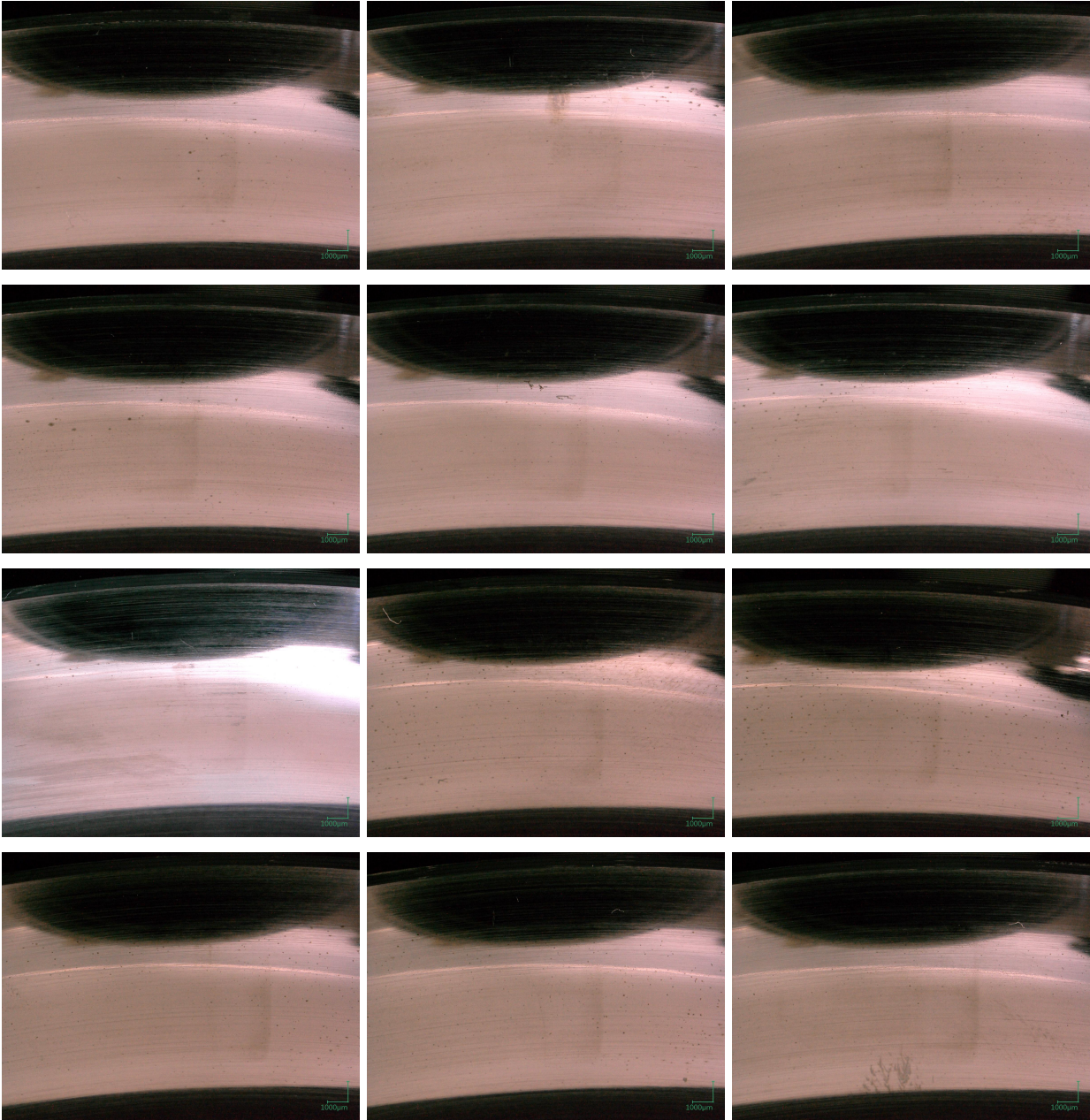


Figure .5: Raceway condition inner ring, Test ID 5, Bearing ID 0009

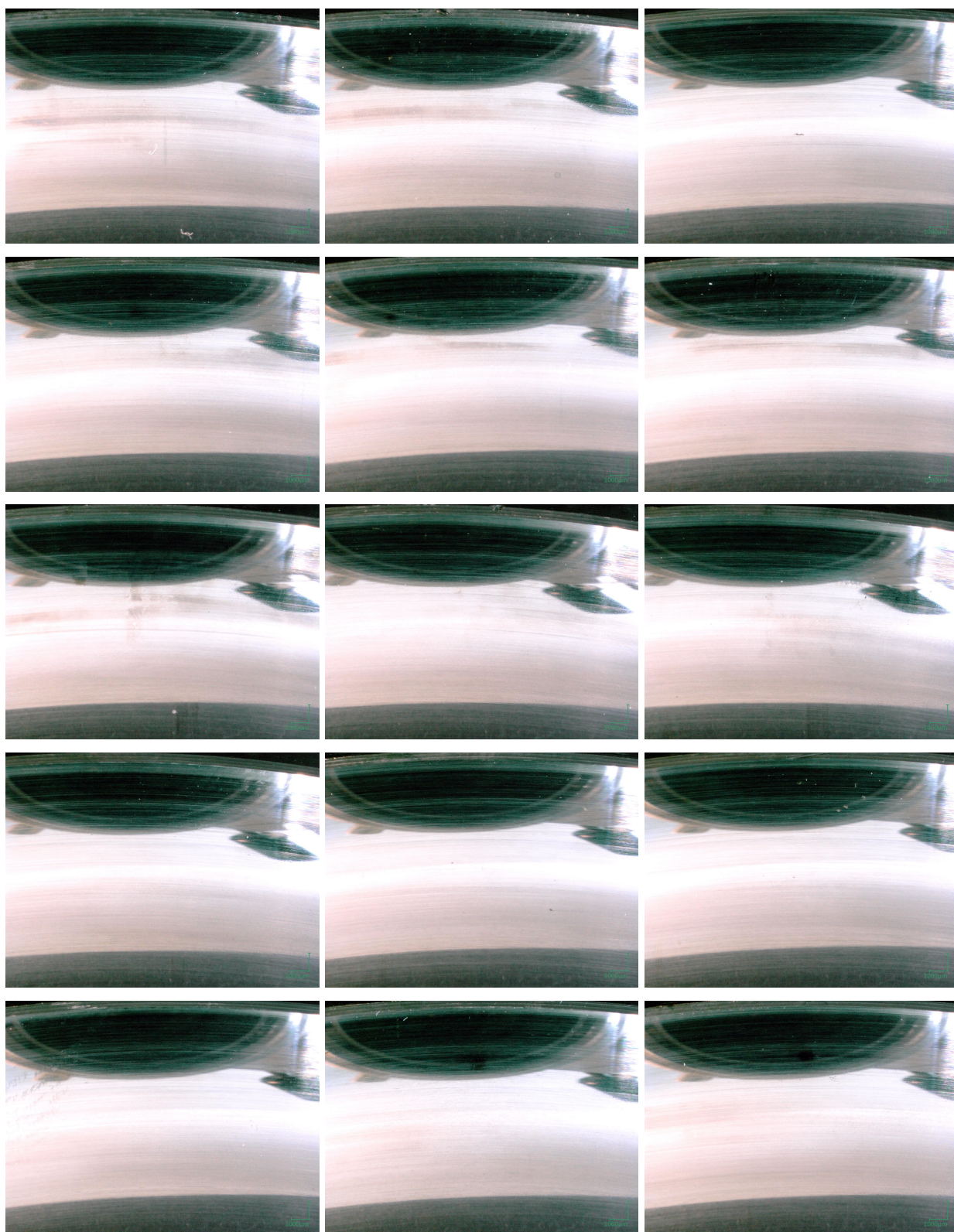


Figure .6: Raceway condition inner ring, Test ID 6, Bearing ID 0021

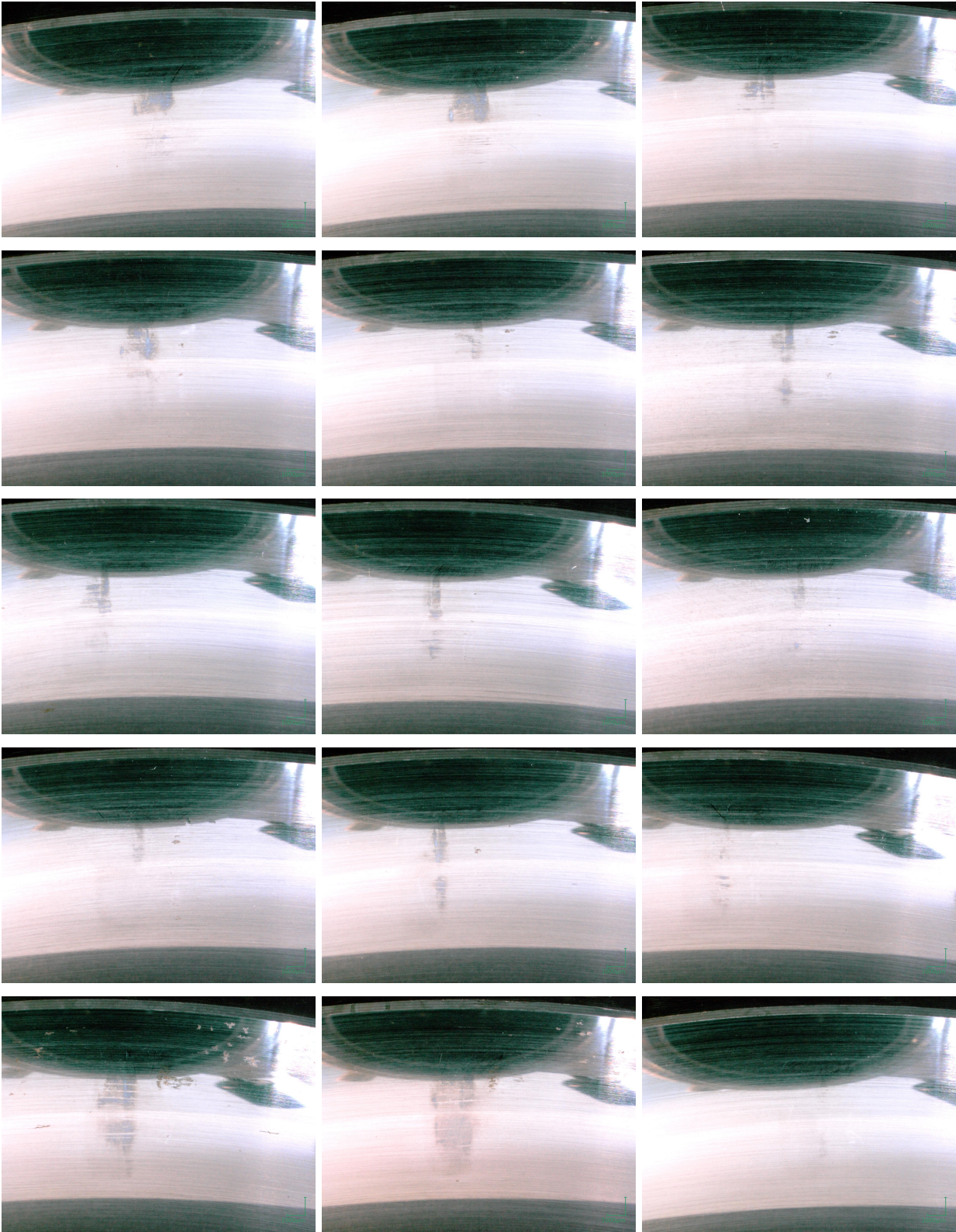


Figure .7: Raceway condition inner ring, Test ID 7, Bearing ID 0023

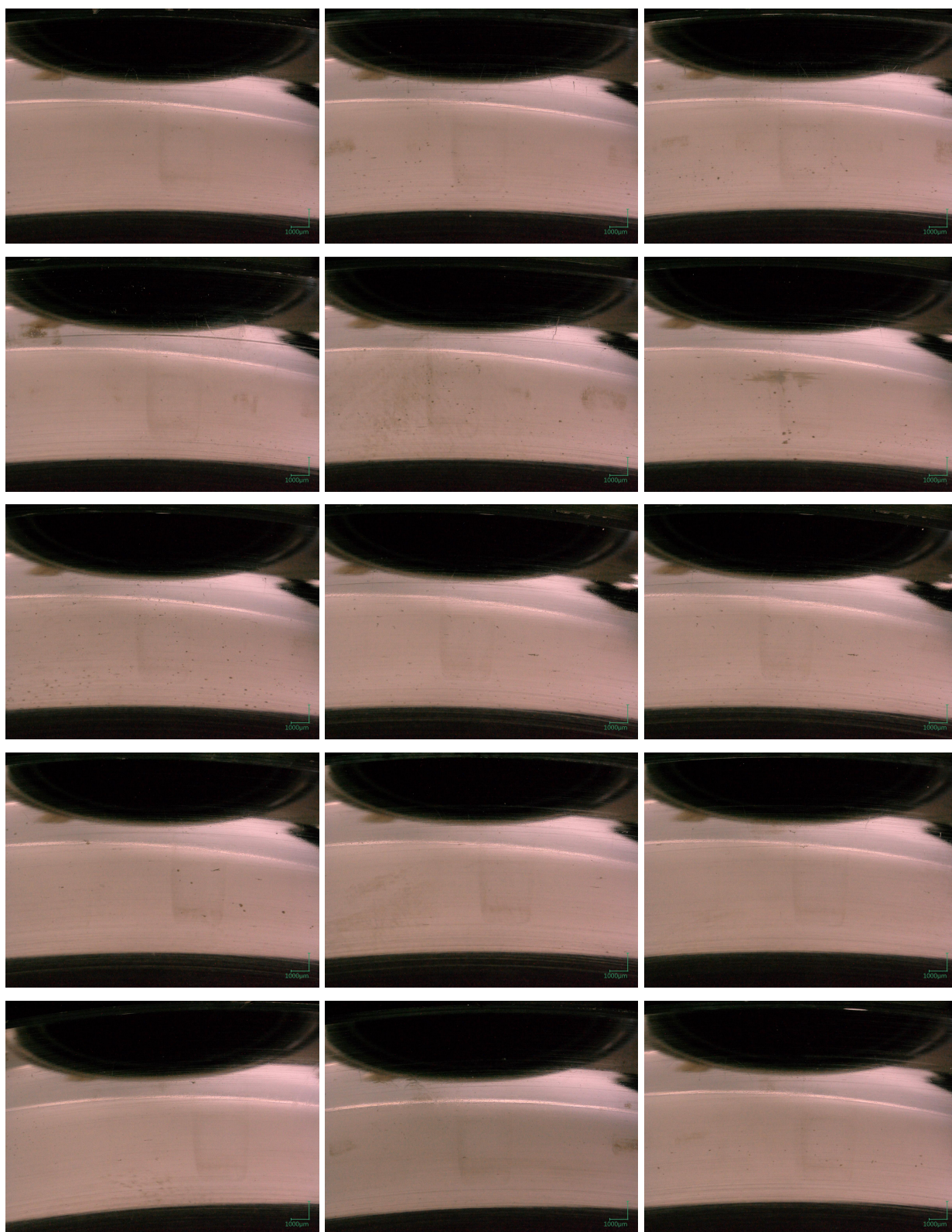


Figure .8: Raceway condition inner ring, Test ID 8, Bearing ID 0017

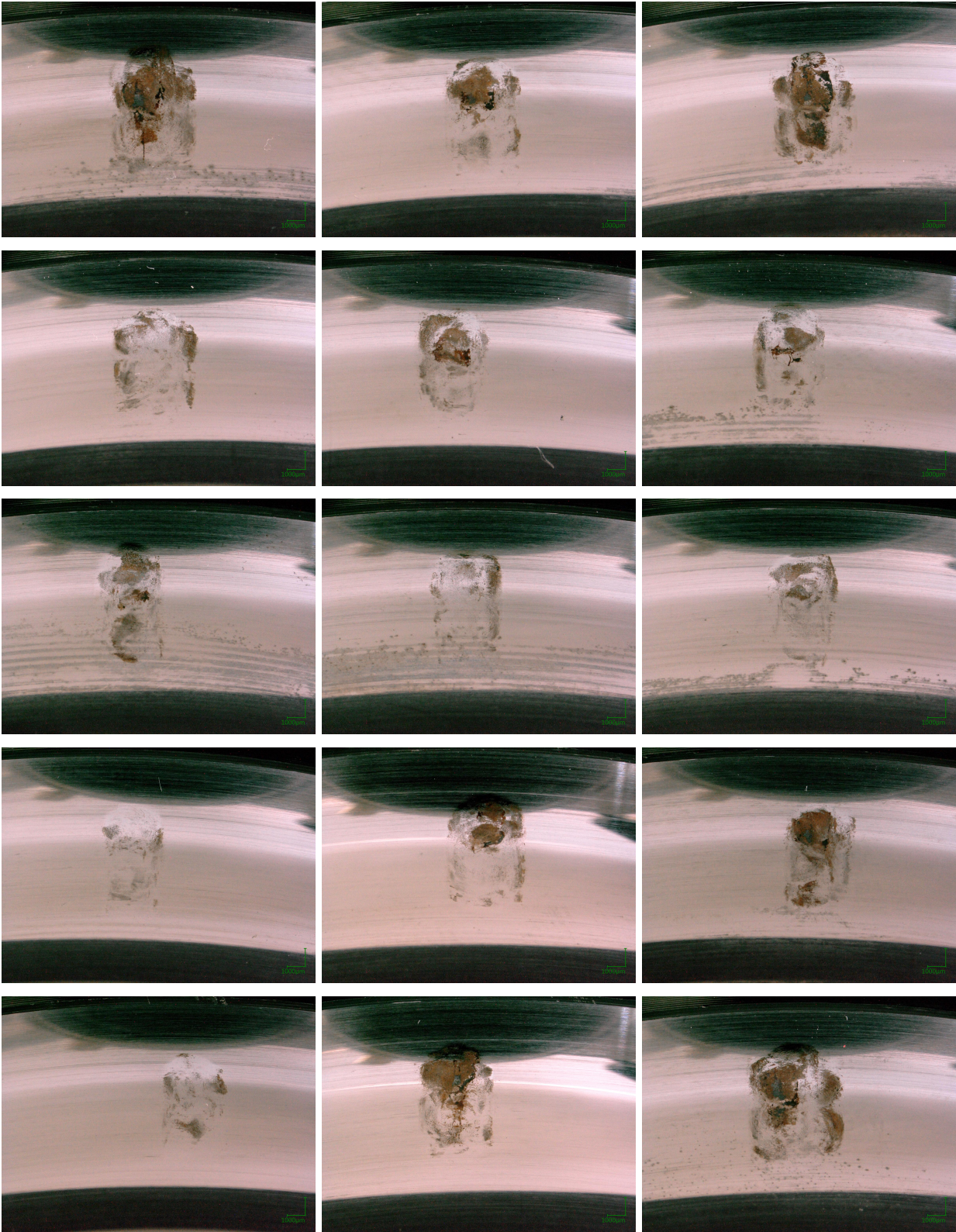


Figure .9: Raceway condition inner ring, Test ID 9, Bearing ID 0013

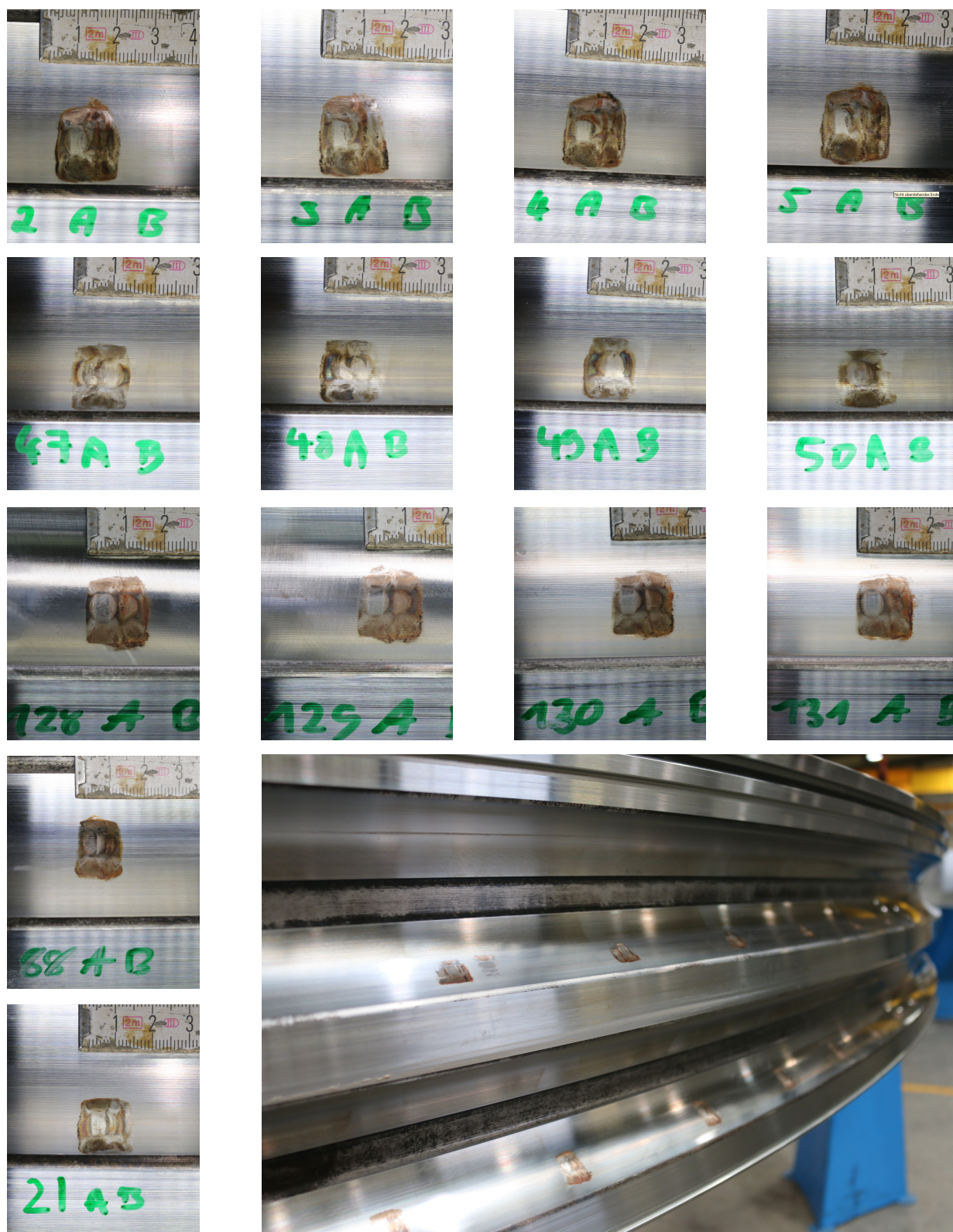


Figure .10: Raceway condition inner ring, Test ID 10, Bearing ID 0001

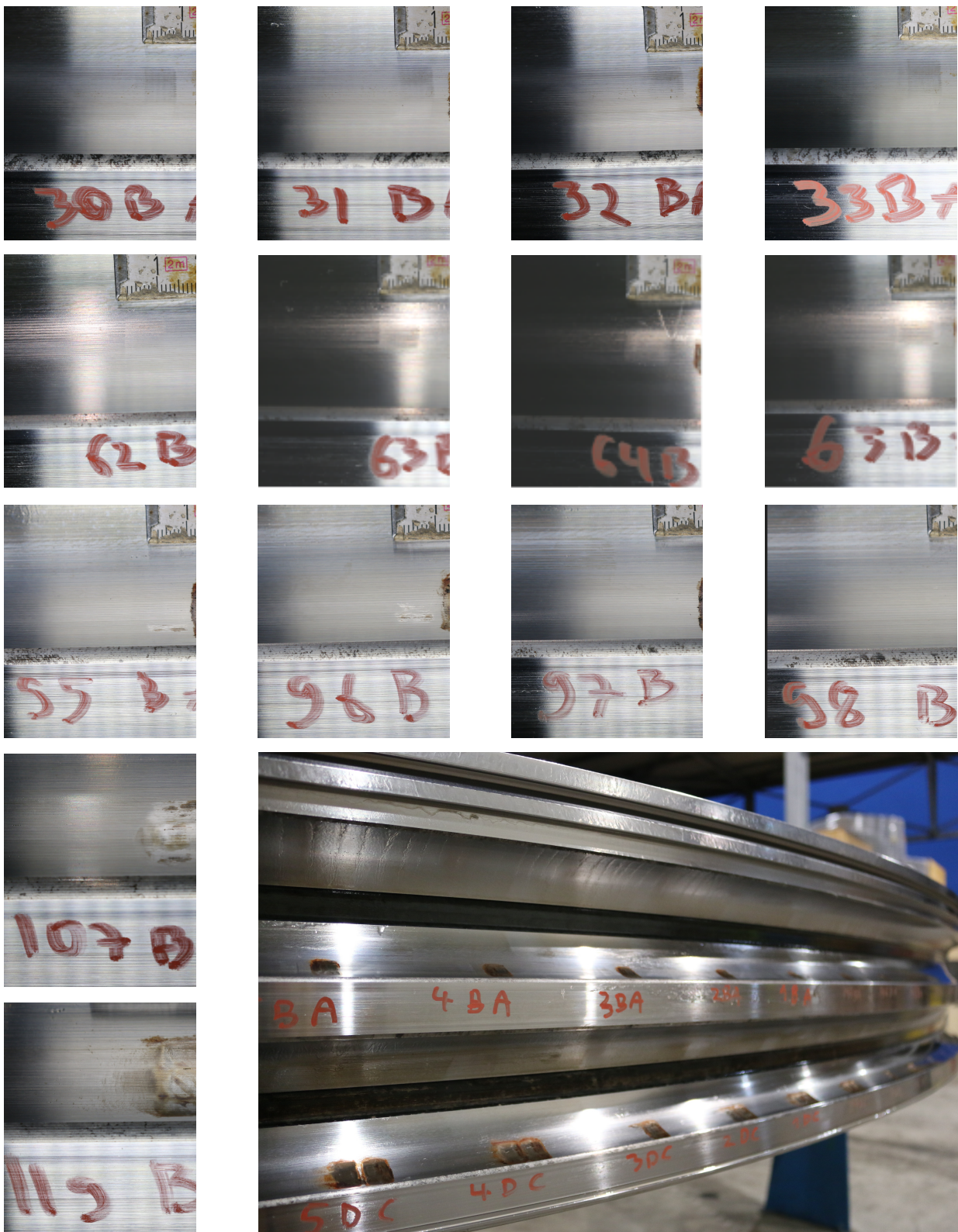


Figure .11: Raceway condition inner ring, Test ID 11, Bearing ID 0002